Doctoral Dissertation
Doctoral Program in Science and Technology of Materials (34th Cycle)

Single metal atom catalysts for the electrochemical reduction of CO_2

By

Daniele Sassone

******

Supervisors:
Prof. F. C. Pirri, Supervisor
PhD. S. Bocchini, Co-Supervisor
PhD. J. Zeng, Co-Supervisor

Doctoral Examination Committee:
Prof. Giancarlo Cicero, Referee, Politecnico di Torino
Prof. Simelys Hernandez, Referee, Politecnico di Torino
Prof. Paolo Pescarmona, Referee, University of Groningen
PhD Adriano Sacco, Referee, Istituto Italiano di Tecnologia
Prof. Joseph Sadighi, Referee, Georgia Institute of Technology

Politecnico di Torino
2022

Declaration

I hereby declare that, the contents and organization of this dissertation constitute my own original work and do not compromise in any way the rights of third parties, including those related to the security of personal data.

Turin, 2022

Daniele Sassone

* This dissertation is presented in partial fulfillment of the requirements for **Ph.D. degree** in the Graduate School of Politecnico di Torino (ScuDo).

“Per chi conosce la lore,

Per chi la sta scoprendo,

Per chi la scoprirà”.

Sabaku no Maiku

Acknowledgment

Vorrei caldamente ringraziare tutte le persone conosciute nel percorso di questi anni. Il dottorato, che in primis è stato un percorso formativo e lavorativo, ha portato con sè un valore aggiunto molto più grande, rivelandosi in una forte esperienza umana. Diverse sono state le lezioni affrontate. Dalla difficile ma necessaria capacità di gestire lo stress, l'accettazione e superamento delle delusioni, specialmente quando paragonate alle proprie aspettative, ed infine la gestione di una mole di lavoro più grande del tempo a propria disposizione. Tutte queste intense emozioni si sono affacciate anche a frequenti momenti di entusiasmo, felicità e a volte fin troppo ottimismo. Tutto questo sarebbe stato un peso insormontabile se non fosse stato per tutte quelle amicizie trovate in questo percorso; questo assieme al sostegno ed appoggio della mia compagna, Claudia.

Fare un elenco lo trovo riduttivo, non è da me. Non ho bisogno di chiamarvi uno a uno per dirvi quanto siate diventati persone importanti nella mia vita. All'inizio colleghi, ma col tempo grandi amici. Grazie di tutto, della vostra grande pazienza e dei momenti di spensieratezza. Sono stati per me un inestimabile tesoro.

Abstract

The thesis is based on the electrochemical activation of CO_2 towards several types of catalysts, having as common characteristic, the attempts and realization of single metal active sites. Different approaches were investigated, throughout the Lewis acids doping of organic polymers, taking the advantages of peculiar structures like the one of the Molecular Organic Framework (MOF) and finally more challenging approaches starting from metallorganic complexes building heterogeneous materials based on metalloporphyrin.

The complete physical and chemical characterization of those catalysts was performed by several techniques like the Attenuated Total Reflectance Fourier Transform Infrared spectroscopy (ATR-FT-IR), UV-Vis spectroscopy and Diffuse Reflectance Measurement, Powder X-Ray Diffraction (XRD), X-Ray Photoelectron Spectroscopy (XPS), Field-Emission Scanning Electron Microscopy (FE-SEM), Brunauer–Emmett–Teller surface analysis (BET) and Thermo-Gravimetric and Evolved Gas Analyses (TGA-EGA). Parallel to them, fundamental electrochemical analysis were performed in order to detect and quantify the possible selectivity towards the CO_2 conversion and to compare it to the competitive H_2 evolution reaction, such as: Cyclic Voltammetry (CV), Electrochemical Impedance Spectroscopy (EIS) and Chronoamperometry (CA).

The catalysts were able to produce variegated products of great interest for both the fuels and chemicals industrial sectors. Indeed, carbon monoxide, formate, ethylene and methane could be synthetized at different rate and selectivity based on the different type of catalysts. In order to optimize such conversion processes, also the experimental setting followed a continuous improvement all along the years,

strictly following the upgrade obtained from the scientific community highly active in this research field. Indeed, starting from simpler apparatus based on H-cell, the electrochemical setup followed itself a great improvement passing through the batch cell till the most performing flow cell employment.

The interest to stabilize single metal centers, considered to be the active species for the CO_2 conversion through electrochemical process, hided in some way a more complex topic: the nature of the true active site under an electrochemical bias. Indeed, the work, following the updates coming from the most recent literature, highlights the real nature of the catalyst under potential that is often underestimated. Indeed, only performing specific physical and chemical characterization under potential, it is possible to analyze the active species all along an electrochemical process. In our specific case we were indeed able to identify metallic clusters formed during the catalysis that they were completely unpredicted in the previous literature for the last part of the thesis.

Contents

List of Figures

List of Tables

List of Acronyms

ACN - Acetonitrile

AEL - Anodic Exchange Layer

AEM - Anion Exchange Membranes

Atm - Atmosphere units

ATR-FT-IR - Attenuated Total Reflectance Fourier Transform Infrared Spectroscopy

BET - Brunauer–Emmett–Teller surface analysis

BPM - Bipolar Membrane

C_2H_4 - Ethylene

CA – Chronoamperometry

C_{dl} – Double-layer capacitance

CEL - Cathodic Exchange Layer

CEM - Cation Exchange Membranes

CH_4 - Methane

CO_2RR - Carbon dioxide reduction reaction

COF - Covalent Organic Framework

CP - Carbon Paper

CuTAPP - 5,10,15,20-Tetrakis-(4-aminophenyl)-porphyrin-Cu^{2+}

CuTPP - Cu-tetrakisphenylporphyrin

CuTPP(F) - Cu-tetrakis(pentafluorophenyl)porphyrin

CV - Cyclic Voltammetry

DFT – Density Functional Theory

EB-PANI - Emeraldine Base Polyaniline

ECSA - Electrochemically Active Surface Area

EDX - Energy-Dispersive X-ray spectroscopy

ES-PANI- Emeraldine Salt Polyaniline

EtOH - Ethanol

FE - Faradaic Efficiency

FE-SEM - Field-Emission Scanning Electron Microscopy

GC – Glassy Carbon

HER - Hydrogen Evolution Reaction

HOPG – Highly Ordered Pyrolytic Graphite

IHP - Inner Helmholtz Plane

IL - Interfacial Layer/Bipolar Junction

iPrOH - Iso-propanol

MEA - Membrane Electrode Assembly

MeOH - Methanol

MOF - Metal Organic Framework

MOF – Molecular Organic Framework

MWCNT – Multi Walled Carbon Nanotube

NMP - N-Methyl-2-pyrrolidone

OHP - Outer Helmholtz Plane

PCET - Proton-Coupled Electron Transfer

PEM - Protonic Exchange Membrane

PTFE - Polytetrafluoroethylene

PVDF - Polyvinylidene Fluoride

R_{CT} –Charge Transfer Resistance

RHE - Reverse Hydrogen Electrode

$scCO_2$ - Supercritical carbon dioxide

SHE - Standard Hydrogen Electrode

SSE - Solid-State Electrolyte

TAPP - 5,10,15,20-Tetrakis-(4-aminophenyl)-porphyrin

TEA - Triethylamine

TEA- Triethylamine

TEM – Transmission Electron Microscopy

TGA-EGA - Thermo-Gravimetric and Evolved Gas Analyses

THF – Tetrahydrofuran

TPP – Tetraphenyl porphyrin

TPP(F) - Tetrakis(pentafluorophenyl)porphyrin

TRL - Technology Readiness Level

u-GC - Micro gas chromatography

XPS - X-Ray Photoelectron Spectroscopy

XRD - Powder X-Ray Diffraction

ZIF – Zeolitic Imidazole Framework

Chapter 1

Introduction and state of the art

The carbon dioxide (CO_2) is a charming molecule heavily studied for its simplicity and well-known inertness; nevertheless, it conceals a lot of hidden chemistry inside[1]. Indeed, an isolated carbon atom bonded to a couple of oxygen atoms represents one face of the nature's token able to balance all the redox processes characterizing the life we know. Starting from the sunlight, the energy vector, passing through several biologic mediators and photosystems, two different high energetic molecules are produced, namely the ATP and NADH. These extremely reactive compounds need to be rapidly consumed to produce more stable energetic molecules through the so-called *Calvin cycle*, fixing the CO_2 to glyceraldehyde-3-phosphate and subsequently to carbohydrates and several other energetic complex molecules[2]. The entire process in which CO_2 is fixed at expense of light energy together with H_2O is the so called *photosynthesis*, which generates high energy carbon compounds like the carbohydrates and also molecular O_2. The formers, are fuels that will be consumed to sustain the organism, following a detailed redox pathway called "*cellular respiration"* avoiding sudden and uncontrolled energy release. Such pathway is responsible of the regeneration of ATP and NADH(P) biosynthesis, these molecules guarantee the life through the biosynthesis of the necessary molecules, their locomotion and transport across cell membranes, and several other processes. The final acceptor of the cellular respiration is the oxygen molecule, the second face of the token's life, which would be transformed to water parallel to the CO_2 release, in a continuous life cycle.

Such sophisticated energy scheme is based on three elements: the energy, provided by the sun, the CO_2 and the O_2. The necessity of a complex redox mediator has not been randomly selected by nature. Indeed, the CO_2 hides a great thermodynamic stability, partially preserved by the absence of a dipole momentum,

which makes it tremendously difficult to convert this molecule in a more energetic substrate[3]. In addition, the CO_2 is the most oxidized form of carbon, making the molecule suitable for redox processes. Here there is the sophisticated balance that characterizes this molecule: even if CO_2 is inclined to be reduced, due to kinetics restrictions, the activation energy for this step is energetically expensive. This is translated to a general inertness of CO_2 in normal condition, which becomes accessible once a proper redox mediator system is built up; like in the case of the bio apparatus.

The electrochemical conversion of CO_2 is the human approach to mimic, and hopefully optimize, the nature workshop. Applying a potential bias in an electrolysis process, we are able to climb back the required energy barrier to activate the CO_2, to break its symmetry and then reach more reduced and hydrogenated products. The interesting aspect characterizing the electrolysis processes is the possible integration with green alternative energy plants. Fuels and chemicals production could be obtained using CO_2 as building blocks at the expanse of energy coming from photovoltaics, wind power, hydroelectric and any different sources connected to the place of interest. The true power of CO_2 electrolysis conversion resides in its versatility, making it able to be displayed everywhere.

1.1 Thermodynamic analysis

The electrochemical conversion of CO_2, also denoted as "*carbon dioxide reduction reaction, CO_2RR*" has gained much attention in the last two decades due to the interest of modern policies to mitigate the climate change. The CO_2 electrolysis is extremely emphasized, it is commonly reported as a process able to convert CO_2 directly from the air and to be able to lower its concentration from the atmosphere. Even if it is usually reported in this way, the actual experimental setup works instead with pure commercial resources of CO_2. The most similar approach to the one described above, should involve the combination of carbon capture technology with the consequent electrolysis processes. Such technology is still present and for the readiness of the actual technology would require extremely high energy input which would make it difficult to sustain the overall system from an economical point of view[4].

The CO_2RR should be thought as a promising tool able to produce molecules of interest, likes fuels and chemicals, and parallel stock the exceeding energy produced from discontinue alternative energy plants. The Technology Readiness Level (TRL) for CO_2RR did not reach a turning point, indeed in the far 2004 a TRL of 5 for zero-

gap configuration cell[5] was reached and still today the actual scale up does not grow so far. To describe the evolution of CO_2RR technology, the *thermodynamic analysis* of the process is the perfect start. The molecule CO_2 molecule, being the most oxidized form of carbon, is placed at the bottom of the free Gibbs energy[6] resulting almost inert, as reported in the Latimer-Frost diagram (**Error! Reference source not found.**) in w hich several reduced carbon products are placed at higher free energy values. Despite these values, the half semi reactions for these reduced products are not thermodynamically expensive. In the Table 1 the thermodynamic potentials versus Standard Hydrogen Electrode (SHE) at pH 7 for different reduced products of CO_2 are reported[7]. With the exclusion of the $CO_2^{\cdot-}$ radical anion, requiring the lowest potential (negative potential), all the other half reactions show accessible bias, if not even positive ones[8,9]. The main difference among such values is correlated to the number of electrons and protons involved. The highest energy request occurs for the mono electron transfer, necessary to bend the planar geometry of the molecule and occupy the lowest-energy unoccupied molecular orbital. From Table 1 is possible to see that the applied potential continuously decreases as the number of electrons and protons involved increases[10]. Moreover, at equal number of electrons and protons, half reactions proceeding in acidic media require a higher potential. That is numerically significant for products like HCHO, CH_3OH, C_2H_4 and CH_3CH_2OH and lesser for CH_4, CO and HCOOH instead.

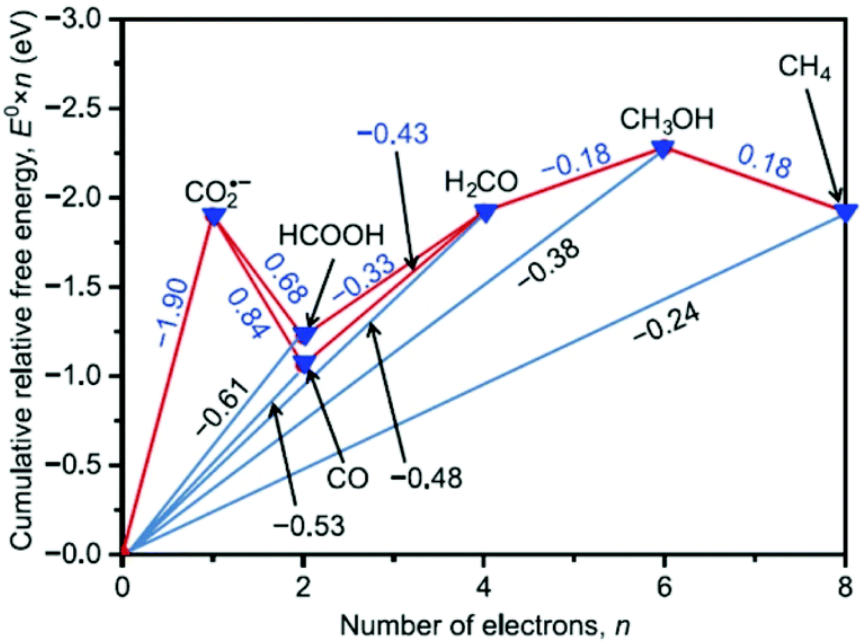

Figure 1: Latimer-Frost diagram for the multi-electron, multi-proton reduction of CO_2 in aqueous solution at pH = 7. Reproduced with permission from ref. 6. Copyright © 2014, Science China Press and Springerverlag Berlin Heidelbeg.

Even if concerted multi-electrons transfer are feasible, single steps concerning more than 2 electrons are not reported in literature. In nature, multi-electrons reduction with enzymes or photosystems are well known, nevertheless they are characterized by consequent electron transfers involving one or two concerned electrons. Usually, complex mechanism involves cascade steps of one/two electron reductions occurring sequentially in the same substrate. The Nitrogenase enzymes are a class of enzyme able to perform one of the most difficult reduction catalysis possible, the N_2 fixation. Such process occurs through several one proton-coupled electron transfer (PCET) and occurs six times for cycle. Each intermediates was isolated and characterized, so justifying the one-electron transfers mechanism[11,12,13,14].

Table 1: Theoretical electrochemical potentials of CO_2 reduction half reaction versus Standard Hydrogen Electrode (SHE), at pH 0, at 25 °C, 1 atm and 1.0 M concentration of other solutes.

Possible half-reactions of electrochemical CO_2 reduction	Electrode potentials (V vs SHE)
$2H^+ + 2e^- \rightarrow H_2$	0.000
$CO_2 + e^- \rightarrow *COO^-$	-1.486
$CO_2 + 2H^+ + 2e^- \rightarrow HCOOH$	-0.250
$CO_2 + H_2O + 2e^- \rightarrow HCOO^- + OH^-$	-1.078
$CO_2 + 2H^+ + 2e^- \rightarrow CO + H_2O$	-0.106
$CO_2 + H_2O + 2e^- \rightarrow CO + 2OH^-$	-0.934
$CO_2 + 4H^+ + 2e^- \rightarrow HCHO + H_2O$	-0.070
$CO_2 + 3H_2O + 4e^- \rightarrow HCHO + 4OH^-$	-0.898
$CO_2 + 6H^+ + 6e^- \rightarrow CH_3OH + H_2O$	+0.016
$CO_2 + 5H_2O + 6e^- \rightarrow CH_3OH + 6OH^-$	-0.812
$CO_2 + 8H^+ + 8e^- \rightarrow CH_4 + 2H_2O$	+0.169
$CO_2 + 6H_2O + 8e^- \rightarrow CH_4 + 8OH^-$	-0.659
$2CO_2 + 2H^+ + 2e^- \rightarrow H_2C_2O_4$	-0.500
$2CO_2 + 2e^- \rightarrow C_2O_4^{2-}$	-0.590
$2CO_2 + 12H^+ + 12e^- \rightarrow C_2H_4 + 4H_2O$	+0.064
$2CO_2 + 8H_2O + 12e^- \rightarrow C_2H_4 + 12OH^-$	-0.764
$2CO_2 + 12H^+ + 12e^- \rightarrow CH_3CH_2OH + 3H_2O$	+0.084
$2CO_2 + 9H_2O + 12e^- \rightarrow CH_3CH_2OH + 12OH^-$	-0.744

In order to build up a catalytic system able to perform a similar work, we could find inspiration in one of the most studied and know natural catalytic system involving the CO_2: the photosynthesis. Such light driven reaction involves six molecules of CO_2 converted into six-carbon-atom sugars at the expense of ATPs and NADHs. Since both reducing agents are able to release two electrons per mole, several two electrons steps occur for the overall reaction. A similar reaction pathway is theorized on metallic copper surface in the CO_2RR. Indeed, after a two electrons transfer on CO_2 forming the carbon monoxide, this intermediate is still bonded and can proceed with further

reduction steps which will eventually form all the other compounds known in literature for this catalyst, like the aldehydes, carboxylic acids, alcohols and so on[15].

1.2 Solubility

Acknowledged the thermodynamic aspects of CO_2RR, the second essential point is the CO_2 *solubility* in the electrolyte. Excluding advanced technologies based on three-phase system having the CO_2 both in gas and liquid phases, the CO_2 dissolved in the electrolyte is the main source for the CO_2RR. The electrolyte carries out several functions: guarantees the close of the electrical circuit between working and counter electrode, pairs the charge distribution between the electrodes through the ions migration and permits a correct measurement of the applied working electrode potential measuring the difference with the reference one.

Next to these proprieties, the electrolyte is also the main source of the substrate of interest. This is the main drawback and limitation about CO_2RR. Indeed, CO_2 shows critically low solubility in water-based electrolyte, the benchmark solvent due to availability and recyclability, reaching a poor concentration of only 33 mmol L^{-1} at and at 25°C and 100 kPa[16]. Moreover, hydrogen evolution reaction (HER) from protons reduction is extremely accessible (Table 1) and the H^+ concentration is high in acid and neutral pH. The HER is indeed considered a competitive reaction of the CO_2RR. The solubility limit of 35 mmol L^{-1} is translated into a limit current density reachable for the CO_2RR electrolysis (20 mA cm^{-2}) due to mass transport limitation. This means that at higher current densities, inevitably the HER rate would increase.

HCO_3^- and CO_3^{2-} are the main forms in which CO_2 can be found in water as shown in Figure 2. Such substrates have no record of possible electrolysis[17]. Common CO_2RR studies use pure CO_2 source as reagent batch to compensate such limited solubility. Moreover, higher CO_2 molar flow rates are correlated to higher CO_2RR rates and consequently lower fraction of actual CO_2 converted[18].

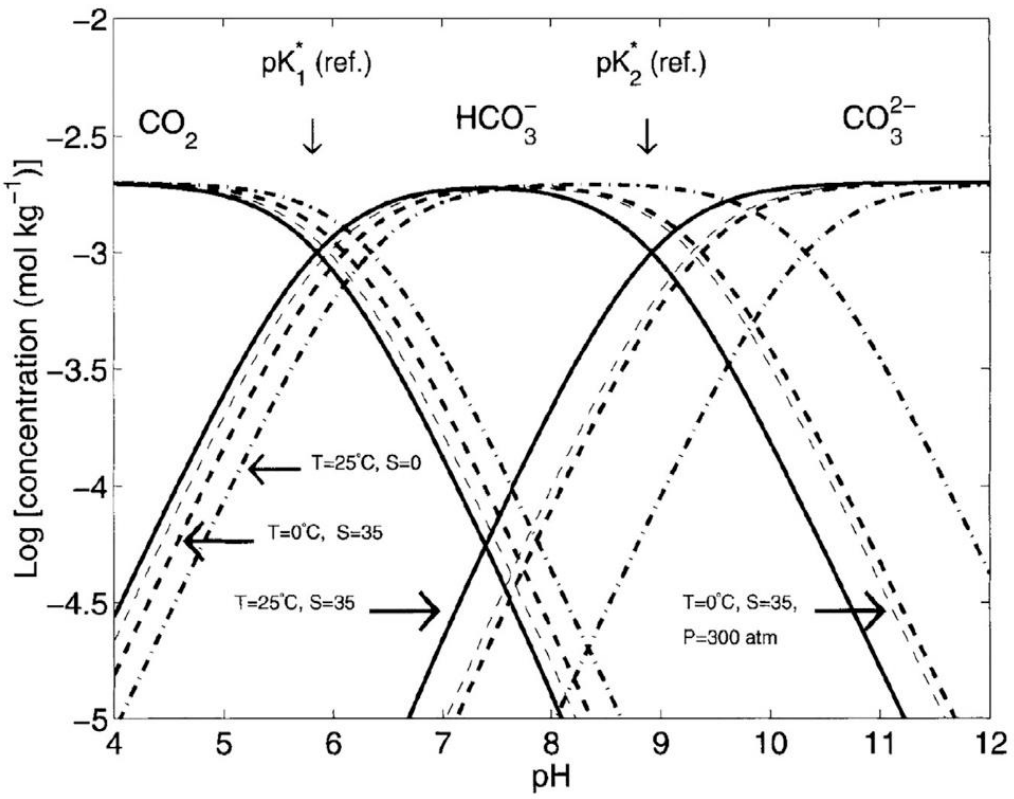

Figure 2: Solubility of CO_2 in water as a function of the pH value at indicated temperature, salinity, and pressure. Reproduced with permission from ref. 24. Copyright © 1969, Elsevier.

Temperature and pressure are the physical variables characterizing any gas solubility in the solvents. As reported in Figure 2, increased temperature generally reduces the CO_2 solubility, while increased pressure act in the opposite direction. In literature several approaches for low temperature electrolysis are present[19,20] especially if combined with the use of organic solvents characterized by a minor specific heat capacity compared to water. Even if less frequent, also high pressure electrolysis are reported[21]. In order to obtain a lower temperature, further energy input is required, those involving a minor energy efficiency of the system. More feasible design allowing high-pressure setup can be designed, even reaching extreme conditions e.g. use of supercritical CO_2 ($scCO_2$) directly as electrolyte. Supercritical solvents manifest the low viscosity typical of gas phase parallel to the high density of liquids, all beneficial characteristics for the electrolysis. Like several other organic solvents, the $scCO_2$ is a perfect aprotic solvent, this involves the presence of a proton donor in order to achieve hydrogenated species. Nevertheless, if organic compounds are characterized by a poor

conductivity, the $scCO_2$ shows an even lower applicability under this aspect[22]. Additionally, the application of supercritical fluids resulted quite aggressive promoting the metal corrosion of the electrodes which eventually precipitate as carbonate salt[23].

1.3 Electrolyte

Several strategies are used in order to increase carbon dioxide solubility, such as the type of electrolyte, the working pH, the temperature and the pressure. Moreover, additional aspects come from the operational working condition and performances. The electrolyte choice is the easiest approach to tune the CO_2 solubility. Several organic solvents show major solubility of carbon dioxide compared to water, creating a more concentrated environment of such substrate[24].

1.3.1 Organic solvent

Solvents like acetonitrile (ACN) and tetrahydrofuran (THF) show 10 times higher CO_2 solubility compared to water-based electrolytes (respectively 314 and 313 mmol L^{-1})[24]. Such characteristic partially benefits the electrolysis but involves some differences in the catalysis. Due to the aprotic nature of ACN and THF, the PCET cannot occur during a catalytic process, since no protons are available in case of pure organic solvent. The most retained intermediate is the $CO_2^{\cdot-}$ radical anion, which requires really negative potential (Table 1), and can produce only carbon monoxide and oxalate. A common procedure in literature is the employment of mixed solvents between the aprotic organic ACN/THF with a second protic solvent like water, methanol (MeOH), organic acids and so on. The conductivity of the organic solvents is an extremely important limitation since the number of inert salts able to be dissolved in such solvents is quite narrow. The actually employed are lithium salts having inorganic counter ions, like the $LiClO_4$, $LiPF_6$, $LiBF_4$ and Li_2SO_4, and tetra ammonium salts having several counter ions, R_4N^+. Common characteristic of these salts is their modest solubility, which limits the possible current density for the electrolysis. Among all of them, the tetra ammonium salts stand out for a supposed role as co-catalyst for CO_2RR due to a characteristic ability to stabilize the $CO_2^{\cdot-}$ intermediate or to act as a single electron transfer specie. The main evidence of such propriety is found out in the production of CO and oxalate with the same electrode comparing the tetra ammonium salt with the family of lithium salts.[25,26]

1.3.2 Ionic Liquids

Another approach is the use of ionic liquids (ILs), peculiar salts that are liquid at temperature below 100 °C and sometimes also at room temperature (RT). ILs are characterized by a low vapour pressure. Due to their interaction with carbon dioxide, ILs are considered useful also to the CO_2RR. Once dissolved in the electrolyte or used as solvent itself, the employment of ILs resulted to drastically increase the conductivity and the CO_2 concentration in the solution[27,28,29,30]. Nevertheless, different publications claim the role of ILs is not limited to the increased CO_2 solubility rather than to work as co-catalyst stabilizing the $CO_2^{\cdot-}$ radical anion; in a similar way to the tetra ammonium salt employed with organic solvent. At the time of the writing, despite the peculiarity of such salts, their application resulted limited, due to their price, their viscosity as pure solvent and the competition with other electrochemical setup, later illustrated, that overcome their benefits.

1.4 pH

Regarding the CO_2 solubility in CO_2RR the most important parameter is probably the bulk solution pH. As we can see in the water-carbon dioxide Pourbaix diagram (Figure 3), the competition between CO_2RR and HER is strictly related to the pH of the solution. As the pH increases in value, also the required potential for the HER increases (red line). This is well explained by the Nernst equation in which a lower concentration of protons inevitably favours the CO_2RR (eq. 1).

$$E = E° - \frac{RT}{zF} * ln \frac{aRed}{aOx} \qquad \text{Equation 1}$$

Where the concentration of H^+ are present in the numerator of the logarithmic part (aRed).

At low pH the HER is thus favored thanks to the minor required potential, moreover the hydrogenated reduced carbon dioxide products become favorable. This is true until the pH gets lower than 4 and CO production becomes thermodynamically favored. Since a high pH resulted in a major required potential for HER, is seems to be convenient to work in such conditions in order to optimize the CO_2RR. Unfortunately

this is only partially true because, from the CO_2 solubility diagram (Figure 2), at pH ≥ 9 the presence of dissolved carbon dioxide reaches zero and only inorganic carbon HCO_3^-/CO_3^{2-} is present.

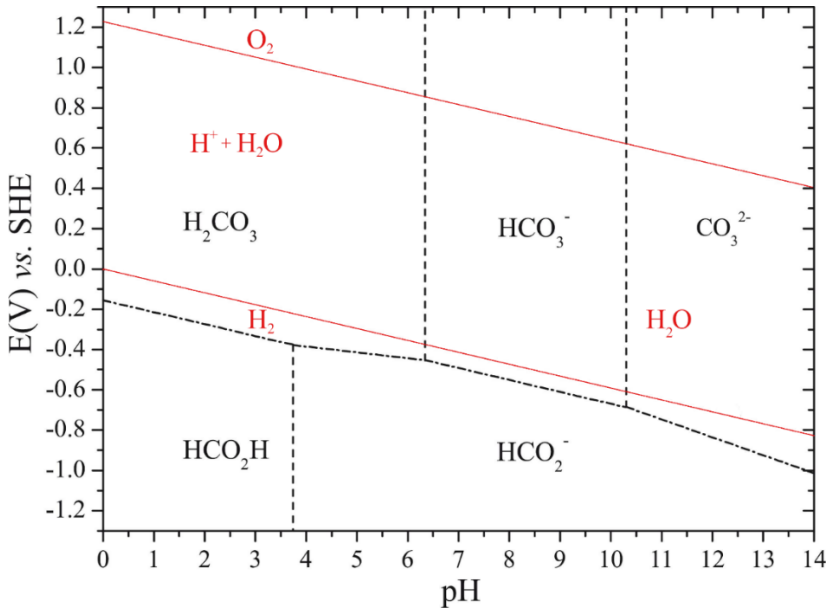

Figure 3: Water-carbon dioxide Pourbaix diagram.

We have seen the chemical composition in which the CO_2 is present in the solution is strictly correlated to the pH; nevertheless, the latter is not a fixed parameter in the time, but it is rather perturbed by the electrolysis itself. Once a bias is imposed on an electrochemical system, inside the solution different regions appear according to the distance from the electrodes. Two main regions can be found: the *Stern layer* and the *diffuse layer*. The Stern layer is the region of electrolyte closest to the electrode and can be further divided in the *Inner Helmholtz Plane* (IHP) and the *Outer Helmholtz Plane* (OHP). In the former, the ions are adsorbed on the electrode surface, promoted by charge and chemical interaction, and grows parallel to the applied bias. In the latter hydrated ions and not adsorbed water molecules are present and free to move[31] (Figure 4). Different mathematical models describe the presence of the so-called *double layer capacitance* due to the presence of actual adsorbed ions and hydrated ones. External to the Stern level there is the diffuse layer having a larger size compared to the former. This layer directly confines with the bulk electrolyte of the entire cell. The reactants mass transport limit is indeed defined as the energy barrier that a substrate must win to

move from the diffuse layer to the Stern one. The mass transport limit is actually the main limitation of all the electrochemical processes.

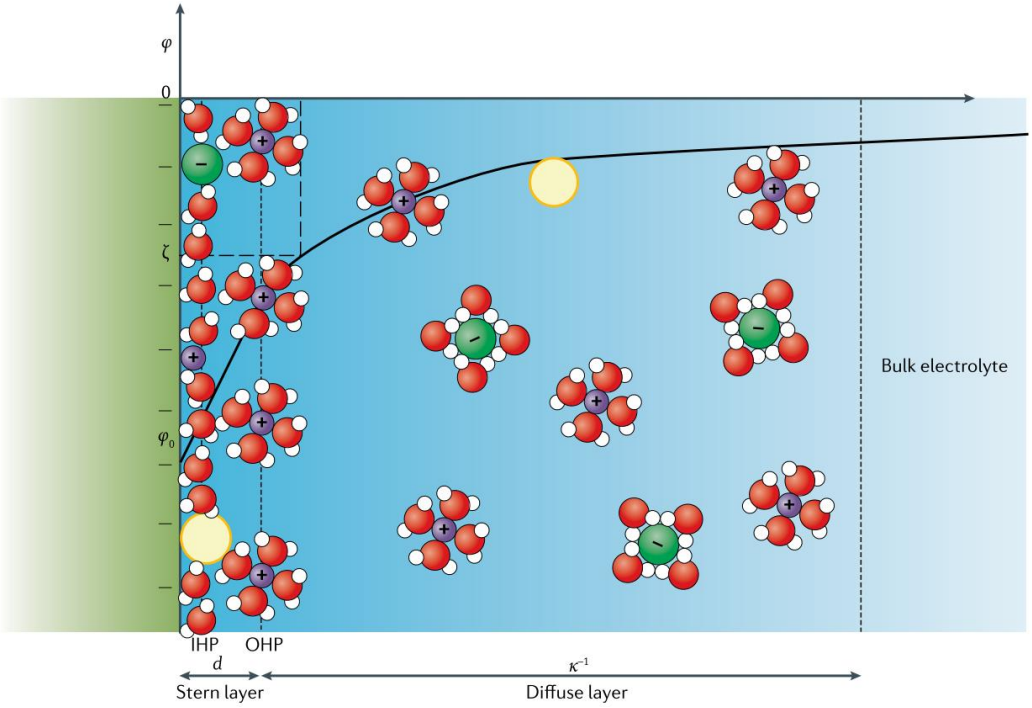

Figure 4: Classical mean-field description of the electrical double layer based on the Gouy–Chapman– Stern model. Are reported the inner Helmholtz plane (IHP) and the outer Helmholtz plane (OHP) forming the Stern layer, externally the diffuse layer. Reproduced with permission from ref. 31, Copyright © 2021, Springer Nature Limited.

The correlation between the activity and pH is evidenced locally on the IHP. As long the H^+ and CO_2 reduction proceed in the Stern layer, also the OH^- anions are produced, as previously reported (Table 1), rising the pH in the HIP respect to the current density of the electrolysis. There is an intrinsic limit current density possible for the CO_2RR due to the extreme local basic pH formed that would reduce the CO_2 solubility near the electrode. Indeed, the OH^- ions would react with CO_2 to form HCO_3^- /CO_3^{2-}, not reducible chemical species. Generally, we can affirm that a change of the surface pH, respect to bulk pH, happens when the consumption rate of local protons exceeds the mass transport of the protons from the bulk solution[32]. Such aspect remarks

how much the pH governs the overall catalysis and circularly, the catalysis perturbs the pH itself.

1.5 Membrane

The membranes are intrinsically connected to the electrochemical setup (1.6) and their development has a common route. Chambers separation is the main role of membranes, nevertheless ions permeability is an essential prerequisite in order to guarantee a close circuit of the cell. The electric fields push the ions towards the opposite electrodes during an electrolysis process. The membranes prevent from electrolytes mixing while allowing ions permeability. For electrocatalytic studies carried out in organic solvent, common ionomers are not compatible, for stability problem in specific solvents and for their necessity to be hydrated. The common membranes require a good grade of hydration to be performant, using organic solvent the amount of water inevitably would decrease for gradient transport inside the electrolyte.

1.5.1 Glass frit

The choice of porous glass frit is the common solution for organic solvents. They do not totally prevent liquid mixing, permitting a partial contact between the two solutions inside the porous channel of the glass matrix[33]. The two solution have only a diffusion-limited contact which permits the ions exchange. Porous glass frits are versatile but not well performing, they introduce a really high resistance in the cell, which makes them accessible only for elementary studies and not for actual applications.

1.5.2 Cationic Exchange membrane (CEM)

Solid ionomer membranes are a more consolidated choice used to completely separate working and counter electrodes in aqueous-based electrolytes. These membranes are classified according to the type of permeable ions: cationic exchange membranes (CEM), anionic exchange membranes (AEM) and bipolar exchange membranes (BPM). The CEM are ionomers in which cations can migrated inside the

membrane, blocking neutral and negative compounds. A subclass of the CEM is the protonic exchange membranes (PEM) able to exchange only protons. In Figure 5a is reported a schematic representation of a Nafion membrane, the most known and employed PEM, based on a tetrafluoroethylene unit having pendant sulfonic groups (-SO_3H)[34].

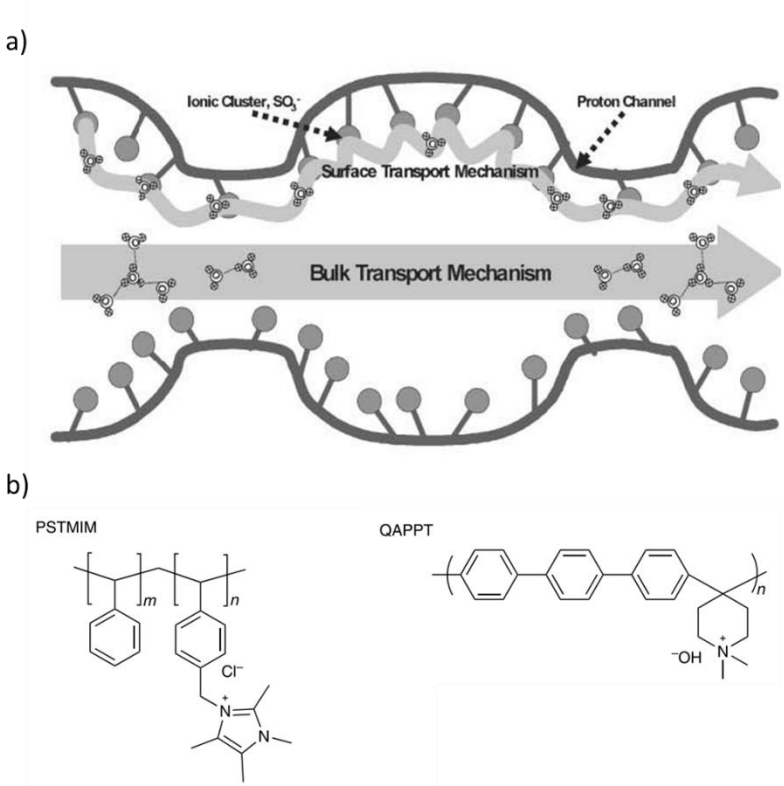

Figure 5: a) Nafion membrane proton transfer mechanism. B) Two examples of Anionic exchange membrane. Reproduced with permission from ref. 34. Copyright © 2005, The Royal Society of Chemistry.

These chemical groups, represented as circles, can exchange protons one to another under a bias and gradient concentration, making possible their transfer in the two electrolytes. PEMs are extensively used in fuel cell application in which they have reached a great optimization. In the CO_2RR literature instead, PEMs have still several limitations. Being able to promote protons migration from anode to cathode they accelerate the competitive HER[35]. The optimal ionic conduction for PEMs is in acidic environment, a challenging condition for usual CO_2RR. Nevertheless, recent studies performed by Sergeant et al. showed how at extremely high current density (> 1 A cm^{-2}) the intense local OH^- production near the first layer of the electrode induces a neutral/basic pH, a favourable condition for the CO_2RR, this even if the bulk electrolyte

is actually characterized by an overall low pH[32]. This is the optimized condition in order to have protonated products likes CH_4. PEM results advantageous in case of formate and oxalate production. Due to the anionic nature of these reduced products, their impossibility to migrate and get re-oxidize in the anode is of great interest.

1.5.3 Anionic exchange membrane (AEM)

In the case of AEM conductive mechanism is specular exploiting cationic ionomer to attract the anions, e.g. Sustanion™ membranes, a polystyrene polymer having imidazolate functionalities, interact with anions thanks to the aromatic positively charged present in the ionomer, Figure 5b. The AEMs are considered the benchmark membranes employed in flow cell configuration once coupled with basic electrolytes, which drastically reduce the HER minimizing protons concentration and avoiding their migration from anode to cathode[35]. Nevertheless, compared to PEMs, AEMs still show low conductivity and selectivity. Many anionic species can permeate the membrane, including HCO_3^- and CO_3^{2-}, causing crossover. Moreover, HCO_3^- and CO_3^{2-} anions are characterized by a lower flow rate compared to the OH^- and cause aggregation of bulky anions on membrane, preventing further migration of OH^- in the anodic compartment where the OH^- accumulation involves further production of carbonates, in a circular deterioration spiral.

1.5.4 Bipolar Membrane (BPM)

The integration of a cathodic exchange layer (CEL) and an anodic exchange layer (AEL) in a shared Interfacial Layer (IL), or bipolar junction, generates the Bipolar Membrane (BPM). BPMs do not let ions permeate across the membrane, they perform a disproportion reaction in which water is converted into H^+ and OH^- or viceversa[36]. Such reaction is different from the one normally occurring at the electrode since no gas evolution occurs. The BPM can work with two different configurations[36] as schematized in Figure 6. The *Reverse Bias* configuration is reported in Figure 6a, the CEL faces the cathode and the AEL faces the anode, as a consequence, the ions produced in the two chambers cannot migrate through their respecting layers. In order to balance the charge, water disproportion into H^+ and OH^- occurs inside the IL (requiring +0.8 V of bias) and the ions migrate the opportune layers. Membrane hydration is required to maintain the disproportion[36]. A different configuration, denoted as *Forward Bias,* faces the AEL to the cathode and the CEL to the anode,

Figure 6b. In this scheme, the OH^- produced at the cathode will permit the AEL reaching the IL, analogously the H^+ produced at the anode will permeate the CEL recombining with the counter ion producing water. The two configurations have different behaviours. In the Forward bias the ions converge in the IL showing low resistance, in the Reverse Bias it is necessary a bias involving high resistance with a drastically current rise once H^+ and OH^- are produced. The main used BPM is composed of a polystyrene polymer which is functionalized on both the CEM and AEM layers. For CEM, the sulfonic group is the main choice[37], nevertheless some formulas having the phosphonic and carboxylic groups are known. Polystyrene is not the only support used for CEM, compositions based on phenylene oxide[38], sodium alginate[39], modified chitosan[40], polyvinyl chloride[41] and polyether ether ketone[42] are known. For the AEL the typical functionalization is based on quaternary ammonium on the polystyrene matrix[43], further efforts lead to the fabrication with ternary/secondary amines and several diamine. Moreover, different matrixes for AEL are the polysulfone, polyvinylidene fluoride (PVDF) and several co-polymers.

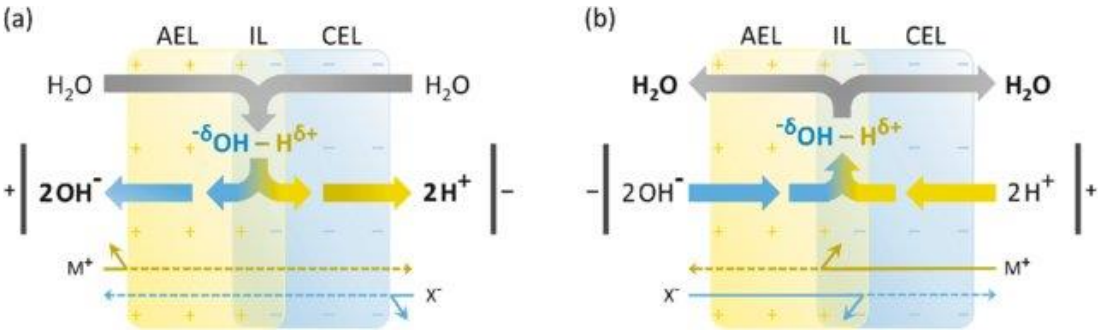

Figure 6: Schematic representation of a bipolar membrane. A) under reverse bias and b) forward bias. Reproduced with permission from ref. 36, Copyrights © 2020, Elsevier.

1.6 Electrochemical setup

Many variables define the CO_2 reduction: the thermodynamic, the CO_2 solubility, the mass transport limitation, and so on. In order to optimize the CO_2RR considering all these aspects an engineering optimization of the electrolyzer is required. Many possible setup configurations were already studied, and further research is still on going. In order to have a preliminary commercial technology for the CO_2RR electrolyzer, several requirements must be satisfied: current density > 200 mA cm^{-2}, high selectivity of faradaic efficiency (FE) > 80%, restrained cell potential < 3V and extended working operation time of months/years[44]. All these aspects are actually not

matched at the same time in any existing setup. Nevertheless it is expected that further contributes would be implemented in the next future in terms of CO_2 conversion rate and energy efficiency of the technology[45]. An ideal electrochemical scheme would work avoiding pure CO_2, in order to contain the upstream CO_2 capture cost[46,47], moreover should be able to completely convert the CO_2 furnished. However, the actual literature suggests the major FE values are obtained using concentrated CO_2 gas stream, lowering the overall carbon conversion in the process[46,48,49,50]. The setup must be able to minimize the mass transport limitation of the substrate of interest and a proper control of the pH must be guaranteed since a low pH would favour the HER and a high one would reduce the carbon dioxide available. The main known electrochemical configurations are reported below with a detailed analysis of benefits and disadvantages.

1.6.1 Close cell setup

It is the easiest configuration and is mainly employed in the elementary studies. In this scheme, the anode and cathode are immersed in a common electrolyte. The cell is refilled with saturated electrolyte previously purged with CO_2. The electrolysis is performed for a fixed short time, gas composition and the electrolyte are analysed only at the end of the test to quantify the products. This configuration has many limits: cross reaction of products occurs between the electrodes, so reduced products can be re-oxidized, the amount of gas dissolved in the electrolyte is not renewed limiting the CO_2 availability along the time, the electrolyte composition changes during the time in case of liquid products. This setup results to be quite rudimental and is commonly reported for elementary studies.

1.6.2 Batch cell setup

This configuration, commonly reported as H-cell electrolyzer due to the classic form of the cell (Figure 7a), introduces the benefit of electrode separation through an ions exchange membrane between the chambers (membranes and frit glass separator will be detailed in the next session). The membrane reduces the cross-reaction problem, except for permeable ionic products, and renew the dissolved CO_2 through a continuous gas flow inside the solution, which further guarantees a higher current density and faradic efficiency. Such open setup permits also the ongoing gas products monitoring

by gas-chromatography (GC). Several limitations are still present in this configuration, due to the low solubility of CO_2. Indeed, even considering a stationary saturated solution, the limiting achievable current density is still lower than 20 mA cm^{-2}. Nevertheless, requiring a reference electrode, inevitably placed at high distance, a further Ohmic contribute limits the applied voltage. Being the batch cell the most studied configuration, several optimizations able to increase the setup performances are present in literature. The electrolyte composition is the main contribute studied for the optimization. Highly buffer electrolytes are utilized in order to decrease the competitive HER and increase the CO_2 solubility. The employment of ionic liquids (Ils), as pure electrolytes or additives, shows modest benefits. Optimized batch cell configuration introduces the possibility to work at higher pressure and lower temperature, which improves the CO_2 solubility. Nevertheless, once taking in the consideration the current density performances, such improvements result to be marginal since the CO_2 mass transfer from the bulk solution to the electrode is not improved.

1.6.3 Flow cell electrolyzer

A great improvement in CO_2RR was the introduction of flow cell configuration built around the innovation of gas diffusion layer (GDL) beside the catalyst. GDL brings to the CO_2 electrocatalysis a great improvement, making the current collector both hydrophobic and gas permeable. In this way, the cathodic reaction switches from being only a mere liquid phase reduction counting only dissolved CO_2, to the reduction of CO_2 both in liquid and gas phases (Figure 7b). The hydrophobic layer inside the GDL inhibits the electrolyte flow across the electrode while the porous layer makes possible CO_2 back flow the electrode, drastically reducing the mass transport limitation. The GDL introduction, tremendously extends the performances of the CO_2RR allowing current density over 200 mA cm^{-2}. This is possible without lowering the selectivity since the CO_2 reservoir it is not restricted to the one solubilized in the electrolyte but it comes directly as gas phase. Moreover, the flow electrolyzer commonly benefits to the circulation of the electrolyte, making it possible to operate with highly concentrated electrolytes. Indeed, the latter guarantees higher current densities, reduces the Ohmic resistance and limits the HER in favour of CO_2RR. The most optimized flow cell electrolyzer configuration uses concentrated KOH solution, from 1 M to extremely basic 12 M, in order to eradicate the HER and register extremely high current densities. However basic solutions have a controversial role: they reduce the HER limiting the H^+ concentration although also increasing the CO_2 loss due to its reaction with the hydroxide. For every $2e^-$ paired electrons transfer related to CO_2RR,

one hydroxide anion is formed and reacts with a second CO_2. This involves that only a 50% of CO_2 utilization efficiency for CO_2RR[51] as reported in the following:

$$CO_2 + H_2O + 2e^- \rightarrow CO + 2OH^-$$

$$2OH^-_{(aq)} + CO_2 \rightarrow CO_3^{2-}{}_{(aq)} + H_2O \qquad \text{Equation 3}$$

A high conversion rate would correspond to bicarbonate crystals precipitation. The employment of humidified CO_2 stream is a common procedure in order to reduce such problem. The benefits of a basic electrolyte push the preparation of AEM for flow reactors. Such membranes guarantee better performances in terms of resistance and consequent current density at high pH, nevertheless they implicate a further loss of CO_2 utilization efficiency being anion permeable. The carbonate/bicarbonate formed from hydroxide reaction can indeed permeate the membrane reaching the anodic compartment in which they will be reconverted in gaseous CO_2 once reacting with protons, lowering the cathodic amount available:

$$CO_3^{2-}{}_{(cathode)} \rightarrow CO_3^{2-}{}_{(anode)}$$

$$H_2O \rightarrow O_2 + 4H^+ + 4e^-$$

$$CO_3^{2-} + 2H^+ \rightarrow H_2CO_3 \rightarrow CO_2 + H_2O \qquad \text{Equation 4}$$

In order to decrease the so called "CO_2 crossover", CO_2RR in high acidic media flow reactor was also tested with current density major of 1 A cm^{-2}, reaching 50% of FE for mixture of C_{2+} products and operating cell voltage of 4.2 V. Indeed, at such high current density, the local hydroxide production on the electrode surface switches the pH from acid to neutral and even basic values. Locally on the electrode the HER is prevented meanwhile the bulk pH guarantees the carbonate depletion before reaching the crossover[32]. Flow reactors were deeply studied also for other fundamental aspects concerning the GDE. Thinner GDE seems to guarantee a higher CO_2 concentration near the catalyst, suppressing more efficiently the HER[52,53]. Moreover, they promote single carbon reduced products (C_1) rather than larger carbon chain (C_{2+}) thanks to the competition in the binding sites between CO_2 and CO. On the other hand, thicker electrodes involve a major permanence time of the chemical species. This is translated in a major permanence time for CO that can promote C_{2+} products, instead higher OH^- dually lowers the HER and CO_2 availability. The polymer additive employed in the electrode fabrication has shown to increase the gas permeability and consequently the

CO_2 mass transport[54,51,54]. Ionomer additives alter the hydrophobicity of the electrode which is translated in a more effective bubble removal on catalyst surface. The presence of a gas phase limits the accessible area of the electrode with a consequent energy losses of the 20% for industrial electrolyzer[55]. Last parameter is the electrode wettability. The electrodes require hydration to guarantee the ionic conductivity, avoiding the catalyst deactivation. Wettability of the electrode increases under potential[56,57] becoming more hydrated and unbalancing the three-phase system in which solid, liquid and gas phases are combined[58,59]. In order to introduce hydrophobicity on the GDL, polytetrafluoroethylene (PTFE) deposition is the common procedure. The PTFE amount is a critical aspect, parallel to the hydrophobicity, also the electrical resistance[60] and the electrode fabrication cost increases with its introduction[61].

At the time of writing, the energy efficiency of flow-cell electrolyzer can reach the 20%[62], which is still low and overestimated since all the calculations are commonly iR compensated and the oxygen evolution reaction overpotential is approximated to zero[63,64]. Moreover, the actual scale up of this configuration shows some limitations regarding the high amount of electrolyte involved and its regeneration.

1.6.4 Zero-gap electrolyzer

Commonly reported as membrane electrode assembly cell (MEA-cell) or improperly fuel-cell-like[65], since is the typical configuration used in the fuel cell application, this configuration has the peculiarity to work without the catholyte, having the catalysts layer separated just by the membrane. Indeed, the name zero-gap comes from the proximity of the cathode to the membrane, of few micrometers, and to the anode, of few millimeters, which improves the setup performances reducing the Ohmic resistance (Figure 7c) and the resulting operating voltage. To reduce to the micrometer scale the distance between cathode and membrane, a mechanical contact induced by high pressure and temperature is applied to them[66]. Several combinations of temperature, pressure and time result in different performances which are also connected to the nature of the membrane[67]. Such close contact led to the configuration in which the electrolyte on the cathode compartments is absent using only gaseous CO_2 as substrate and receiving ions from the membrane. In the anode compartment instead, the electrolyte is often preserved. Typical highly conductive electrolytes, like the

hydroxides KOH and CsOH, are employed, less frequently carbonate salt $KHCO_3$ and $CsHCO_3$ are utilized. The first investigation of CO_2RR with zero-gap configuration used the PEM fuel-cell scheme. Here a Nafion proton exchange membrane was placed between the electrodes. This configuration for CO_2RR cannot guarantee the same performances as the fuel cell application, due to the intrinsic evolution of HER during the exchange of protons directly on the GDE of the cathode[68,69,70]. Nevertheless, there are still studies in which this membrane are applied with zero-gap configuration in order to reach possible hydrogenated products of interest[68], when liquid anionic products are obtained ($HCOO^-$) and also supporting the system with solid electrolytes.

The larger part of the literature employs AEM in CO_2RR with zero-gap configuration. Even if more versatile regarding the promotion of CO_2RR, they are not free of any drawback. Indeed, like in the microfluidic setups, parts of the CO_2 will react to produce CO_3^{2-} anions able to permeate the AEM. Moreover, there is a problem of cations migration from the anode to the cathode. This migration led to the local precipitation of carbonate salts, both inside and on the surface of the GDE, which lowers the active surface of the electrode mining the operational performances[65]. The regeneration of the electrode is possible only on the surface with the passage of pure water, but it is more complicated for the residual salt removal inside the electrode. In order to extend the operational time of work, humidified CO_2 can also be used at cost of lowering the performance of the cell[65]. Working with diluted anolyte can prolong the lifetime of salts precipitation but does not deny it.

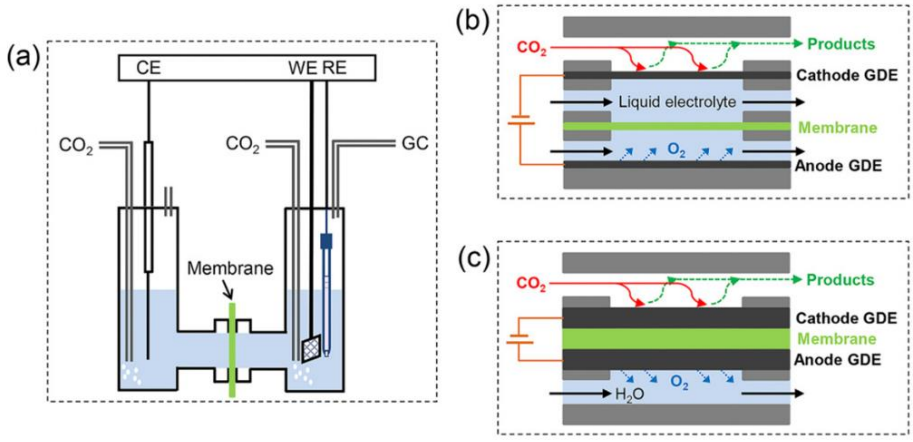

Figure 7: Electrochemical setups for the conversion of CO_2. A) Batch cell, b) Flow cell and c) Zero-gap configuration. Reproduced with permission from ref. 66. Copyright © 2021, Acta Physico Chimico Sinica.

A more complex configuration of zero-gap electrolyzer would implement a further element: the solid-state electrolytes (SSE). The introduction of such components can be useful to concentrate the liquid products and removing the liquid phase in the anode. Several schemes are reported in literature employing SSE combined with the presence of both a cationic CEM and an AEM facing respectively the anode and cathode. A first example is the one reported in Figure 8a, SSE is placed at the center of the scheme between the CEM and AEM. Here the $HCOO^-$ coming from the cathode encounters the H^+ coming from the anode; the resulting HCOOH is being concentrated and flow away by a N_2 stream or diluted with a water flow which characterizes the final concentration of the chemical. Higher FEs for liquid products are achieved at higher amount of water, at expanse of the final product concentration. This method was indeed optimized for the HCOOH production on a Bi nanosheet catalyst on the cathode. The highest FEs exceedes 95% with a current densities of 50 mA cm^{-2}. Instead the highest concentration of HCCOH, 12 M product solution, was reached with a drastic decrease of selectivity to a value of 40%[71]. The introduction of a second membrane and a SSE inevitably involves a major operating voltage for the cell, which requires values major of 3 V; nevertheless the SSE introduction leads to more stable electrolysis processes. Indeed, with a superior configuration reported in Figure 8b, the same electrocatalysis was able to reach 150 mA cm^{-2} and operating work of more than 20h[71]. In such configuration an AEM and CEM membranes are facing the cathode and anode, next to both membranes are collocated two different SSE, one cationic conductive and the other anionic conductive, which are separated by a BPM. With this approach, concentrated HCOOH and KOH are obtained.

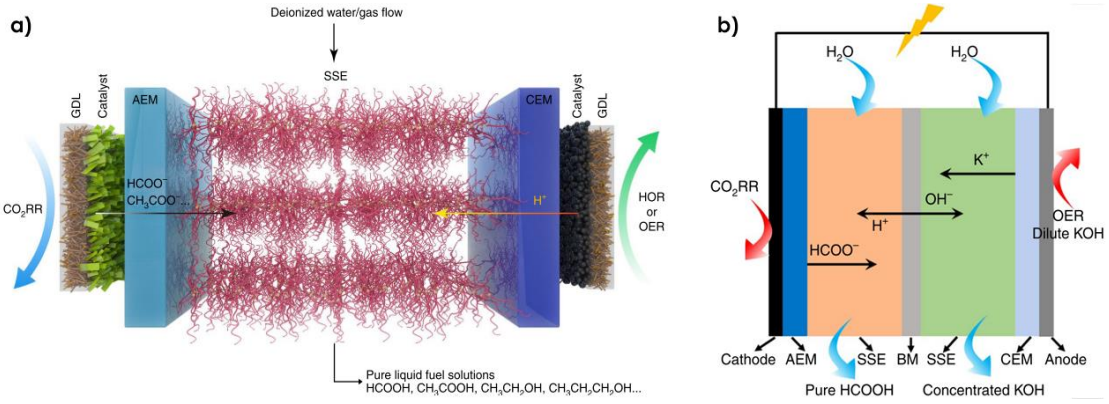

Figure 8: Zero-gap configuration variations. Reproduced with permission from ref. 71. Copyright © 2019, Springer Nature.

The implementation of SSE can lead to the elimination of the electrolyte phase in the anolyte and guarantee the concentration of liquid products on the system[72]. This approach is more similar to PEM-Fuel Cell, in which no liquid electrolyte is present. Nevertheless, it seems that the presence of a liquid electrolyte can guarantee better performances once we switch to gaseous products rather than liquid one[65].

The working temperature is also a parameter that can greatly influence the zero-gap electrolyzer performances. If in the flow cell setup, higher temperature means lower solubility of CO_2, in the case of zero-gap configuration that cannot happen since the cathode's electrolyte is missing. There is anyway a correlation between working temperature and required voltage for zero-gap electrolyzer. As illustrated in Figure 9, in a zero-gap electrolyzer having gold nanoparticles at the cathode working at a stable current density of 0.1 A cm^{-2}, as the temperature increases the operating voltage decrease[73]. This is due to better kinetic reactions rate at higher temperature; nevertheless, the FE for the CO shows a drastic decrease, since it is the thermodynamic favorite product compared to HER.

The zero-gap configuration is promising compared to the previous setup or in general compared to the microfluidic systems, however the partial/total absence of the electrolyte is the main limitation in terms of performances. It is believed that the presence of cations adsorbed in front of the cathode induces an increase in current density[74]. In the zero-gap configuration, being the anolyte a hydroxide solution, there is an activation time in which cations reach the GDE in the cathode and make it possible a current increase[65].

Once the products purification is taken into consideration, the promising scheme of zero-gap electrolyzer seems to be dominant. Nevertheless, the actual performances of such electrolyzer are still lower compared to the flow cell one. In a comparative study[71], a bismuth nanoparticles catalyst tested in a flow cell shows a great selectivity of 97% once the potential is pushed at more negative potential than -0.8 V vs RHE. Fixing a current density of 0.50 A cm^{-2} in a 1 M $KHCO_3$ electrolyte, a FE for formate reaches 92% of selectivity for the flow cell. In the case of zero-gap electrolyzer, a smaller current density of 0.42 A cm^{-2} was reached with only 80% of FE. In general, there are a lot of differences which make difficult to compare the two systems in terms of performances. Generally can be compared for the selectivity of a

desired product fixing the current density, in case of mono chamber, or the applied voltage, for the complete cell.

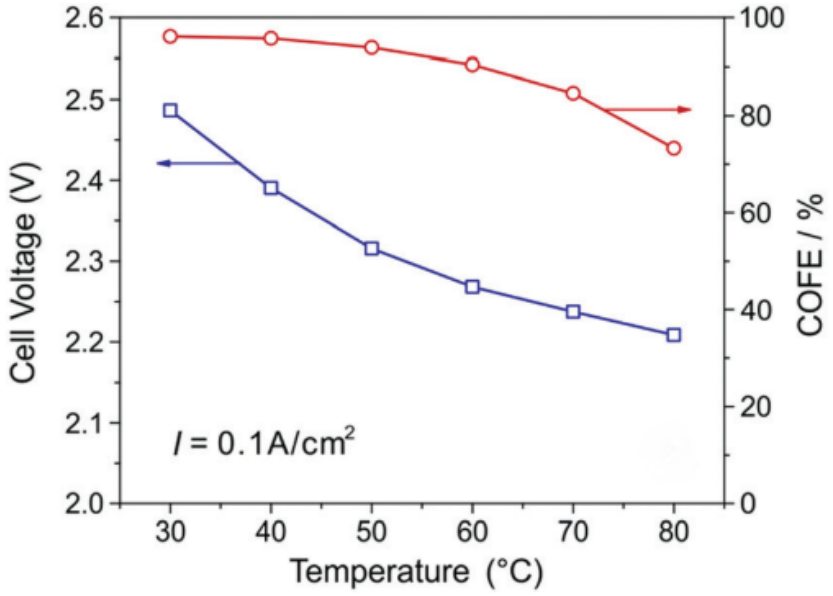

Figure 9: The zero-gap electrolyzer working at different temperatures. Reported cell voltage (blue line) and CO selectivity (red line) at a constant current density of 0.1 A cm^{-2}. Reproduced with permission from ref. 73. Copyright © 2019, RSC Publishing.

1.7 CO_2RR Catalyst

In the previous part, the electrochemical conversion of CO_2 was analysed under several aspects. The importance of CO_2 solubility and its interconnection with different contributions like pH, nature of the solvent, physical variables such as temperature and pressure were underlined. Different technological strategies to mitigate these aspects were introduced in the form of possible electrolyzer setups and the consequent membrane coupling. Nevertheless, in this discussion the role of the catalyst was intentionally omitted.

Discussion of the catalysts known to perform the CO_2RR open a wide new dissertation. Indeed, once we consider the cathodic reaction, different energy barriers appear both for the HER and CO_2RR depending on the catalyst choice. A wide variety of catalysts known to perform such reaction exists and their comparison is quite hard. As discussed in the previous sessions, the performances regarding the CO_2RR are not merely restricted to the chemical composition of the cathode, thus to the catalysis, but

also due to all the operative working conditions and the cell configuration employed. This makes difficult to compare different catalysts unless all the other variables coincide.

Narrowing down to heterogeneous catalysts, being the only one showing possible industrial application, the metal/metalloid atoms of the IIIA and IVA groups are known to be selective for CO_2RR in favour of $HCOO^-$. This peculiar selectivity does not come from a major affinity towards the CO_2, rather than an actual overpotential for the HER[75]. Catalysts based on Au[76], Ag[77], Pd[78], Zn[79] particles are known to be selective for the CO production at different conditions, instead only copper-based catalysts seem to be able to coordinate CO without releasing and thus proceeding in its reduction to more complex products likes CH_4, CH_3OH, EtOH, BuOH, C_2H_4 and so on[80,81]. Metal and metal oxide particles (Figure 10a) as a wide class of materials, characterized by different sizes from micro to nanoscale, through different and variegated morphologies, are considered the benchmark catalysts for the electrochemical reduction of CO_2.

Different approaches try to disassemble the idea of catalyst as metal cluster agglomeration and point towards materials bearing single metal active sites. The best example of this strategy is the one of the Me-N-C materials (Figure 10b). Characterized by a graphitic carbon material reminding the structure of the graphene, they are rich of nitrogen atoms in form of pyridinic, pyrollic, quaternary-N amine and pyridine-N-oxide. Part of these chemical groups are responsible of single metal cations coordination, eventually incorporating these atoms inside the carbon support. These materials are promising for their low employment of metal atoms and the organic support can be prepared through organic waste treatment. In terms of catalysis, at the time of writing, they result able to produce only CO bearing cheap metals like Mn, Co, Cu, Zn, Ni and Fe[82]. Among them, Ni-N-C resulted highly selective for CO production at several potentials, instead the Fe-N-C is the one requiring the lowest potential in order to reach a modest CO selectivity.

A further approach more similar to homogeneous catalysis, is the employment of Metal Organic Framework (MOF) and Covalent Organic Framework (COF) as catalysts for CO_2RR (Figure 10c). Indeed, single metal atoms, commonly in form of cations, are stabilized by organic ligands in an ordered and periodic structures. This class of compounds is less studied compared to Me-N-C, nevertheless some peculiar results are present. Several COFs incorporating metal porphyrins are known to be

active catalyst for the production of CO with high faradaic efficiency[83,84,85,86] and also the case of a Cu^{2+} based MOF able to produce CH_4 at high selectivity [87]. For this class of compounds, the main limitation is on the active species characterization, since the operando techniques under potential are not actually spread and ex situ investigations of the catalyst are commonly avoided. The metal organic compound is often considered the true-catalyst even though cations reduction and metal agglomeration can easily occur several times, hiding the nature of the real active site.

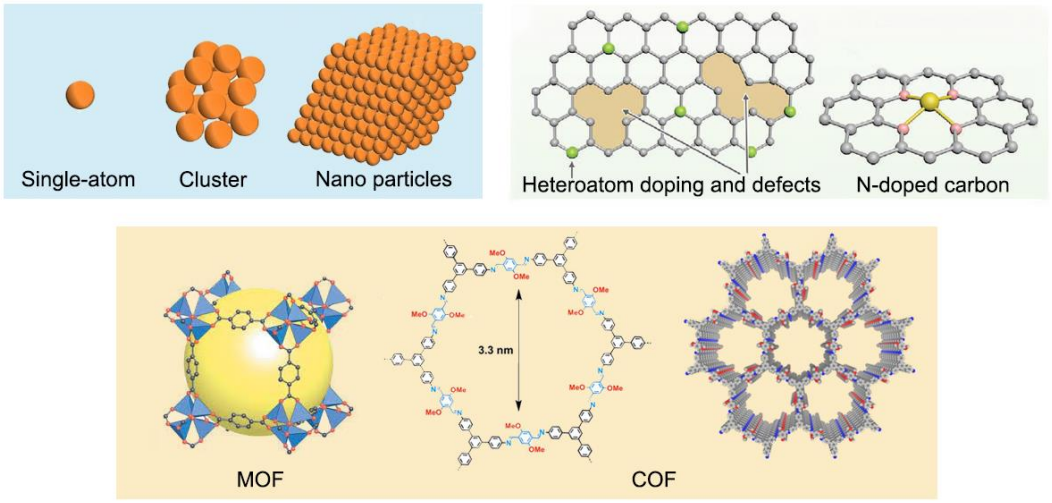

Figure 10: Different type of heterogeneous catalysts. a) single atom, cluster and nano particles, b) Me-N-C catalysts ad c) MOF and COF representations.

During my PhD several attempts to prepare single metal catalysts were performed, charactering and testing them for the electrochemical conversion of CO_2. Such investigation was conducted in parallel with the electrochemical setup engineering that could drastically enhances the performances. In the next chapters, four different classes of materials were investigated.

Chapter 2

Experimental Procedures

In this chapter, all the analytical technique employed during the experiments will be reported in details. The techniques are divided in two separated groups: the chemical/physical and the electrochemical characterizations.

2.1 Chemical and physical analysis

All the studied catalysts required the combinations of several techniques in order to understand the chemical composition of the main support, typically organic, and additionally specific ones for the active site characterization.

2.1.1 Attenuated Total Reflectance Fourier Transform Infrared spectroscopy (ATR-FT-IR)

Infrared spectroscopy is an essential analytical technique necessary for the characterization of organic compounds and several inorganic ones. The ATR analysis was performed on a Bruker Tensor II in attenuated total reflectance configuration, in which the sample powder was placed directly on the ATR crystal without any further preparation and then collecting the spectra. Powder samples need to be preferentially dried in order to avoid extended bands due to the water absorption. Through the infrared spectroscopy, several chemical groups were identified, assessing the correct synthesis of the samples. ATR spectroscopy does not furnishes quantitative information, rather than gives detailed qualitative information of specific bonds present in the sample, drastically helping in the characterization of the compound.

2.1.2 UV-Vis spectroscopy and Diffuse Reflectance Measurement

UV-Vis spectroscopy is a versatile technique applied for several samples; the main requisite is the sample absorption in the region of the visible-ultraviolet. The spectroscopy was employed with two different configurations on a LAMBDA™ 650 S spectrometer. For soluble catalysts the spectra was recorded in the absorption mode, in which the powder was dissolved in a proper organic solvent. For our studies N-Methyl-2-pyrrolidone (NMP) was commonly employed. The absorption of the catalyst dissolved subtracted by the blank (NMP itself) was measured. The catalysts were prepared simply by solubilization and dilution at the concentration necessary to not have saturated spectra. The main catalysts studied are heterogeneous solid compounds difficult to be solubilize without losing information and damaging the material. For such compounds, the diffuse reflectance measurement was employed instead. In this configuration the detector does not register the spectrum that has partially absorbed by the sample, rather the reflected light by an opaque solid sample once it is being illuminated. With the reflectance configuration, catalyst powder must be prepared as a flat surface to be irradiated; the common procedure employed was the pressing of the powder in form of pallet or alternatively a drop casting filming on a PTFE support.

2.1.3 Powder X-Ray Diffraction (XRD)

XRD analysis was abundantly employed in order to investigate the possible crystallinity of samples and also for their ex situ characterization after their electrolysis performance. Indeed, several compounds bear active sites formed by single metal cations. An ex situ analysis aims to identify the possible clustering of metal nanoparticles caused by the electrolysis process. The diffraction pattern was recorded in Bragg-Brentano symmetric geometry by using a PANalyti-cal X'Pert Pro instrument (Cu-Ka radiation, 40 kV and 30 mA) equipped with an X'Celerator detector. Dried powder was collected and placed on the top of the sample holder making a flat and homogeneous deposition on it previously the measurement.

2.1.4 X-Ray Photoelectron Spectroscopy (XPS)

XPS analysis furnishes elementary analysis of the sample and gives further details about the chemical composition of metal atom sites other than for the organic

counterpart. Parallel to the XRD investigation, also the XPS resulted essential for the ex-situ investigation after the electrochemical test. X-Ray spectroscopy was performed on a PHI 5000 Versaprobe spectrometer (Physical Electronics), equipped with monochromatic Al K-alpha X-ray source (1486.6 eV). Surface charge compensation was obtained with a combined system, based on an electron gun and Ar^+ ion gun. Survey and high resolution (HR) spectra were acquired using pass energy (PE) values of 187.85 and 23.50 eV, respectively. The calibration of the binding energy (BE) scale was obtained by setting the C-C component of the C1s region to 284.6 eV. Casa XPS software was used for the analysis of the experimental data. The Shirley background function was subtracted from HR spectra to remove the background signal.

2.1.5 Field-Emission Scanning Electron Microscopy (FE-SEM)

FE-SEM imaging investigation was employed in order to visualize the three-dimensional morphologies of the samples collected, the homogeneity of the prepared electrodes and to characterize ex-situ the catalysts to search possible metal and metal oxide nanoparticles. The images were recorded on a ZEISS Supra 40 FESEM with the following configuration: SE2 detector for secondary-electron imaging, BSE detector for back-scattered electron imaging, Si(Li) Oxford Instruments detector for Energy-Dispersive X-ray (EDX) Spectroscopy. In details, the SE2 detector was deeply employed in order to detect metal atoms having a heavy Z number and easily identify metal atoms clusters. EDX-mapping introduce further information regarding the homogeneity of the metal active site dispersion on the catalysts.

2.1.6 Brunauer–Emmett–Teller surface analysis (BET)

BET analysis was performed on crystalline catalysts showing high internal surfaces. The specific surface area and the macro/micropore volume/area of the crystals were measured using a Micromeritics gas adsorption analyzer ASAP 2020 Plus 2.00 instrument equipped with commercial software for calculation and analysis. The BET surface area was calculated from the adsorption isotherms using the standard Brunauer–Emmett–Teller (BET) equation. The mesopore and micropore volume was obtained using a BJH plot.

2.1.7 Thermo-Gravimetric and Evolved Gas Analyses (TGA-EGA)

TGA were carried out on a Netzsch TG 209 F1 Libra while EGA was conducted by means of a Bruker Tensor II infrared spectrophotometer equipped with vapour phase accessory heated at 220 °C and DTGS detector. The two instruments were coupled by a heated (220 °C) gas transfer line. About 10 mg of sample were placed in an alumina pan and heated up to 800°C in nitrogen flow (40 ml min^{-1}) followed by an 15 minutes long isotherm.

2.2 Electrochemical Analysis

Under the voice of electrochemical analyses are include all the characterization techniques necessary to investigate the catalyst behaviour under a bias and additionally the instruments necessary during electrolysis experiment building the electrochemical setup.

2.2.1 Cyclic Voltammetry (CV)

CV technique is considered one of the fundamental analysis regarding the electrochemical studies relate to the electrocatalysts. It can furnish detailed information about stability and reaction mechanism for homogeneous catalysts, i.e. dissolved in the electrolyte, and minor information about the selectivity between HER and CO_2RR for heterogeneous one. In a classic experimental configuration of the latter, the electrolyte solution is purged with N_2/Ar flow in order to completely remove any trace of dissolved CO_2 in the electrolyte. In such electrolyte, a scanning potential is plotted against the current for the electrode bearing the catalyst of interest and the same procedure is then repeated once reached a complete saturation of CO_2 inside the electrolyte. From a mechanism point of view, from CV it is possible to reveal the oxidation/reduction of active species inside the solution, their reversibility and possible change once the CO_2 is introduced in the system. Regarding the selectivity, the two currents are than superimposed and analysed.

In case of aqueous electrolyte, the potential should be reported versus the Reverse Hydrogen Electrode (RHE) since the dissolution of CO_2 in water involves carbonic acid production which lowers the pH. The variation of the pH causes a more difficult

interpretation of the voltammograms, since HER and CO_2RR are competing reaction, is quite common to register higher current densities in CO_2 saturated solution rather than in N_2/Ar, caused by a major protons concentration and consequent HER rate. CV technique can furnish important information regarding the potential necessary to the catalysis and discriminate the regions in which the major difference among the two atmospheres became relevant. Such electrochemical characterization was performed in a three-electrode H-type cell at room temperature with a Metrohm Multi Autolab/M101 potentiostat. As working electrode was used a catalyst-coated carbon paper with a small geometric area of 0.15 cm^2. A Pt wire was used as counter electrode and an Ag/AgCl (3 M NaCl) was used as reference electrode in the experiment. A membrane (Nafion™ Membrane N117, Sigma-Aldrich) was employed to separate the cathodic and anodic compartments. CV measurements were generally performed from +0.5 to -1.2 V vs Reversible Hydrogen Electrode (RHE) at a scan rate of 10 mV s^{-1} in N_2- and CO_2-saturated solution flowing the proper gas at 5 mL min^{-1} in a 0.1 M $KHCO_3$ aqueous solution.

2.2.2 Electrochemical Impedance Spectroscopy (EIS)

The electrochemical characterization was performed in a three-electrode H-type cell at room temperature with the same setup employed for the CV, both the cell and the potentiostat. To determine the double-layer capacitance of the electrode, several CV were executed in a potential range in which no reactions occur at scan rates of 2 mV s^{-1}, 5 mV s^{-1}, 10 mV s^{-1}, 25 mV s^{-1}, 50 mV s^{-1}, 75 mV s^{-1} and 100 mV s^{-1} always under a N_2-saturated atmosphere in 0.1 M $KHCO_3$ aqueous solution. EIS measurements were performed at various potentials, typically from -0.19 V to -0.99 V, with an AC signal of 10 mV of amplitude and 1 - 105 Hz frequency range in N_2- and CO_2-saturated 0.1 M $KHCO_3$ aqueous solutions.

2.2.3 Chronoamperometry (CA) and electrochemical setup

The chronoamperometry (CA) is the heart of the electrochemical analysis. Indeed, applying a bias to the working electrode of interest and tracking parallelly the products

and the current density along the time, we are able to completely characterize the possible CO_2RR of each catalyst.

The overall electrochemical setup follows the scheme reported in Figure 11. The actual scheme falls into the category of microfluidic flow cell where the prefix micro stands for the reduced dimension of the plates and flows involved on a lab scale. In this setup, two different reservoirs were employed with different combination of $KHCO_3$ solutions, from the lowest of 0.05 M to higher concentration of 2 M. All the studies exploit continuous flows of pure CO_2 in both the cathode and anode chambers, in the case of the former, the flows do not pass directly through the solution rather than the back of a GDE as a characteristic of the flow cell. The electrochemical setup is composed of a CHI 760D (CH Instruments, Inc.) potentiostat in a customized two-compartment cell (ElectroCell™) with a proton exchange membrane (Nafion Membrane N117, Ion Power) or an anionic exchange membrane (Sustanion X37 from DioxideMaterials or Fumasep FAA-3-PK-130).

Both cathodic and anodic compartments are refilled continuously with two separated reservoirs of electrolyte through the employment of a mechanical pump. The usual flow is set at 2 mL min^{-1}. A catalyst-coated carbon paper (GDL28 SIGRACET 28BC, SGL Technologies) of 1.5 cm^2 was used as the working electrode whereas a 4 cm^2 Pt foil is the chosen counter electrode, an Ag/AgCl (1 mm, leak-free LF-1) electrode is used as reference electrode. Gas-phase products were analyzed on-line by a micro gas chromatograph (μGC, Fusion®, INFICON) placed directly in the outgoing channel of the microfluidic cell.

The GC is equipped with two separated channels mounting a 10 m Rt-Molsieve 5A column and an 8 m Rt-Q-Bond column and two micro thermal conductivity detectors (micro-TCD) at the end of each column. The inlet of the μGC equipment was connected to the cathodic side of the electrochemical cell through a GENIE filter to remove the humidity from the gas and possible solid contamination.

During the CA measurements, a constant CO_2 flow rate in the range of 5-25 ml min^{-1} was maintained on the back site of the electrode (gas-diffusion layer) to assure the reactant supply and to bring the gaseous products to the μGC. Liquid products were analyzed ex situ by a High-Performance Liquid Chromatograph (Thermo Scientific Ultimate3000 HPLC) with a UV-Vis Detector set at 210 nm by using a ReproGel (300 × 8 mm) column, with 9.0 mM H_2SO_4 (flow rate of 1.0 mL min^{-1}) as mobile phase.

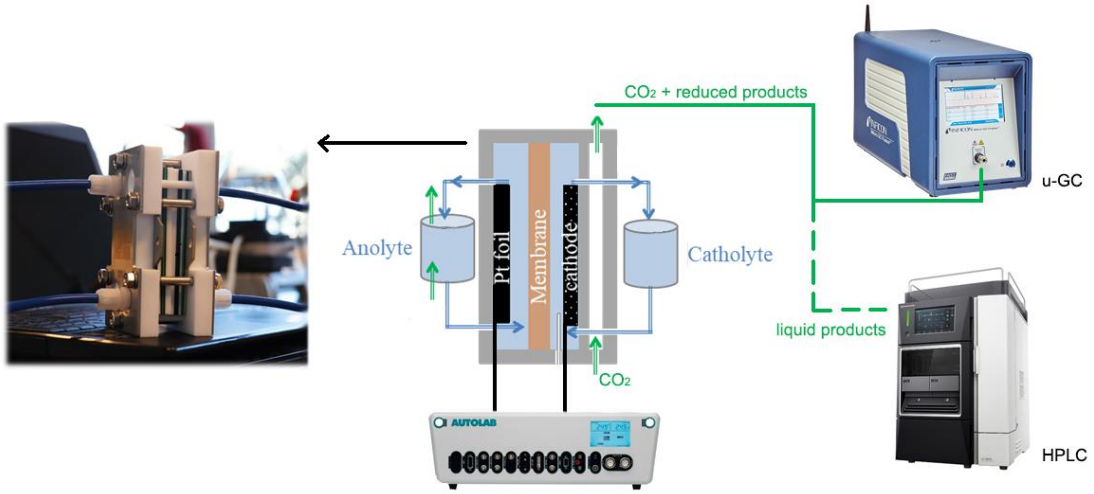

Figure 11: Electrochemical setup configuration.

The catalysts are always tested as a GDEs, i.e. depositing the catalyst of interest on a GDL (gas diffusion layer, GDL; SIGRACET 28BC, SGL Technologies) in order to fabricate hydrophobic and gas permeable electrodes. All the catalysts were deposited by drop casting technique in which the powder, together with possible additivities, is dispersed in an organic solvent making a slurry which will be deposited on a the GDL surface. Once the ink is completely dried, a homogeneous flat deposition is formed on the GDL surface. The drop casting technique shows good accessibility in terms of practical operation, do not require a previous filtering of the dispersion or peculiar steps for the deposition. Nevertheless, it results a technique employable only for small dimension electrodes. Indeed, once the electrode became larger, the deposition homogeneity got lost and more specific technique should be applied. The common procedure utilizes 1 or 2 mg of catalyst dispersed in 160 µL of ethanol (EtOH) by sonication. Related to the specific study, also some additives were employed, like the ionomer Nafion or carbon black powder (CB, Shawinigan Black AB50).

In a conventional experiment, the information obtained from a previous CV furnish the range of potentials in which CO_2RR can be registered with a good rate of conversion. Several combinations of potentials and electrolyte are studied and compared in order to reach the optimal condition for the CO_2RR and the selectivity of specific products in case of multi-products production.

In order to evaluate the FEs for each product, different calculations are performed for gaseous and liquid molecules. Nevertheless, all the potential must be compared to the RHE considering the pH of each electrolyte as reported in the following equation:

$$E(Ag/AgCl) = E(RHE) - 0.059 * pH - E^0(Ag/AgCl) \qquad \text{Equation 5}$$

The selectivities of the products are reported in terms of Faradic Efficiency (FE), thus matching the percentage of electron employed to the concentration of products itself, thus not involving the ratio between the CO_2 furnished compared to the actual reacted. Equation 6 and equation 7 correspond to the formula utilized respectively for gaseous and liquid products:

$$FE = \frac{Q*\%*n*F}{Vm*i} \qquad \text{Equation 6}$$

$$FE = mol * n * \frac{F}{C} \qquad \text{Equation 7}$$

Where the letters stand for:

Q = gas flow rate

% = concentration in molar percentage of gas products

n = number of electrons required for the specific product

F = Faraday constant

Vm = molar volume

i = current intensity

mol = mol of obtained products

C = total charge accumulated

2.3 Computational details

2.3.1 Molecular chemical potentials

In this section, the details present in the DFT calculation of modelled materials are reported. The chemical potential (μ_M) of a molecule M at standard conditions and in the gas phase (g) is

$$\mu_{M(g)} = E_M^{DFT} + E_M^{ZPE} + H^{\circ}_{M(g)} - T^0 S^{\circ}_{M(g)} \qquad \text{Equation 8}$$

where the gas phase standard enthalpy and entropy, $H^{\circ}_{M(g)}$, and entropy, $S^{\circ}_{M(g)}$ are reported in thermochemical tables[88]. In liquid phase or in aqueous solution, the chemical potential is obtained as

$$\mu_{M(l/aq)} = \mu_{M(g)} + \Delta G^f_{M(l/aq)} - \Delta G^f_{M(g)} \qquad \text{Equation 9}$$

in which $\Delta G^f_{M(l/aq)}$ is the Gibbs free energy of formation of the molecule in liquid phase or aqueous solution. From thermochemical databases we can get $\Delta G^f_{M(l/aq)}$ and $\Delta G^f_{M(g)}$.

2.3.2 Molecule corrections

In Density Functional Theory, the PBE functional introduces systematic errors in the total energies of species containing double and triple bonds between carbon and oxygen, such as CO, CO_2, esters and carboxylic acids (OCO-molecules). To overcome this issue, we adopted a statistical correction strategy[89] based on reaction enthalpies and applied it to CO, CO_2, and OCO-species.

The correction values (γ) introduced to the total energy are

$$\gamma_{CO} = -0.330$$

$$\gamma_{CO2} = 0.092$$

$$\gamma_{OCO} = 0.066$$

The γ_{CO} correction largely dominate over γ_{CO2} and γ_{OCO}.

2.3.3 Solvation energy calculation

Since all reactions take place in an aqueous environment, the contribution of the interaction with the solvent to the energy of the catalyst surface and its adsorbates, named solvation energy (E^{solv}), was computed by means of DFT simulations. In order to estimate this quantity, we used an explicit solvent model, calculating the binding energy of the bare surface and the adsorbate with the maximum number of water molecules that can bind through hydrogen bonds, both in the acceptor and donor configurations.

For each system studied, the first and second hydration shells were recreated by the addition of *n* water molecules ($n \cdot H_2O$) which surround the active site and adsorbates. During the geometry optimization, only water molecules were free to fully relax, and the solvation correction for configuration *i* (E_i^{solv}) was calculated as

$$E_i^{solv} = E_{i+n \cdot H2O}^{DFT} - \left(E_i^{DFT} + E_{n \cdot H2O}^{DFT}\right) \qquad \text{Equation 10}$$

where $E_{i+n \cdot H2O}^{DFT}$ is the total energy DFT of the system including the solvent, while E_i^{DFT} and $E_{n \cdot H2O}^{DFT}$ are energies of the active site (or adsorbate) and the water cluster, respectively.

2.3.4 The Computational Hydrogen Electrode method

The Computational Hydrogen Electrode (CHE) method allows us to determinate the Gibbs free energy profile of a reaction on a given catalyst[90,91,92]. This method assumes that at standard conditions and zero applied electric potential (U = 0 V) with respect to the Reversible Hydrogen Electrode (RHE), the half of a hydrogen molecule chemical potential in the gas form ($1/2\mu_{H2}$) can be used to replace the chemical potential of each proton-electron couple (H^++e^-).

At electric potential U ≠ 0 V vs. RHE, the chemical potential of each (H^++e^-) couple is shifted by −eU. Starting from these considerations, it is possible to compute the thermodynamic onset potential (U^r_{onset}) of each reaction (r) as

$$U^r_{onset} = -\max\frac{\left[\Delta G^r_{ij}(0\ V)\right]}{n_e} \qquad \text{Equation 11}$$

where ΔG^r_{ij} is the free energy variation of a reaction step from state j to state i, while n_e represents the number of electrons exchanged in the step. From the onset potential U^r_{onset} the reaction overpotential (η_r), can be obtained as

$$\eta_r = U^r_{onset} - U^r_0 \qquad \text{Equation 12}$$

where U^r_0 is the equilibrium potential of the reactions.

2.3.5 Reaction Gibbs free energy calculation

The Gibbs free energy variation between two reaction states 1 and 2 ($\Delta G_{1\to2}$, in which 1 corresponds to the starting state and 2 to final ones) can be written as

$$\Delta G_{1\to2} = G_2 - G_1 + (n_2 - n_1)\left(\frac{1}{2}\mu_{H2} - eU\right) \qquad \text{Equation 13}$$

where n_2 and n_1 are the numbers of (H^++e^-) couples in state 2 and 1 respectively, and the free energy of state 1 (or 2) can be expressed as the sum of two thermodynamic contributions, namely

$$G_1 = G_1^{\star+A} + G_1^{g,l,aq} \qquad \text{Equation 14}$$

the $G_1^{\star+A}$ term arises from the surface ($\star$) in presence of a possible adsorbate (A), while $G_1^{g,l,aq}$ takes into accounts species (reactant or products) present in gas (g), liquid (l) or in aqueous solution (aq).

The first term combines the computed total energy DFT (E^{DFT}) with the vibrational Helmholtz free energy (F^{vib}) of the adsorbate and the solvation energy (E^{solv}), that is

$$G_1^{\star+A} = E_1^{DFT} + F_1^{vib} + E_1^{solv} \qquad \text{Equation 15}$$

while the second term is estimated as the total energy E_s^{DFT} of the molecular species combined with chemical potentials and DFT corrections.

Chapter 3

Metal Doped Polyaniline

In this chapter, the electrochemical investigation of Lewis Acids doped polyanilines as catalysts for the CO_2RR will be reported. The interest on developing a material able to sustain single metal active sites, avoiding metal clusters or even bigger nanoparticles agglomerates, led to the choice of polyaniline as mere organic support. Polyanilines are polymers based on the aniline monomers repetition inside the polymeric chain. Their peculiar characteristic resides on this extended aromatic chain in which regions of benzenoid and also quinone units are repeated. Polyanilines are quite popular since they are spread as dye in different manufactories; an aspect which makes them great candidates for possible scale up technology in different fields.

As reported in Figure 12, the polymerization of polyanilines starts by an oxidation step in which the amino group of the aniline monomer forms the radical cation, such step can be performed chemically by a weak oxidant or electrochemically[93]. The obtained radical cation can then react with another radical or with the aniline itself, leading to the polymerization of the chains. At the end of this step, it will be obtained the so called *Emeraldine Salt Polyaniline* (ES-PANI), a green p-doped polymer in which the vacancies delocalized on the polymer rearrange themselves forming a highly conductive species called *bipolaron* state (Figure 12). The same polymer can be deprotonated to form a blue polymer denoted *Emeraldine Base Polyaniline* (EB-PANI) which shows a completely different nature of semiconductor instead. In the EB-PANI benzenoid and quinoid units are both present and through their possible oxidation or reduction, another two additional forms of polyanilines are obtainable. The *Pernigraniline* presenting dominant quinoid units and the *Leucoemeraldine* once the aromaticity is completely obtained on the polymer. These two forms are less stable of the EB-PANI, so they are difficult to preserve. We can divide all these forms in two groups: the undoped ones in which are present the EB-PANI, the leucoemeraldine and the pernigraniline, and the doped one in which the proton-doped ES-PANI is allocated. Other than protons, several Lewis Acids were previously used as dopants for the polymer[94,95,96,97]. Aiming to fabricate single metal active sites, several doped polyaniline were produced and investigated as catalysts for the CO_2RR.

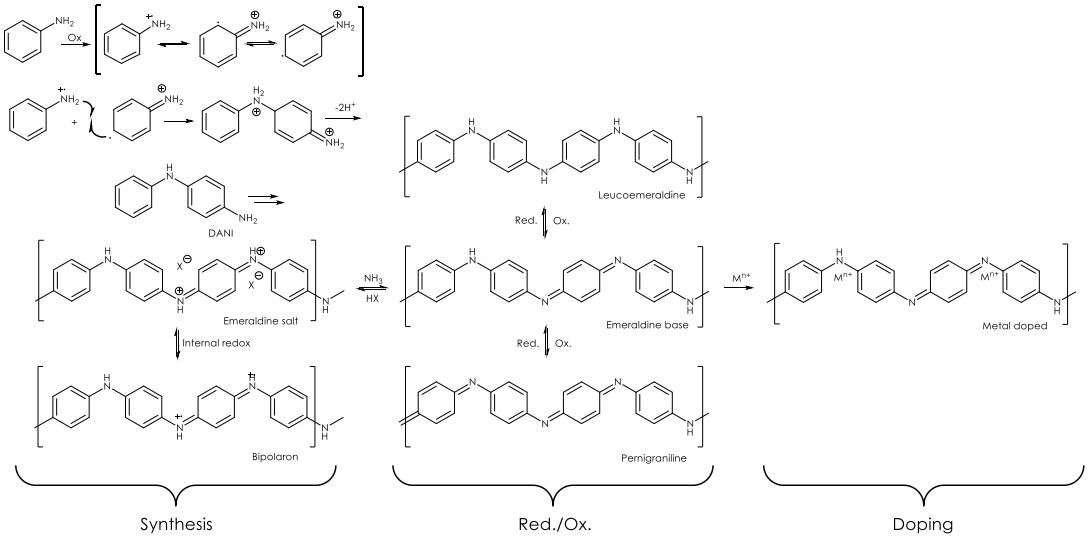

Figure 12: Reaction mechanism of polyaniline synthesis and the possible forms obtainable.

3.1 Doped polyanilines synthesis

All the reagents employed for the synthesis were purchased from from Merck and used without further purification. In details, the N-phenyl-1,4-phenylenediamine (DANI, 98%), copper (II) chloride ($CuCl_2$, 99%), iron (III) chloride ($FeCl_3.6H_2O$, 97%), manganese (II) chloride ($MnCl_2$, 99%), tin (IV) chloride ($SnCl_4.5H_2O$, 98%), zinc (II) chloride ($ZnCl_2$, 99%), ammoniumpersulfate (APS, $(NH_4)_2S_2O_8$, 98%), methanol (MeOH, 99.9%), N-methyl-2-pyrrolidinone (NMP, 99.5%), hydrochloric acid fuming (HCl, 37%), potassium bromide (KBr, 99%), NafionTM 117 containing solution (5% in a mixture of lower aliphatic alcohols and water) were used.

The first step of the synthesis involves the polymerization of the DANI, the aniline dimer, in the form of ES-PANI. The choice to start with the dimer rather than the monomer comes from two separated reasons. The aniline is a toxic molecule which requires more precaution, at difference to the relative dimer, and its distillation as purification step just before its employment. Moreover, the dimerization step is the one characterized by the highest barrier energy, thus fastening the overall reaction. The polymerization was performed chemically in a batch reaction using DANI (5 gr, 27.1 mmol) and an excess amount of APS (9.29 gr, 40.7 mmol) as oxidizing agent. The DANI was firstly dissolved in 15 mL of solution 70:30 v/v MeOH:H_2O with 1% w/w of HCl and placed in an ice bath under stirring, while APS was dissolved in analogous 5 mL of the same solution

separately. Successively, the APS solution was slowly added dropwise into the DANI solution all along in 5 minutes and kept under stirring for 3 hours at room temperature (RT). As soon as the APS solution makes contact with the former, a green solution start appearing became darker as long the APS solution is being dropped, finally a dark green precipitate was formed. The precipitate was then filtered, washed several times with a solution 70:30 MeOH:H_2O (in order to dissolve the low molecular weight polymers) and then dried at 60 °C.

In order to obtain the semiconductive form of EB-PANI in a second step reaction, the powder was dispersed in 40 mL of ammonia 32% solution and stirred overnight in order to neutralize the protons present as dopant on the polymer. As soon as the precipitate makes contact with the basic solution, a fast color change occurs, turning the green solution into a deep blue color. The obtained powder is filtered and washed with water several times and dried at 60 °C. The passage from ES-PANI to EB-PANI is essential in order to achieve a possible doping with Lewis acids. Among all the possible cations, the protons are the one having the more concentrated charge and the lowest dimension, which makes them the best candidate for doping compared to any other cations. So, it is essential to remove as much H^+ dopant as possible in order to achieve a possible doping with different cations. The final doping step was performed dissolving 100 mg (around 1 mmol) of EB-PANI and 11 mmol of the relative metal salt ($MnCl_2$, $CuCl_2$, $SnCl_4.6H_2O$, $FeCl_3$ or $ZnCl_2$) in 20 mL of MeOH and stirred at 60 °C overnight. The solution was then diluted in water to promote the M-PANI re-precipitation. The obtained powder was thus filtered, washed several times with water in order to remove any residual trace salts, and then dried overnight at 60 °C. Those samples were then denoted as Mn-PANI, Cu-PANI, Sn-PANI, Fe-PANI and Zn-PANI.

3.2 Physical and Chemical Characterizations

The obtained PANIs were then characterized. We will anticipate that all along the different characterizations it was clearly assessed that among all the samples, only Mn-PANI, Cu- PANI, Sn- PANI and Fe-PANI were actually doped polyanilines, different case was the one regarding Zn cations in which a heterogeneous materials bearing ZnO particles grown on EB-PANI was found. Since the failure to reach a Zn-doping on PANI sample, its electrochemical performance was then omitted.

3.2.1 ATR

With the ATR spectroscopy is possible to analyse the correct polymerization of the monomer forming the polyaniline and to guarantee its preservation after the doping step.

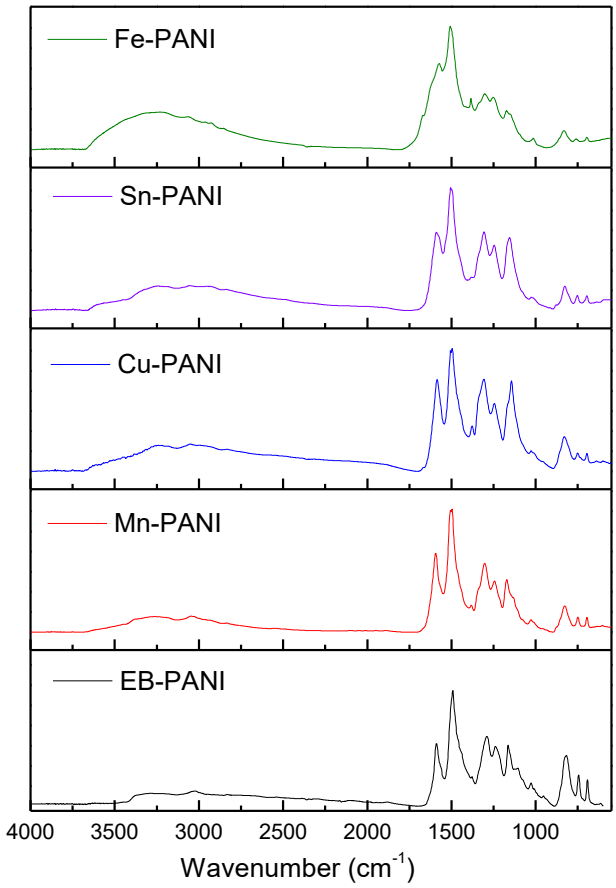

Figure 13: ATR spectra of EB-PANI (black), Mn-PANI (red), Cu-PANI (blue), Sn-PANI (purple) and Fe-PANI (green). Reproduced with permission from ref. 61. Copyright © 2021, Springer Nature.

As reported in Figure 13, a typical absorption pattern of the polyaniline is observed for each sample. EB-PANI shows the characteristic νN-H at 3172 cm^{-1} stretching of secondary amines, the νC-H at 3031 cm^{-1} stretching of aromatic rings, the νC-N at 1597 cm^{-1} of the benzenoid ring and the νC-C at 1495 cm^{-1} stretching

of the quinoid ring of the polymer chain, the νC-N at 1312 cm^{-1} stretching of aromatic amines, the quinoid ring stretching at 1151 cm^{-1}, and the out of plane bending of para-disubstituted benzene at 819 cm^{-1}. Similar patterns are recorded for the metal-doped PANI samples, indicating good preservation of the polymer chains during the doping reaction without any sign of oxidation.

3.2.2 UV-Vis spectroscopy

The PANIs samples were also investigated through the UV-Vis spectroscopy thank to their peculiar characteristic to absorb in the visible region of the spectra. PANIs sample were dissolved in the NMP solvent and being analysed in absorption mode. The reported spectra are normalized on the first peak in Figure 14.

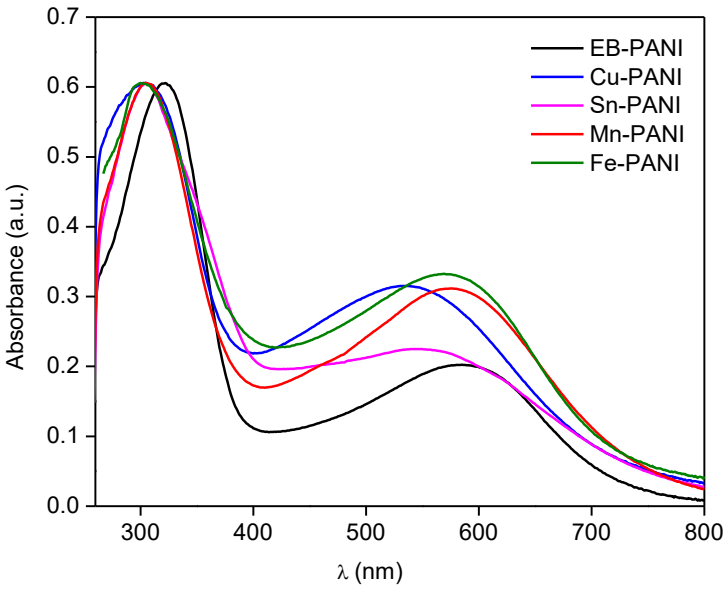

Figure 14: UV-Vis spectra of EB-PANI (black), Mn-PANI (red), Cu-PANI (blue), Sn-PANI (purple) and Fe-PANI (green). Reproduced with permission from ref. 61. Copyright © 2021, Springer Nature.

For all the spectra, a common pattern of two transition is registered: at lower wavelengths, between 300 nm and 350 nm, are present the π-π* transition associated with the benzoid moiety absorption, at higher value between 500 nm and 700 nm, the n-p transitions are present. The absence of the transition at 400-450 nm for all the PANIs, typical of the bipolaron state, suggest that all the materials are emeraldine base polyanilines[98]. The absorption peaks are slightly different for each sample: 322 nm (π-π*) and 585 nm (n-p) for EB-PANI, 305 nm and 534 nm for Cu-

PANI, 305 nm and 548 nm for Sn-PANI, 305 nm and 574 nm for Mn-PANI, 300 nm and 569 nm for Fe-PANI. It is interesting to note that the presence of metal cations leads to a hypsochromic shift (blue shift) for both π-π* and n-p transitions and causes an increase in latter absorption intensity, suggesting that a doping process is involved at different scales for each cations[99].

The peculiar case of Zn-PANI shows already some clues regard its chemical composition. As reported in Figure 15, the ATR and UV-Vis spectroscopies of Zn-PANI are reported. In the ATR spectra, Figure 15a, the polyaniline pattern present also in the other samples is recorded, nevertheless is it possible to detect intensive signals around the 3550 cm^{-1} due to O-H stretching of the superficial hydroxyl groups present on the ZnO. Further evidence can be found looking to the UV-Vis spectra of the Zn-PANI, Figure 15b, where the polymer does not shows a clear hypsochromic shift in the π-π* transition like the other samples, more resembling the one of the EB-PANI instead.

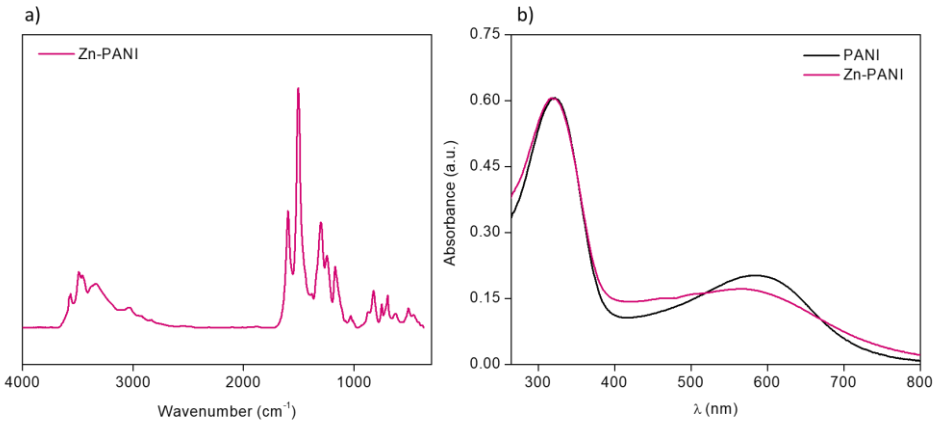

Figure 15: a) ATR and b) UV-Vis spectroscopy of Zn-PANI sample.

3.3.3 XPS and ICP

High-resolution XPS studies were performed in order to validate the correct doping of metal cation on polyaniline sample and to investigate their chemical environment.

For Cu-PANI sample (Figure 16a), the $Cu2p_{3/2}$ peak can be deconvoluted into two main contributions at 932.6 eV (75.6% peak area) and 934.6 eV (24.4% peak

area). Those components can be attributed to Cu(I) and Cu(II), respectively, in accordance with the literature on CuCl[100], $CuCl_2$[101] and Cu-doped polyaniline[102]. Based on the $Sn3d_{5/2}$ peak position (487.3 eV), it is possible to exclude the presence of metallic Sn in the Sn-PANI sample (Figure 16b) but also of SnO and SnO_2 due to the higher value registered[103,104,105], suggesting the presence of tin cations in a different chemical environment. Concerning the Mn-PANI sample (Figure 16c), the identification of the oxidation state of Mn is not straightforward due to its low concentration and the well-known complexity of interpretation of the Mn2p region caused by multiplet-splitting and satellite structure[106]. Based on the estimated binding energy of the $Mn2p_{3/2}$ peak (641.6 eV), the presence of Mn(III) and Mn(IV) seems most probable[107]. Regarding the last sample, Fe-PANI sample (Figure 16d), both the $Fe2p_{3/2}$ peak at a binding energy of 711.2 eV and the presence of characteristic satellite, point to Fe(III), in accordance with the literature on $FeCl_3$[108] and Fe-doped polyaniline[109]. Concisely, detailed XPS analysis unveils that Cu, Sn, Mn and Fe ions are successfully introduced in the EB-PANI as coordinated ions and thus dopants, thought manifesting different ratios.

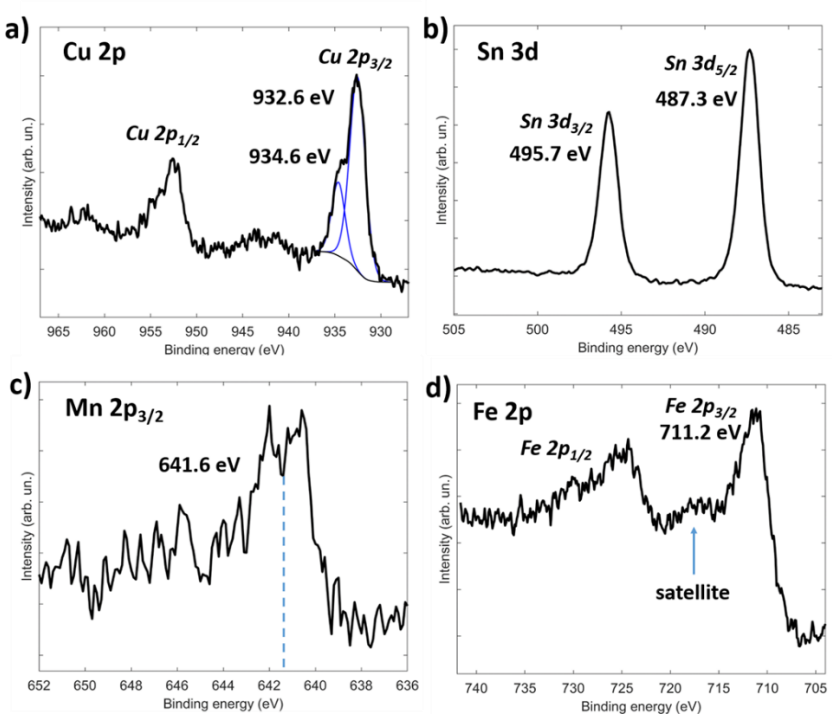

Figure 16: High-resolution XPS acquisitions of the Cu2p, Sn3d, $Mn2p_{3/2}$ and Fe2p regions for samples (a) Cu-PANI, (b) Sn-PANI, (c) Mn-PANI and (d) Fe-PANI. Reproduced with permission from ref. 61. Copyright © 2021, Springer Nature.

The successful incorporation of metal cations is quantified by elementary analysis through the ICP-MS and XPS analysis respectively. The weight percentage of doped metal and the atomic ratio of metal to coordinated nitrogen were quantified and listed in Table 2. It is confirmed that the chemical composition of the synthesized EB-PANI is in accordance with the reported molecular structure[110,111]. The Zn-PANI it is reconfirmed as a dissonant case compared to the other PANIs samples. Indeed, an incredibly higher amount of metal is recorded compared to the other samples, 36.4% in weight, with an irrational value of Zn/N ratio of 1.47 for a mere doping. The metal atoms completely oversteps the number of possible nitrogen atoms available for coordination, thus suggesting the presence of zin atoms in a different chemical environment.

Table 2: Metal percentage by ICP quantification and chemical composition by semi-quantitative high-resolution XPS analysis. Reproduced with permission from ref. 61. Copyright © 2021, Springer Nature.

Sample	ICP	XPS					
	Metal (wt%)	C (at%)	O (at%)	N (at%)	Cl (at%)	Metal (at%)	Metal/N (at%/at%)
EB-PANI	/	80.5 (4) ± 0.4	3.9 (2) ± 0.2	15.2 (4) ± 0.4	0.4 (1) ± 0.1	/	/
Cu-PANI	8.9 ± 1.6	78.3 (7) ± 1.1	6.2 (3) ± 0.3	12.3 (6) ± 1.2	2.5 (1) ± 0.1	0.7 (1) ± 0.1	0.06 (1)
Sn-PANI	6.6 ± 1.1	71.5 (5) ± 0.5	9.8 (3) ± 0.3	11.2 (5) ± 0.5	4.7 (1) ± 0.1	2.8 (1) ± 0.1	0.25 (1)
Mn-PANI	2.2 ± 1.0	80.1 (4) ± 0.5	5.0 (2) ± 0.2	12.9 (5) ± 0.5	1.5 (1) ± 0.1	0.5 (1) ± 0.1	0.04 (1)
Fe-PANI	1.4 ± 1.0	72.0 (4) ± 0.5	13.8 (2) ± 0.2	8.6 (3) ± 0.5	4.6 (1) ± 0.1	1.1 (1) ± 0.1	0.13 (1)
Zn-PANI	36.4 ± 1.0	52.8 (0) ± 0.5	21.3 (1) ± 0.2	8.1 (3) ± 0.5	5.8 (1) ± 0.1	11.9 (1) ± 0.1	1.47 (1)

3.3.4 FE-SEM

Further study on the morphology has been performed by FESEM technique. As shown in Figure 17a-f, where all the images of polyaniline samples are reported.

Considering the undoped form of polyaniline EB-PANI (Figure 17a) a reference for all the other samples, it is possible to detect different dimension of

particles from the microscale and partially lower size and a missing peculiar morphology.

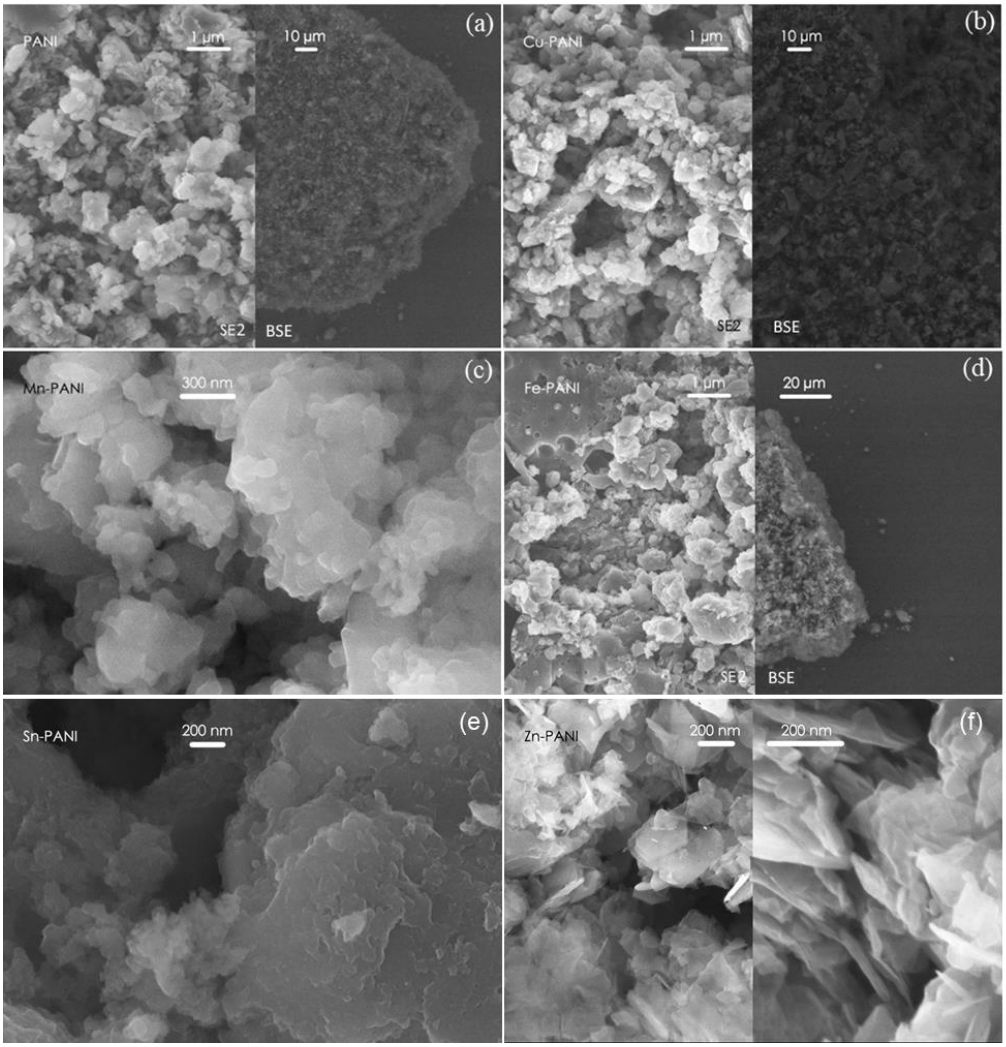

Figure 17: FESEM images of (a) EB-PANI and (b) Sn-PANI. Reproduced with permission from ref. 61. Copyright © 2021, Springer Nature.

All aspect being shared in all the doped PANIs samples. In Figure 17b-e, the doped forms of PANIs are reported and no trace of metal salts precursors is found; justifying the presence of the metal cations only as dopants rather than in the salt or metal oxide forms. This evidence was also supported by secondary electron detector SE2 in which atoms having a high Z number result to be brighter and easier to be recognized. FESEM analysis suggests the presence of metal doping, information perfectly coherent with the one obtained with XPS and UV-Vis analysis. Again, a completely different scenario is presented for Zn-PANI sample, Figure 17f, in this

case ZnO microparticles are clearly visible all over the material, which clarify the high amount of Zn atoms present in the sample by ICP-MS technique.

3.3 Electrochemical characterizations

3.3.1 CV

The activity of PANI-based electrodes was preliminary studied by electrochemical characterizations like Cyclic Voltammetry (CV) and Electrochemical Impendance Spectroscopy (EIS).

Generally, for all the PANIs, the current density registered under N_2 atmosphere is actually higher compared to the one under CO_2 at the same potential vs RHE. This aspect suggests an intrinsic selectivity towards CO_2RR. Indeed, comparing the same potential, the composition of the CO_2-saturated electrolyte involves a higher concentration of protons, which would be translated in an higher current density for HER in case of minor selectivity towards CO_2, instead for all the PANI samples this increment do not occur, suggesting that the active sites are occupied by the CO_2 thus inhibiting the HER. A comparison of all the CVs in CO_2-saturated 0.1 M $KHCO_3$ electrolyte for all the different catalysts are reported in Figure 18a, for the Cu-, Sn- and Fe-PANI, an higher current density is registered comparing to the undoped form of EB-PANI, different scenario is the one of Mn-PANI in which the two currents seems to coincide, probably due to the low concentration of dopant present for Mn cations in the sample (Table 2).

3.3.2 EIS

EIS was performed both in the N_2-purged and CO_2-saturated 0.1 M $KHCO_3$ electrolyte in order to light up the role of the metal cation in polyaniline samples. Representative Nyquist plots of the impedance for the Cu-PANI sample acquired at different potentials in CO_2-saturated electrolyte are shown in Figure 19, which includes experimental data and curves calculated exploiting the equivalent circuit reported in the inset.

Each component of the total resistance can be separated performing EIS measurements and fitting the obtained data with a proper model[112]. In detail, the information regarding the *Resistance Charge Transfer* (RCT, the resistance associated to the electrocatalytic process) was evaluated in this work and plotted in Figure 18b-f for all the PANI samples. The charge transfer resistances obtained in the N_2-purged and CO_2-saturated solutions for each catalyst are compared. Taking

into consideration that under N_2 atmosphere H_2O/H^+ are the only chemical specie able to be reduced, while under CO_2 atmosphere also the latter is a competitive substrate, the EB-PANI electrode shows a great difference between the RCT values in the two solutions for several potentials and much lower RCT values in the N_2 one, implying that H_2O reduction could be the dominant reduction, Figure 18b.

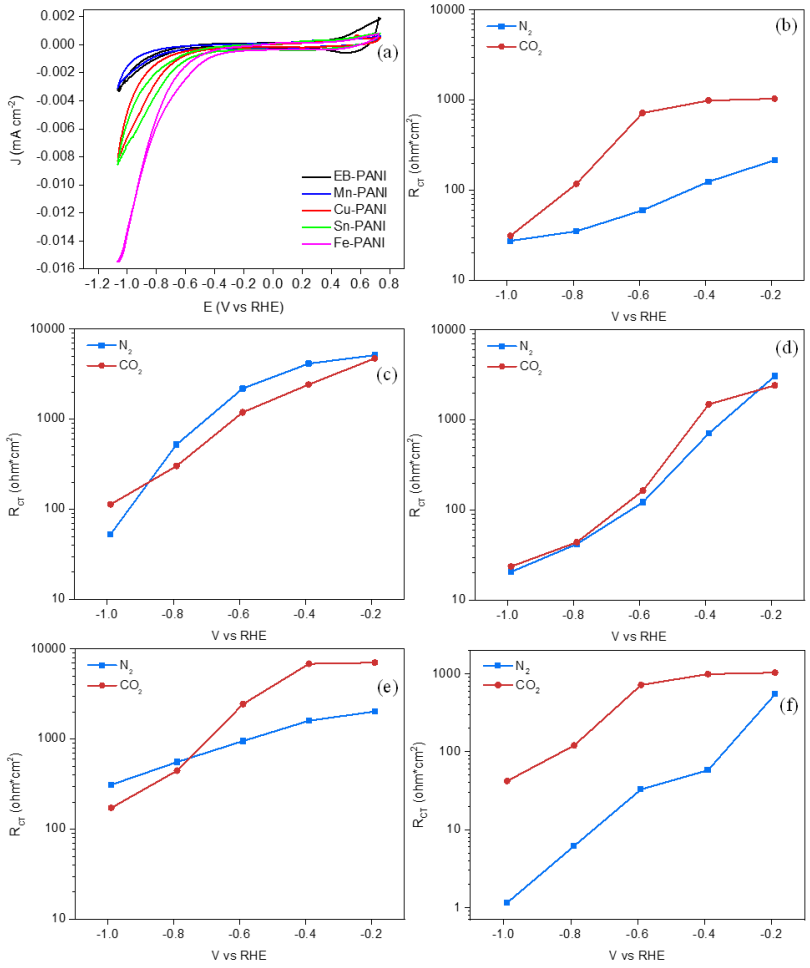

Figure 18: (a) Cyclic voltammograms of EB-PANI, Mn-PANI, Cu-PANI, Sn-PANI and Fe-PANI. Resistance Charge Transfer, RCT, in N_2-purged and CO_2-saturated electrolyte: (b) EB-PANI, (c) Mn-PANI, (d) Cu-PANI, (e) Sn-PANI and (f) Fe-PANI. Reproduced with permission from ref. 61. Copyright © 2021, Springer Nature.

Mn-PANI electrode performs completely differently from the EB-PANI and it displays a lower RCT value in CO_2 electrolyte at each potential (other than -0.99 V), indicating its possible selectivity for the CO_2RR Figure 18c. For Cu-PANI and Sn-PANI, Figure 18d-e, the difference of between RCT values in the two solutions is much smaller than that in the EB-PANI, indicating that they could be more

selective for the CO_2RR with respect to the latter. In contrast, Fe-PANI, Figure 18f, shows a significantly higher RCT value in CO_2 electrolyte with respect to that in the N_2 one, anticipating its scarce selectivity for the CO_2RR.

Combining the CV and EIS analyses, it is expected that doping PANI with Cu and Sn could manifest an interesting performance for the CO_2RR catalysis, while the Fe-PANI should display trace or even no activity toward it. The characteristics of Mn-PANI are not clear, even with the low amount of metal present in the sample, a drastic change regarding the RCT is present, making it interesting the evaluation of the practical performances of the catalyst.

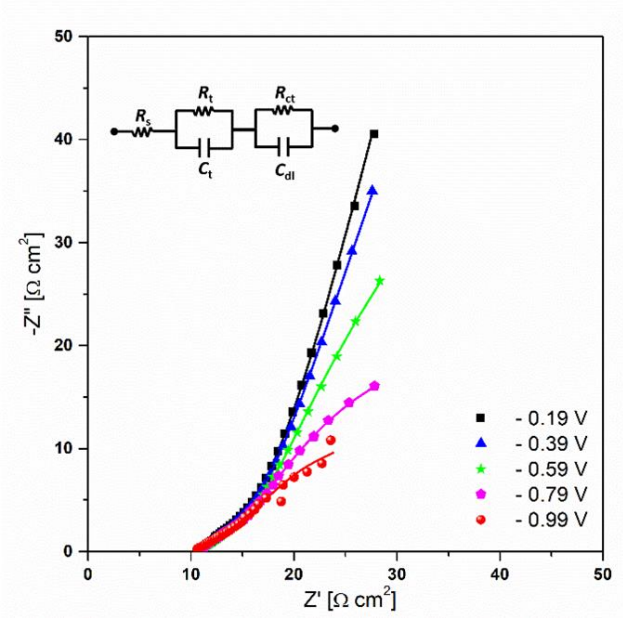

Figure 19: Nyquist plot of the impedance data acquired on Cu-PANI electrode in CO_2-saturated electrolyte at different potentials (the points are experimental data; the lines are calculated using the equivalent circuit shown in the inset). Reproduced with permission from ref. 61. Copyright © 2021, Springer Nature.

3.3.3 Double Layer Capacitance

In order to normalize the currents of the next chronoamperometries, not to the geometric areas rather than to the Electrochemically Active Surface Area (ECSA), the double double-layer capacitance (Cdl) was calculated for all the samples. The Cdl is indeed considered to be proportional to the ECSA in this way the intrinsic

activity of various materials is compared by investigating the Cdl-normalized current densities at the electrodes.

The detailed evaluation of Cdl for Cu-PANI is reported in Figure 20 as example, the calculated Cdl values are 3.6, 1.2, 4.3 and 2.0 mF cm^{-2} respectively for EB-PANI, Mn-PANI, Cu-PANI and Sn-PANI electrodes. The C_{dl} values of various electrodes (PANI, Cu-PANI, Mn-PANI and Sn-PANI) are evaluated by cyclic voltammetry at various scan rates in a potential range where no faradaic process occurs. The geometric current density is plotted against the scan rate and the slope of the linear fitting quantifies the C_{dl}.

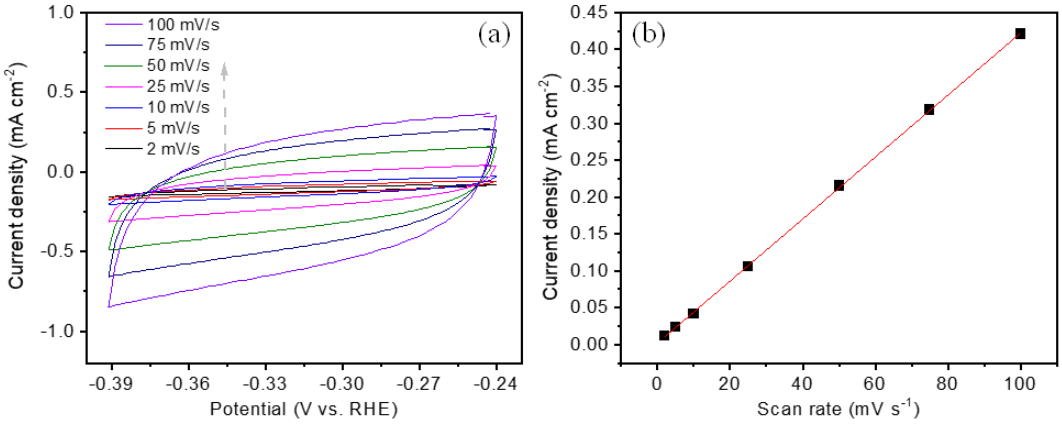

Figure 20: Determination of double-layer capacitance for various electrodes in N_2-purged 0.1 M KHCO3: (a) representing CVs on Cu-PANI electrode; (b) Capacitance values calculated from the slopes of current densities vs. scan rate. Reproduced with permission from ref. 61. Copyright © 2021, Springer Nature.

3.4 Investigation on the electrode composition

In order to evaluate the catalyst, a GDE was prepared drop casting the catalyst on a commercial GDL. A commonly underestimated crucial aspect in the CO_2RR is the composition of the electrode. Different from other research fields likes the one of fuel cells, in CO_2RR the electrode composition has not been intensively studied yet.

In the literature, several methods are reported for the electrode preparation[113], while a specific study on the composition and the roles of each component that overall clarify every aspect has not totally reached. The general composition of an

electrode is based on the current collector, the catalyst, an ionomer binder, whose guarantee the catalyst immobilization on the electrode and increases the ionic conductivity. In the CO_2RR literature is a common procedure the introduction of carbon blacks in order to better disperse the catalyst and homogenize the conductivity all over the electrode. Even more common procedure is the employment of Nafion solution as binder for the catalyst, especially when metal and metal oxide particles are used because of possibility to rapidly disperse them in water solution. With the aim to investigate the role of each component during the electrode fabrication, we performed a cross investigation preparing four different type of electrodes bearing the Cu-PANI as catalyst in presence of: a) no additives, b) carbon black, c) Nafion and d) carbon black together with Nafion. Those electrodes were tested under a bias of -0.99 V vs RHE and the reduced products coming from CO_2RR were analyzed, Figure 21.

Surprising, the Nafion addition dramatically pushes the hydrogen evolution reaction (HER) in terms of both selectivity and activity. Different case is the one of CO_2RR, in which seems not to interfere instead. Fluorinated groups of the ionomer are responsible of an increase in the hydrophobicity of the electrode, which is considered an aspect that would promote the selectivity toward the reduction of CO_2 rather than protons[114]. Nevertheless, the terminal chain sulfonic groups in Nafion lead to an increase in the overall surface polarity, which could act as a promoter of the competitive reaction of HER. The co-presence of Nafion and CB further enhances the HER activity, while CB alone does not add any significant beneficial effect for the CO_2RR (Figure 21b).

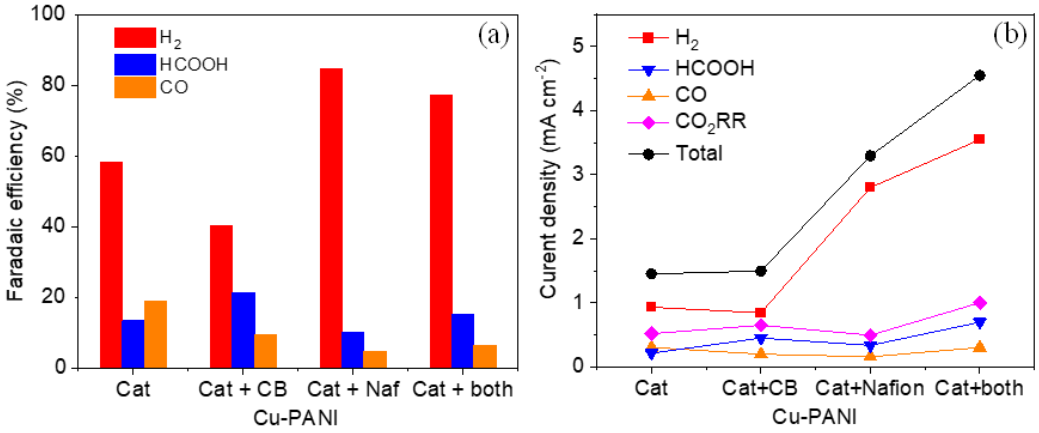

Figure 21: CO_2RR on various electrodes with different compositions at -0.99 V in CO_2-saturated 0.1 M $KHCO_3$ electrolyte: (a) Faradaic efficiencies and (b) partial current densities. Reproduced with permission from ref. 61. Copyright © 2021, Springer Nature.

Based on the above analysis, for the doped-polyaniline sample, we can conclude that the fabrication of electrode involving the presence of the Nafion ionomer should represent a non-profitable strategy. Such aspect would involve tremendous advantages in terms of cathode's electrode cost production, since the extremely high price of the fluorinated ionomers. PANI is an ionomer itself and can act as an ionic conductor, thus not requiring a proper material for that. It also shows great affinity for the GDL substrate without a binder, hence encouraging the PANI-based electrodes fabrication with the total exclusion of any additives.

3.5 Electrochemical performances

The catalytic properties of EB-, Mn-, Cu-, Sn-, and Fe-PANI as binder-free electrodes were investigated at -0.99 V vs the RHE.

Fe-PANI shows a FE_{H2} of 100% as perfectly predicted by EIS investigation. Detailed analysis is reported in Figure 22 for all the samples except for the Fe-PANI which was omitted. The EB-PANI shows a low selectivity only for HCOOH formation with a FE of 3.6% at -0.99 V (Figure 22a), evidencing how the organic polymer acts merely as support rather than a proper electrocatalyst for the CO_2RR.

While all Mn, Cu and Sn dopants lead to a significant enhancement in the CO_2RR selectivity, the individual selectivity for CO or HCOOH formation is distinct. The Mn-PANI achieves a FE_{CO} of 11.8% and a small FE_{HCOOH} of 1.1%. The Cu-PANI enhances both the CO and HCOOH formation, with FE_{CO} and FE_{HCOOH} values of 19.1% and 13.4%, respectively. The Sn-PANI is the catalyst showing the most significant increase in the FE_{HCOOH} (35.6%) and a modest FE_{CO} of 14.6%. Concisely, Mn-PANI is more selective for the CO and Sn-PANI is more selective for the HCOOH, while Cu-PANI produces CO and HCOOH almost equally. Figure 22b shows the electrode activity of various samples in terms of geometric current density.

It is easy to consider how the metal doping actually change and enhance the electrochemical activity toward the CO_2RR rather than the HER. The total current density on various electrodes follows the trend PANI ≈ Mn-PANI < Sn-PANI < Cu-PANI at -0.99 V. The PANI electrode shows almost no partial current density for CO formation, while the metal doping significantly improves the CO formation, with a highest value of 0.3 mA cm^{-2} at the Cu-PANI electrode. HCOOH formation

is remarkably enhanced on the Cu-PANI and Sn-PANI electrodes with respect to the PANI one. CO and HCOOH are the only detected CO_2RR products and the production rate of the C1 products (CO + HCOOH) displays the trend Sn-PANI > Cu-PANI > Mn-PANI > PANI. These results demonstrate that the Cu- and Sn-doping have successfully modified the properties of PANI toward the CO_2RR.

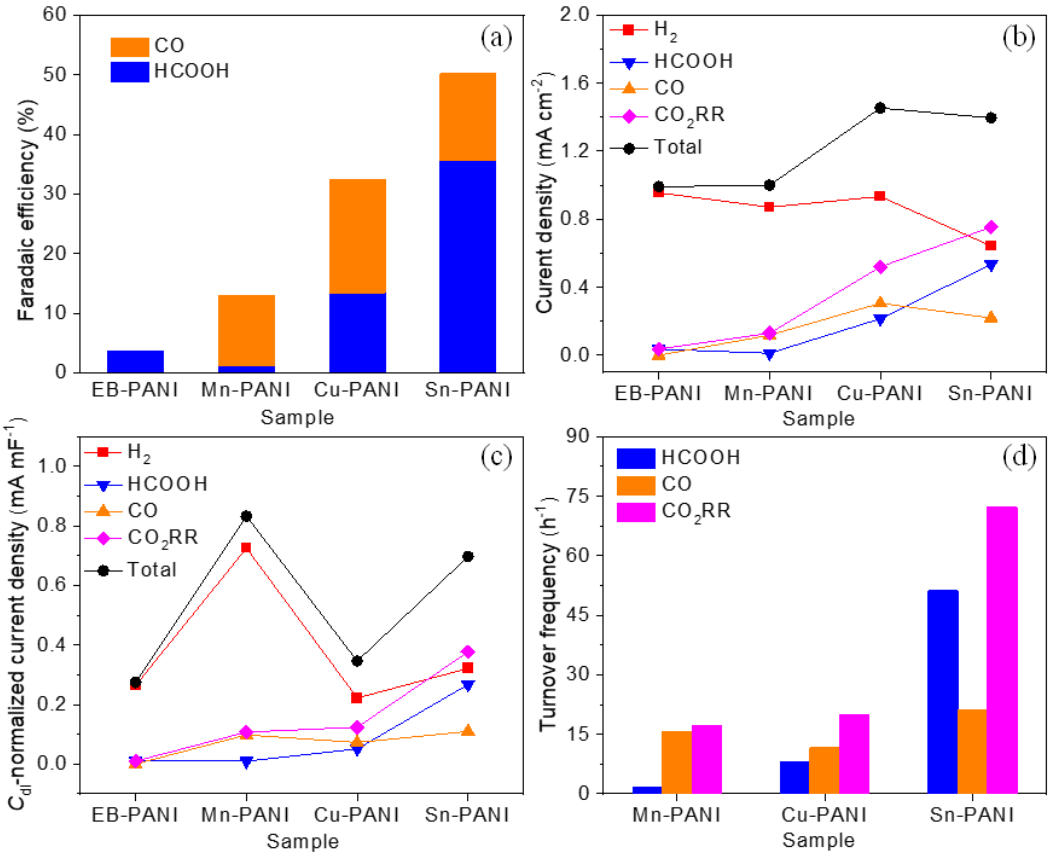

Figure 22: CO2RR on various electrodes in CO2-saturated 0.1 M KHCO3 electrolyte at -0.99 V: (a) Faradic efficiencies for CO2RR products, (b) partial current densities, (c) double-layer capacitance-normalized partial current densities and (d) turnover frequency for CO and HCOOH products.

The current normalized by the geometric surface area of the electrodes does not reflect the intrinsic activity of a catalyst, in order to do that, a normalization process has been done on the partial current intensities of each product. To evaluate the intrinsic activity of these materials, the current density is normalized by the electrochemically active surface area (ECSA) since it is considered to be proportionally associated to the double-layer capacitance (Cdl) which its plot is reported in Figure 22c. Doping the PANI with a metal cation leads to an increase in the activity of the materials for reduction reactions, including HER and CO_2RR.

It is observed that the Mn-PANI shows the highest activity and the Cu-PANI has the lowest activity among the metal-doped samples. However, most of the activity of the Mn-PANI is attributed to the HER, leading to a comparable activity for the CO_2RR with respect to the Cu-PANI, and even a lower activity compared to the Sn-PANI sample. While the activity for CO formation is comparable at the three doped catalysts, the HCOOH formation is much more favorable on the Sn-PANI than on the others. It is also worth to note that the HER activity becomes inferior to CO_2RR for Sn-PANI, which is probably correlated with the low activity of p-group metals for the HER. Figure 22d compares the CO and HCOOH formation rates normalized by the total metal atoms, that is turnover frequency (TOF, h^{-1}), at the three metal-doped PANI electrodes. It is evident that Sn-PANI outperforms the other counterparts with a higher atom efficiency for both CO and HCOOH formation. The TOF value is comparable with reported results for similar metal single-atom materials[115] and definitely higher than the bulk and nanostructured Sn-based catalysts[116], implying the good utilization efficiency of metal in the Sn-PANI complex.

The stability of Sn-PANI has further been investigated, over 10 hours CO_2 electrolysis at -0.99 V, as shown in Figure 23. The selectivity for CO and HCOOH formation (orange and blue square) remains almost stationary during the test, while the FE_{H2} firstly increases and then reaches a plateau (red square). Surprisingly, the electrode activity displays a continuous growth over the time. This could be attributed to the activation of the catalyst (green line, current density) or to the formation of metallic tin clusters, more conductive and able to perform the HER. Nevertheless, the selectivity for the CO_2RR products is not notably changed, it is supposed that the characteristic of the catalyst is not changed either. In situ characterization could be useful to understand the real nature of the active site under the bias.

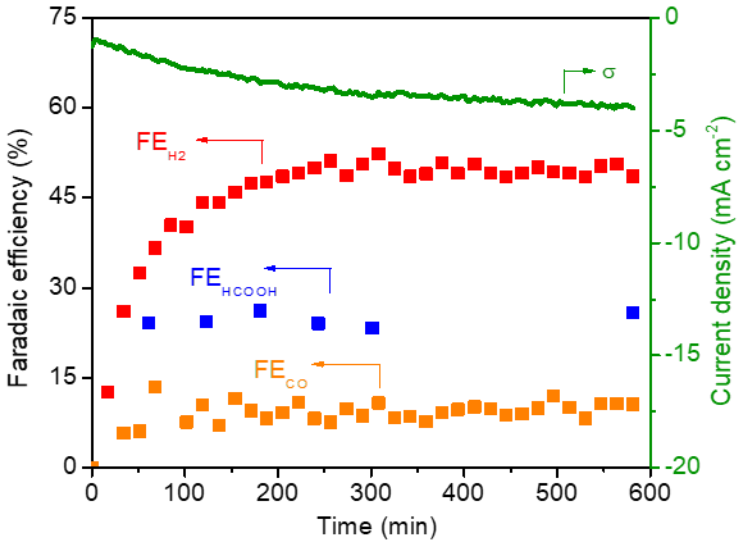

Figure 23: Long-term test of Sn-PANI electrode. Faradaic efficiency and total current density as function of time in aqueous CO2-saturated 0.1 M KHCO3 solution at -0.99 V.

In summary, such investigation lead to the fabrication of interesting material resulting be able to perform electrocatalysis of CO_2 without the assistance of any fluorinated additives. The strategy of doping resulted to be challenging and not versatile for every cation with the proposed synthesis, nevertheless the benefits of Lewis acids doping revealed to be an interesting approach to obtain single metal active sites, which drastically lower the amount of metal atom necessary for the catalysis. The metal cations of Mn, Cu, Sn and Fe have been investigated and show distinct characteristics, indicating the high tunability of the metal-PANI complexes. Sn-PANI outperforms other samples and obtains good selectivity, activity and durability for the CO_2RR, implying its good potential to be implemented in real devices.

Chapter 4

SnO_2/PANI

The preliminary investigation on doped polyaniline pushed forward the catalyst optimization based on this kind of substrates. Among all the employed metal center, the Sn-doped polyaniline resulted to be the most appealing regarding the CO_2RR thanks to its ability to produce formate with an interesting selectivity. The main recorded limitation of the catalyst was in its current densities; which reached values minor to 10 mA cm^{-2} all over the studied potentials.

In order to achieve more challenging results, different combination of electrolyte were investigated and a new one-pot synthetic procedure was build up. The renewed version of the Sn-PANI resulted a catalyst bearing a double amount of Sn cations on the polymer. Surprisingly, the tin atoms resulted organized in a different chemical environment, forming extremely low size SnO_2 nanoparticles of few crystal plane. The employment of the sonochemistry during the synthetic procedure, with its intense and locally peaks of temperature, was the source of the tin oxide deposition all over the polymer. Such catalyst outperformed the previous version, resulting able to reach formate selectivity at values higher than 70% and current density of the range of 50 mA cm^{-2}.

4.1 Synthetic procedure

All the reagents were purchased from commercial sources without further purification. N-phenyl-1,4-phenylenediamine (DANI, 98%), tin (IV) chloride (SnCl4.5H2O, 98%) ammoniumpersulfate (APS, $(NH_4)_2S_2O_8$, 98%), methanol (MeOH, 99.9%), N-methyl-2-pyrrolidinone (NMP, 99.5%), hydrochloric acid fuming (HCl, 37%) were all purchased from Merck.

The synthetic procedure is analogous at the one of the previous chapter, in which through a batch reaction the DANI dimers polymerize thanks to the addition of an oxidizing agent APS. The main differences are the employment of sonochemistry in the reaction batch and the presence of tin salt in the first reaction step. The sonochemistry introduction comes from the interest to induce further defects on the polymer and obtain lower size particles, while tin salt incorporation

aims to reach a higher rate of doping of the metal on the polymer. Surprisingly, the combination of acoustic wave and the presence of tin chloride causes the formation of SnO_2 nanoparticles on the polymer surface with an extremely low dimension of few atomic layers.

In this procedure 5.43 mmol of N-phenyl-1,4-phenylenediamine (DANI, 184.24 g mol^{-1}) and 1.5 times excess of $SnCl_4.5H_2O$ were dissolved in 15 mL of 70:30 v/v MeOH:H_2O with 1% w/w of HCl solution and kept under sonication for 10 minutes in a 10°C bath. Then 8.15 mmol of APS (228.18 g mol^{-1}) dissolved in 15 mL of the same solution, were added in the former dropwise along 5 minutes with continuous sonication. Once the two solutions are completely mixed, they were kept under sonication for further 3 hours in a cold bath, in order to prevent high temperature in the solution, and then stirred all along the night at room temperature (RT). The solution was then centrifuged and washed twice with milliQ water and a last time with MeOH resulting in a green powder typical of the ES-PANI.

The latter was then immersed in 10 mL of 32% ammonia solution and stirred for one night. The obtained EB-PANI blue-powder was then centrifuged and washed three times with water before placing in hoven overnight to dry. The resulting polymer was then used to load further tin cations inside the organic matrix thanks to the H^+ neutralization. Indeed, 4 mmol of EB-PANI (PM 93.13 g mol^{-1}) were dissolved with a 1.5 times excess of $SnCl_4.5H_2O$ in 20 mL of MeOH in a sealed vial. The solution was stirred at 60 °C for the night. The solution was precipitated adding 20 mL of water and then centrifuged. The powder was washed and centrifuged three times with water to remove any trace of metal salts. The obtained powder is labelled as SnO_2/PANI.

4.2 Physical and chemical characterizations

4.2.1 ATR

As in the previously chapter, the evaluation of polyaniline polymerization can be verified by ATR. In Figure 24a, the spectra of EB-PANI and SnO_2/PANI are reported and a coherent stretching pattern is reported. The correct polymerization of the polymer is verified by the presence of the stretching of the chemical groups involved in the polyaniline.

The C=N stretching of quinoid dimmine unit which falls at 1594 cm^{-1} and 1575 cm^{-1} respectively for EB- and SnO_2/PANI, evidencing a shift for the latter in presence of tin ions interacting with this chemical group. The C-C aromatic ring stretching of the benzenoid dimmine unit at 1497 cm^{-1}, present in both samples, the C-N stretching of aromatic amine registered at 1287 cm^{-1} and 1298 cm^{-1} for EB- and SnO_2/PANI, respectively, with a further shift induced by tin ions interaction. At 1167 cm^{-1} there is the stretching of quinoid ring and at 819 cm^{-1} the out of plane stretching due to hydrolysis immine units of the polymer[117]. The ATR spectra are then coherent with the previous published literature[118].

4.2.2 UV-Vis spectroscopy

In Figure 24b are reported the UV-Vis absorption spectra of the polyaniline samples dissolved in N-methyl-2-pyrrolidone.

The two samples show two main bands at 320 and 600 nm of the π-π* of the benzoid moiety and the n-p transition, typical of the semiconductive emeraldine polyanilines pattern[61,119,96]. For the SnO_2/PANI a moderate blue shift occurs in the region of the π-π* transition (from 322 to 315 nm) evidence of a partial doping of tin ions after the third synthesis step[96]. This information underlines how the presence of tin salt during the DANI polymerization do not dope the polymer, since in the EB-PANI polymerization without metal salt the maximum was obtained indeed at 322 nm, so the protons are dominant compared to tin ions. Nevertheless, the third step of reaction for tin doping, a lower amount of doping is registered, since in the previous sample the π-π* band was obtained a lower value of 305 nm. Such minor intense hypsochromic shift is presumably inhibited by the SnO_2 deposition induced by the acoustic wave. ATR and UV-Vis spectroscopies evidence anyway the presence of a minor amount of tin ions as dopants in the structure of the polyaniline, as previously reported in the literature[61].

4.2.3 FE-SEM

In Figure 24c, the images coming from Field Emission Scanning Electron Microscopy (FE-SEM) show the morphology of SnO_2/PANI sample.

The material does not show any trace of visible metal agglomerate in form of metal/oxide with the resolution of the employed technique, moreover it evidences

a drastic morphological change of the material in which the nano dimensional scale is reached with a homogenous distribution of the particles. This involves the sonochemistry helped with the nano-structuration of the material, drastically reducing its size.

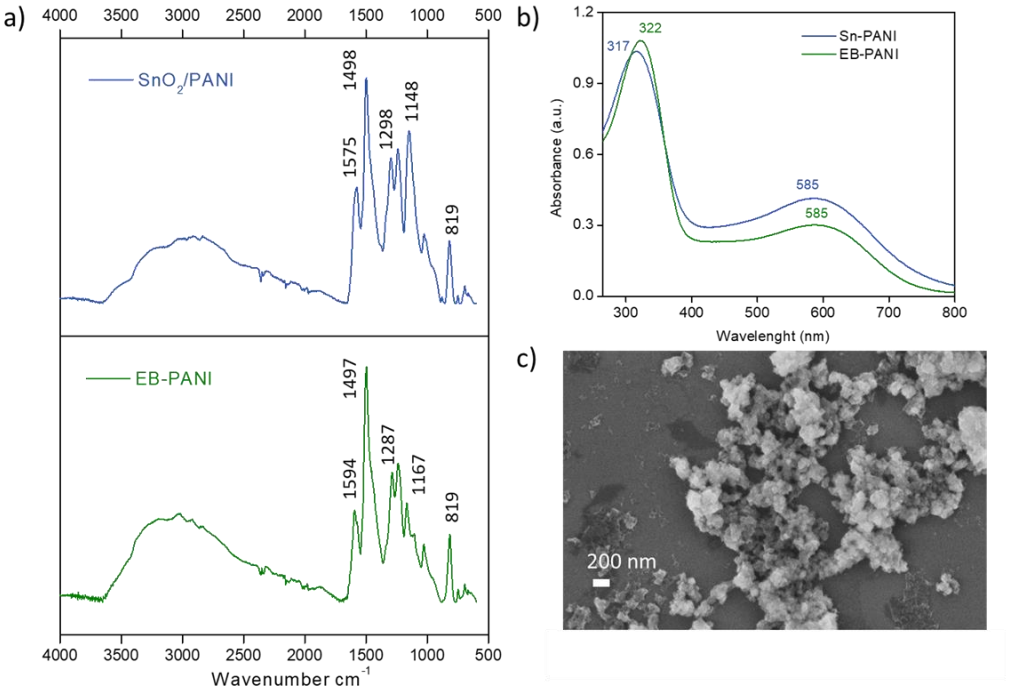

Figure 24: a) ATR spectra of SnO_2/PANI (blue) and EB-PANI (green, b) normalized UV-Vis spectra of PANI samples. c) FE-SEM image of SnO_2/PANI sample.

Further insight into the morphology and structure of the SnO_2/PANI sample is provided by EDX mapping through the FE-SEM characterization, Figure 25. EDX qualitatively confirms the composition of the catalyst, with a coherent distribution of C and N atoms, coming from the organic part of the polymer, and Sn and Cl atoms coming from the cation doping and counter ion. Unexpectedly, a homogeneous distribution of oxygen atoms are spread all over the catalyst, suggesting for the first time the presence of SnO_2 nanoparticles invisible by FE-SEM resolution. The tin oxide formation was an unpredicted result. Since with a similar method deprived of sonochemistry, the tin cations were able to be inserted inside the polymeric chain as mere dopants, thus not forming the relative oxide. Interestingly, EDX mapping shows also a homogenous displacement of chlorine atoms all over the nanoparticles, suggesting that part of the chloride atoms are integrated in the polymer matrix or externally to the metal oxide.

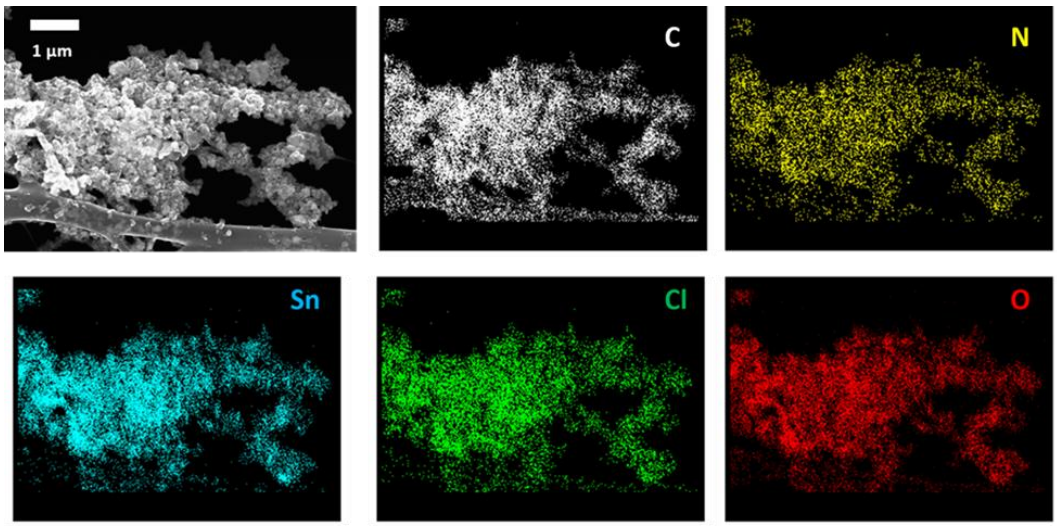

Figure 25: Electron diffraction image (top left) and EDX maps of C, N, Sn, Cl, O chemical elements for the SnO_2/PANI sample.

Through the EDX mapping, also an elemental analysis was possible to be determinated. In Table 3: Elemental analysis of SnO2/PANI sample performed by EDX technique and high-resolution XPS analysis. Sn/O and Sn/N ratio comparison. the atomic percentage of the N, Sn, O, Cl and C elements are reported together with the one obtained by high-resolution XPS technique. The EXD value were recorded on two different large size particles, in order to determinate a significant distribution of the values. The elemental analysis furnishes important clues about the nature of the tin cations inside the catalysts. Indeed, once known the atomic percentage of each atom and reconstructed the possible stoichiometry, different chemical species can be predicted or discarded. From the Table 3 is indeed possible to establish that the amount of chlorine atoms is deeply insufficient to determine the residual presence of the metal precursor $SnCl_4$. Thus chlorine atoms will be indeed determined to act as dopant inside the SnO_2 deposition of the PANI. Instead, the actual amount of oxygen present in the SnO_2/PANI sample is large enough to completely cover the amount of the tin cations following the stoichiometry of SnO_2. In which the ratio Sn/O is close to 0.5 due to the presence of oxygen involved in water and other carbon contamination due to air exposure. Also the Sn/N value suggests the presence of different types of tin cations compared to the one registered in the Sn-PANI catalyst exposed in the chapter 3.

Table 3: Elemental analysis of SnO_2/PANI sample performed by EDX technique and high-resolution XPS analysis. Sn/O and Sn/N ratio comparison.

SnO_2/PANI	N (%at)	Sn (%at)	O (%at)	Cl (%at)	C (%at)	Sn/O (%at/%at)	Sn/N (%at/%at)
EDX 1	9.6	4.8	18.0	3.7	64.0	0.3	0.5
EDX 2	7.3	8.7	21.4	6.8	55.8	0.4	1.2
XPS	8.0	6.0	16.5	4.0	65.5	0.4	0.8

4.2.4 XRD and TEM

A careful characterization of the morphology and structure of the SnO_2/PANI catalyst is obtained by combining XRD with electron microscopy techniques, as reported in Figure 26. In order to gain quantitative information from XRD data, Pawley refinement was employed, as shown in Figure 26a.

The XRD pattern clearly shows very broad peaks corresponding to the tetragonal unit cell (a = b = 4.761 Å, c = 3.198 Å) having the space group P42/mnm (# 136), all in accordance with the known crystalline structure of rutile SnO_2 (example Crystallography Open Database ID: 2101853, http://www.crystallography.net/cod/index.php). Due to the amorphous nature of EB-PANI, XRD pattern suggests the SnO_2/PANI catalyst is constituted by an amorphous polymeric matrix, decorated with nanometric (~ 1.5 nm in size, based on Pawley refinement) SnO_2-like structures. Further analysis was performed with the Transmission Electron Microscopy (TEM). The structural information from selected area electron diffraction (SAED, in Figure 26b) confirms the XRD results, showing contributions compatible with the rutile SnO_2 crystalline structure.

High-resolution TEM (HR-TEM) images (Figure 26c) provide useful details at the nanometric scale, it is indeed possible to directly visualize the amorphous polymer matrix homogeneously decorated with very small (size typically < 2 nm) crystalline domains. By measuring the interplanar spacing from HR-TEM images (Figure 26d) the rutile SnO_2 structure is confirmed.

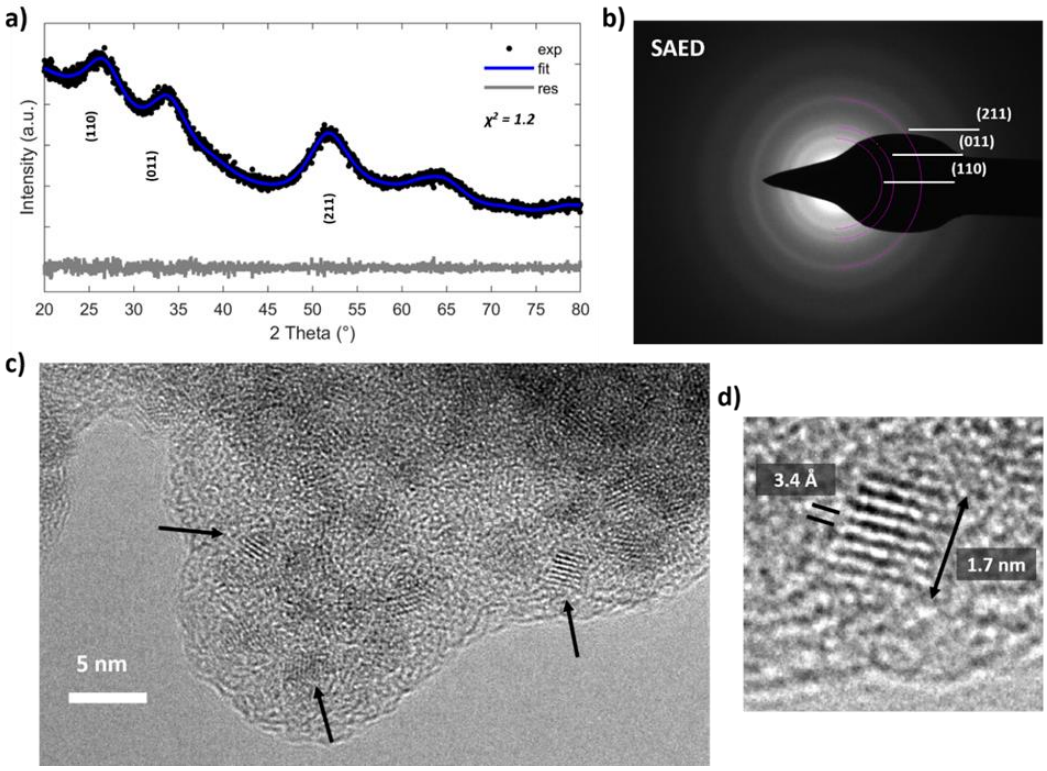

Figure 26:SnO_2/PANI morphological characterization. a) XRD experimental data, alongside fit through Paley refinement and corresponding residuals. b) selected-area electron diffraction results, c) and d) high-resolution TEM images. The arrows in c) point to the crystalline domains. The interplanar spacing measured in d), corresponds to the (110) family of planes in rutile SnO_2.

4.2.5 XPS

The low concentration of tin ions and their chemical state is confirmed and analysed XPS studies. In Figure 27 the high resolution XPS spectra of SnO_2/PANI sample are reported.

In Figure 27a, the C 1s signal is well fitted combining several contributions: the main band of the C=C (284.6 eV) and C-N (285.6 eV), coming from the polyaniline monomer[120] which also shows the correct ratio 4:2, the C-O-C (286.5 eV) and O-C=O (288.5 eV) respectively from the quinone and hydroquinone moiety coming from hydrolysis of immine group[121] and the pi-pi* (291.2 eV) coming from the benzenoid moiety[120]. In Figure 27b O 1s signal is fitted through the two contributions interacting with carbon atoms, the O-C-O (531.7 eV) and O-C=O (533.1 eV), and additionally a further signal attributable to O-Sn (530.8 eV) coming from the previously detected SnO_2[104]. In Figure 27c it is possible to identify the different types of polyanilines trough N1s analysis. The leucoemeraldine PANI has only benzenoid moiety, the emeraldine shows both benzenoid and quinonic

moieties, finally the pernigraniline PANI would shows further oxidized contributions[121]. SnO_2/PANI results to be an emeraldine base as expected also from UV-Vis, the theoretical stoichiometry value of 6:1 between C and N atom, excluding the carbon bonded to oxygen, is coherently preserved[121]. In Figure 27d the contributions of Sn 3d 3/2 and 5/2 are reported (487.5 and 495.9 eV). Interestingly, the values obtained for such peaks are slightly higher compared to the ones registered in classic SnO_2 samples[103,104,105].

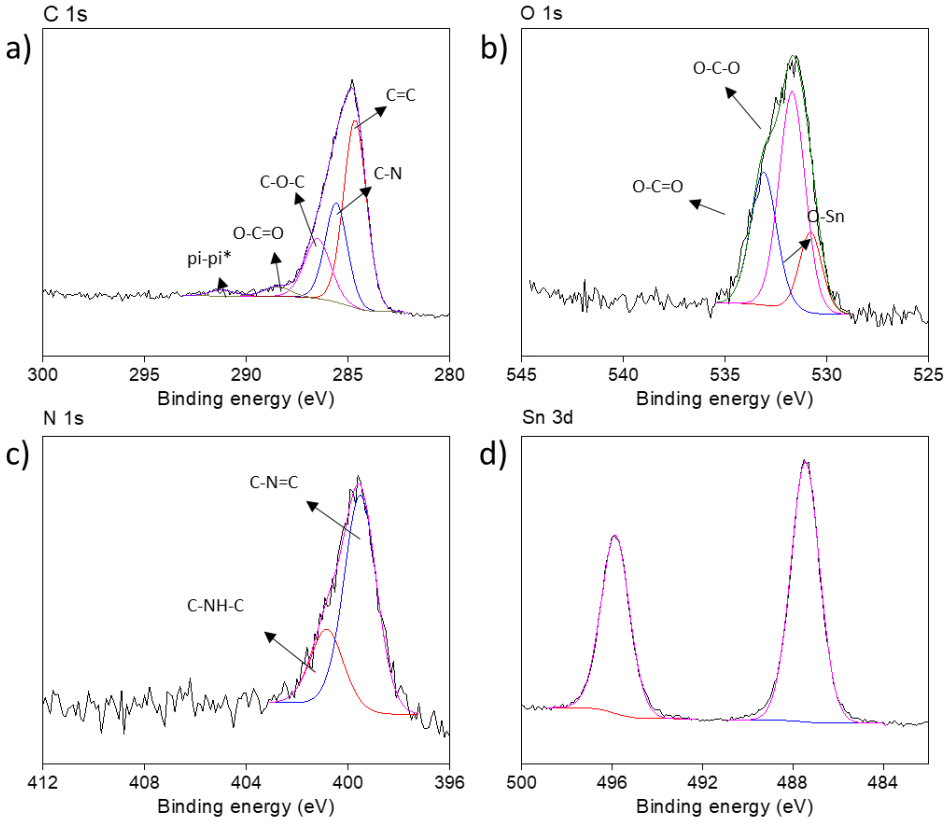

Figure 27: SnO_2/PANI high-resolution XPS spectra. In details a) C 1s, b) O 1s, c) N 1s and d) Sn 3d regions.

Due to extremely low size of these SnO_2 particles, the consequent defects and the perfectly homogeneous distribution of chlorine atoms from EDX, a different environment for tin cations result to be evident. We can affirm the SnO_2 nanoparticles are Cl-doped in order to compensate the dense defects present on the SnO_2 crystals thanks to the higher binding energies registered in presence of such electronegativity atoms[122,123].

4.3 Electrochemical performances

As reported in the previous chapter, the polyaniline is an ionomer, thus an ionic conductor, and it is also hydrophobic, which makes it stable on the GDE without any binder addiction. To the catalyst ink, Vulcan carbon nanoparticles were introduced together with the catalyst powder aiming to increase the overall electrical conductivity of the electrode. The catalyst and carbon nanoparticles followed the ratio of 9:1 for a total powder density of 1 mg cm^{-2} on each electrode.

SnO_2/PANI resulted to be mainly active for the $HCOO^-$ production just like the predecessor Sn-PANI. Several combinations of potentials and electrolytes were indeed studied in order to optimize the highest possible $HCOO^-$ selectivity, since H_2 and CO resulted to be produced only in lower amount. In Figure 28a the FE for three different compositions of electrolyte (0.5, 1.0 and 2.0 M of $KHCO_3$) and applied potentials (-1.0, -1.2 and -1.3 V vs RHE) are reported, parallel to their relative current densities registered in the same conditions, Figure 28b. The relationship between potential and CO_2RR suggests an operational applied potential close to -1.0 V[61]. Indeed, the differences among the potential chosen from -1.0 to -1.3 V reported in Figure 28a and Figure 28b are slight.

In the current work, the highest value of FE_{HCOO-} of 67.2% is obtained in 0.5 M $KHCO_3$ at -1.2 V, since we already know the EB-PANI itself is almost inactive for the CO_2 reduction, such selectivity is reached through the small amount of tin atoms present on the catalyst, which is only the 7.0% in weight quantified by ICP-MS. In Figure 28a, for each electrolyte, the selectivity for different potentials in each electrolyte are reported. At exclusion of the 0.5 M $KHCO_3$, all the other electrolytes do not show big changes in selectivity. Indeed, in the 0.5 M $KHCO_3$ electrolyte, there is a significant increase in selectivity of +30.4% switching from -1.0 V to -1.2 V. Our interpretation is that the highest selectivity for CO_2RR is theoretically reached at -1.0 V vs RHE, as the FEs at the same potential in 1.0 and 2.0 M $KHCO_3$ suggest, nevertheless the competition with HER in 0.5 M is too dominant, lowering the selectivity for CO_2RR. Generally for every electrolyte, shifting the potential from -1.0 V to -1.2 V causes an increase in current density which involves a major local hydroxyl anion production[124] as reported in equations 16 and 17:

$$CO_2 + H_2O + 2e^- \rightarrow HCOO^- + OH^- \qquad \text{Equation 16}$$

$2\ H_2O + 2e^- \rightarrow H_2 + 2\ OH^-$ Equation 17

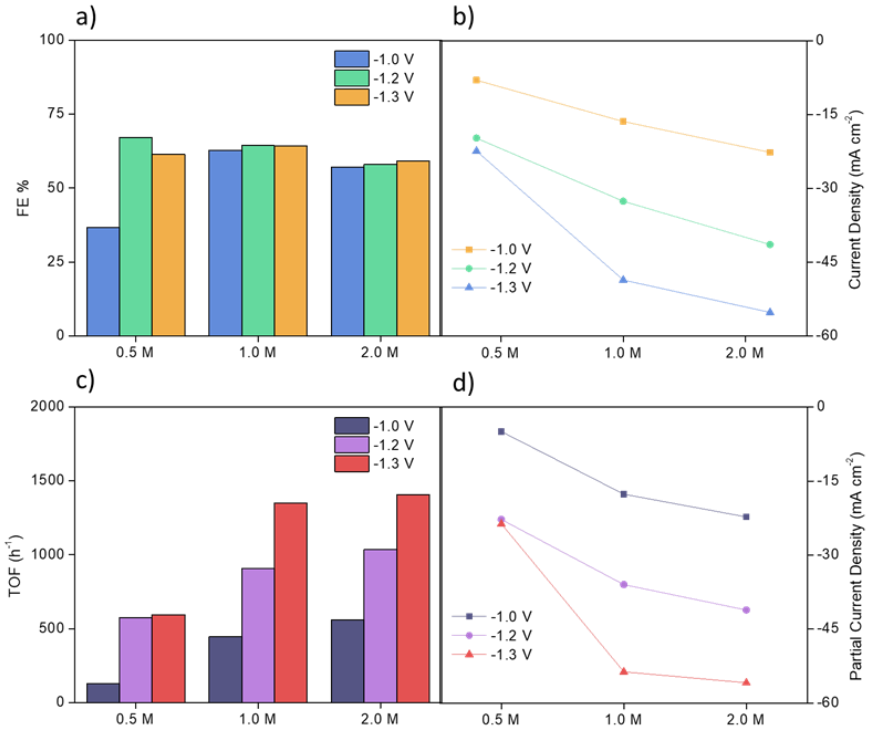

Figure 28: Chronoamperometries results in different combinations of electrolytes (0.5, 1.0 and 2.0 M of $KHCO_3$) and applied potentials (-1.0, -1.2 and -1.3 V vs RHE. a) faradic efficiencies, b) current densities, c) turnover frequencies and d) partial current densities for formate.

The increase in the local pH near the electrode helps the CO_2RR because the HER is decreased by protons depletion. This phenomenon affects all the electrolyte pushing the potential from -1.0 to -1.2 V, nevertheless only in the 0.5 M $KHCO_3$ is so intense. We can find the understand the reason of this behavior taking in consideration the current density plot of Figure 28b. Indeed, in the 0.5 M $KHCO_3$ the selectivity rises from 36.7% to 67.1% with a significant current density variation from 8.0 mA cm^{-2} to 19.8 mA cm^{-2}. Pushing the applied potential to -1.3 V in the 0.5 M $KHCO_3$ solution does not involve important variation in current density, which is translated in a similar selectivity.

For more concentrated electrolytes (1.0 and 2.0 M $KHCO_3$) a comparable increase in selectivity from -1.0 V to -1.2 V is not recorded. That occurs because in these two electrolytes at -1.0 V is already reached a high current density of -16.4 mA cm^{-2} and -22.7 mA cm^{-2}, comparable to the one registered in 0.5 M at more negative potential. The increase in the current densities related to the salt

concentration is a phenomenon coming from a better conductivity of the system. There is actually a limit on protons depletion due to the hydroxyl anion production, since is known that in flow cell reactor at high current density, the concentration of OH^- anions is so high to actually react with the gaseous CO_2, lowering the available amount of CO_2 for the electrolysis. These data suggest the complexity of the selectivity in the CO_2RR, since the current density indirectly influences also the CO_2RR catalysis[32]. The current density is mainly determined by the electrochemical setup, so different cell configurations would inevitably show different results even with the same catalyst. Considering the relative turnover frequencies (TOF), calculated considering the overall number of tin atoms in the catalyst, and the partial current densities for formate (respectively, Figure 28c and d), we can assume the best operational conditions for the CO_2RR electrolysis are certainly in 1.0 M $KHCO_3$ electrolyte, in which the TOF number is almost comparable with the one obtained in the more concentrated 2.0 M.

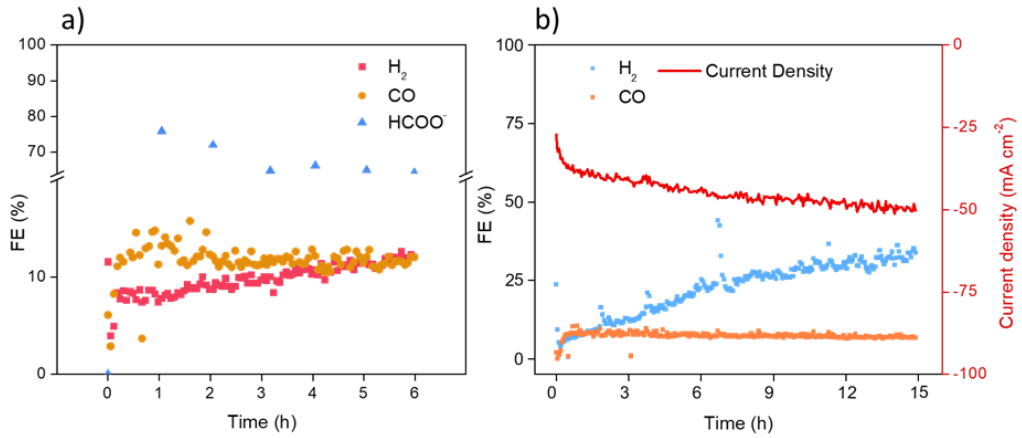

Figure 29: Chronoamperometry tests for stability evaluation. a) $HCOO^-$ production during time at -1.2 V vs RHE in 1.0 M $KHCO_3$, b) current density, FE_{H2} and FE_{CO} along 15 hours at -1.2 V in 2.0 M $KHCO_3$.

A detailed stability test gives further information about how the selectivity changes in function of the amount of formate produced, Figure 29a. A test performed at -1.2 V in 1.0 M $KHCO_3$ shows a decreasing trend all along the 6 hours of test for the $HCOO^-$ selectivity. After one hour of the test the total FE_{HCOO^-} reaches the highest value of 75.9%, and this data inevitably decreases hourly until the last point on the sixth hour of 64.3%. Due to the nature of the setup, the electrolyte is mechanically recirculating through a peristaltic pump during the test. All along the experiment, $HCOO^-$ concentration is increasing, likewise the hydrogen evolution

and the overall current density. The formate is able to be preserved inside the electrolyte without being re-oxidized in the anode compartment thanks to the CEM employed in the experiment. In order to confirm such trend, an all-nightlong experiment was performed at -1.2 V in 2.0 M $KHCO_3$. As evidenced in Figure 29b, the current density increases again parallels to the hydrogen evolution. Comparing to the 6 hours test in 1.0 M $KHCO_3$ and the previously published work in 0.1 M $KHCO_3$[61] together with this last test of 16 hours, it seems that the increasing hydrogen evolution and lowering of formate production is promoted working in more concentrated electrolytes. This information confirms the 1.0 M $KHCO_3$ as the best electrolyte for operating conditions.

Chapter 5

Zeolitic Imidazole Framework

The common characteristic among all the materials investigated as possible catalysts for the CO_2RR is the research of a strategy able to create single metal active sites. For this purpose, the class of the Molecular Organic Framework (MOF) is a perfect candidate, since each metal cation in the structure is stabilized by organic ligands with a reciprocal electron density sharing. Generally, the MOFs are retained materials suffering of poor stability in presence of water, a critical drawback for the application of interest, in which the catalyst is facing a water based electrolyte. Nevertheless, there is a peculiar subclass of MOFs which resemble the typical geometry of the zeolite, the Zeolitic Imidazole Framework (ZIF), that are perfectly stable once exposed to water. Among all the known ZIFs, one of the most studied is the ZIF-8, this compound bear zinc cations as metal centres, shows highly exposed internal surface and are employed in the gas separation/sequestration technologies.

The ZIF-8 was preliminary studied as a zinc based catalyst for the possible CO_2RR catalysis. The investigation also continued in order to engineer the material, which resulted highly dispersible in water solution, with the consequent detachment of the powder from the current collector during the electrolysis and gas evolution. In order to prevent the problem and additionally to increase the conductivity of the catalyst, an innovative procedure englobing the Multi Walled Carbon Nanotubes (MWCNT) was adopted, synthetizing a composite material in which the ZIF-8 was able to grow on the MWCNT, eventually englobing them.

5.1 ZIF-8 synthesis

As anticipated, the ZIF-8 synthesis led to the formation of a material showing interesting activity towards the CO_2RR, nevertheless its catalytic activity was decreased due to the high affinity of the catalyst with the water electrolyte. Indeed, ZIF-8 powder is easily dispersible in water solution, which makes problematic to work with a drop-casted electrode in such condition. As an optimization strategy, a more hydrophobic environment should be built around the catalyst, in order to decrease its affinity with the polar environment of the water electrolyte. Taking in

consideration this aspect and the mutual interest on developing a more conductive heterogeneous catalyst, the MWCNT were integrated in the catalyst.

All the reagents were purchased from commercial sources and employed without performing further purification. Two different catalysts were synthetized, the ZIF-8 without the presence of MWCNT, denoted as *sZIF-8*, and the one bearing the MWCNT inside, denoted as *sZIF-8-MWCNT*, both using a new procedure in water solution[125]. The *s*- present in both names stand for the employment of acoustic waves during the synthesis in order to highly disperse the particles. The sZIF-8 synthesis, 1.1 g of 2-methylimidazole (Im, 13.4 mmol) and 591 mg of sodium hydroxide (NaOH, 14.8 mmol) were dissolved in 30 mL of bidistilled water; such basic pH involves the complete deprotonation of the Im molecule in their relative imidazolates (Im^-). In other separated 30 mL of bidistilled water, 500 mg of [$Zn(NO_3)_2 \cdot 6H_2O$] (1.68 mmol, Zn:MIm ratio 1:8) were dissolved. The latter solution was then added dropwise to the former under continuous sonication, which was kept cold by placing ice cubes in the sonication bath. Immediately after the first drop, the limpid basic solution turned into a white colloidal suspension due to the precipitation of Zn cations with Im^- counterions. Once the two solutions were completely mixed, the sonication was kept for five minutes longer, in order to further disperse the catalyst. The powder was then separated by centrifugation, it was washed twice with water and a third time with ethanol to remove the excess of Im/Im- and hydroxide. The final sample was eventually collected and dried under vacuum until constant weight was reached. Only small aliquots of solvent were employed for the purification, due to the high level of dispersion of ZIF-8 in polar solvent like water. The sZIF-8-MWCNT was prepared using a similar procedure but adding MWCNTs (50mg, 5% w/w) in the former basic solution and sonicating for at least 30 minutes before the addition of the sequent solution bearing the zinc salt. Sonication was performed in a cold bath which prevents the agglomeration of MWCNTs during the dispersion step. The colloidal formation after the first drops of zinc solution, was not clearly visible in this case of the sZIF-8-MWCNT, due to the dark colour of the carbon source. At half of the salt solution addition, the precipitation of MWCNTs together with ZIF became clearly visible. In addition, as a reference material for the electrochemical comparison, a sample of bare MWCNTs was sonicated in the same basic media with the imidazolate, washed and dried for comparison.

5.2 Physical and chemical characterization

5.2.1 ATR spectroscopy

The two samples sZIF-8 and sZIF-8-MWCNT were analyzed by infrared spectroscopy in order to characterize the correct precipitation of the zeolitic framework. The ATR spectra reported in Figure 30 shows a symmetric pattern for both materials, thus demonstrating the formation of the ZIF also in presence of the MWCNT. In details, the peaks at 3130 and 2923 cm^{-1} are caused by the C-H stretching of the aromatic carbons, the signals at 1669 cm^{-1} and 1590 cm^{-1} are respectively the C=C and C=N stretching modes of the imidazole. The three peaks at 1456, 1415 and 1306 cm^{-1} are the stretching of the entire ring and the 1146 cm^{-1} is the C-N stretching mode. The 993 and 749 cm^{-1} can be assigned to the C-N and C-H bending modes. The 693 cm^{-1} is the ring-out-plane of the imidazole and the final 645 cm^{-1} of the interaction between Zn^{2+} cations with imidazolates, confirming the correct formation of the framework. ATR investigation additionally underlines further information by the absence of signals at 3393 cm^{-1} and 3218 cm^{-1}, which is translated in the missing involvement of Zn^{2+} cations in inorganic species likes the ZnO and $Zn(OH)_2$ in the range of sensibility of the technique[126].

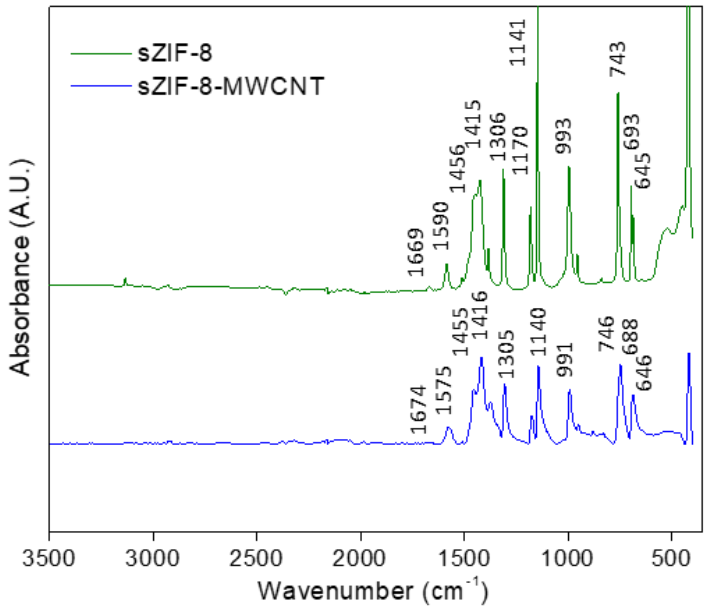

Figure 30: ATR spectroscopy of sZIF-8 sample (green line) and sZIF-8-MWCNT sample (blue line). Reproduced with permission from ref. 125. Copyright © 2022, Elsevier Ltd.

5.2.2 XRD

XRD analyses were performed on both the samples. As reported in Figure 31a, the XRD patterns of sZIF-8 and sZIF-8-MWCNT were recorded and compared with the VESTA simulated diffraction pattern of a centered cubic structure having a $\bar{4}3m$ simmetry[127] and with several experimental ones from different publications[128,129,130].

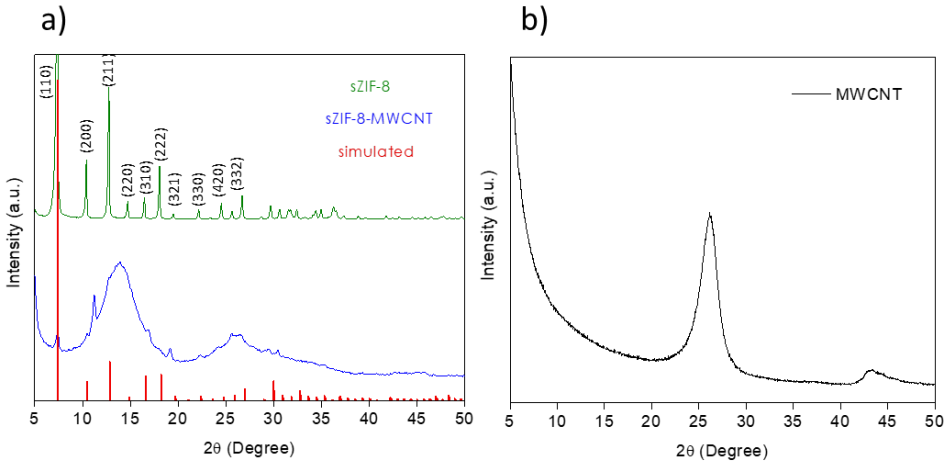

Figure 31: XRD patterns of a) sZIF-8 (green line), sZIF-8-MWCNT (blue line) and related ZIF-8 simulated pattern from VESTA software (red line) and b) MWCNT after basic treatment. Reproduced with permission from ref. 125. Copyright © 2022, Elsevier Ltd.

For sZIF-8 (green line), the diffraction peaks correspond to the ZIF-8 crystals planes of both simulated (red line) and the ones reported in the literatures, indicating the successful synthesis of highly crystalline ZIF-8. On the contrary, sZIF-8-MWCNT (blue line) shows a different pattern in which the well-defined peaks are partially covered by two broad bands at 13.97° and 26.13° with a minor contribution at around 45°. The bands with a maximum at 26.13° and 45°, respectively, are clearly associable with the main bands of MWCNT subject to the same treatment without zinc salt (Figure 31b), while the band with a maximum at 13.97° is the typical band reported in literature for amorphized ZIF-8[131,132,133]. Nevertheless, minor crystalline peaks are still present, meaning that the prepared ZIF-8 is not completely amorphous but rather a mixture of crystalline and amorphous regions. The drastic decrease in crystallinity is clearly due to the presence of nanotubes and a presumable π-π interaction of carbon nanotubes with the imidazoles which inhibit the crystal growth during the synthesis[134]. Due to nature of the application, the loss of the crystallinity and the consequent porous area is not as criticality such as it could be in gas separation/sequestration technology, since only the external sites

are electrochemical active toward the possible reaction, thus hiding the inside sites. Moreover, a lower crystallinity could induce greater defects a larger number of active sites. However, this aspect has not been investigated.

5.2.3 TGA-EGA analysis

The thermal degradation was performed on both samples in order to define the same degradation pathway, thus defining the coherent presence of a zeolitic imidazole species for sZIF-8-MWCNT and excluding different inorganic form of zinc.

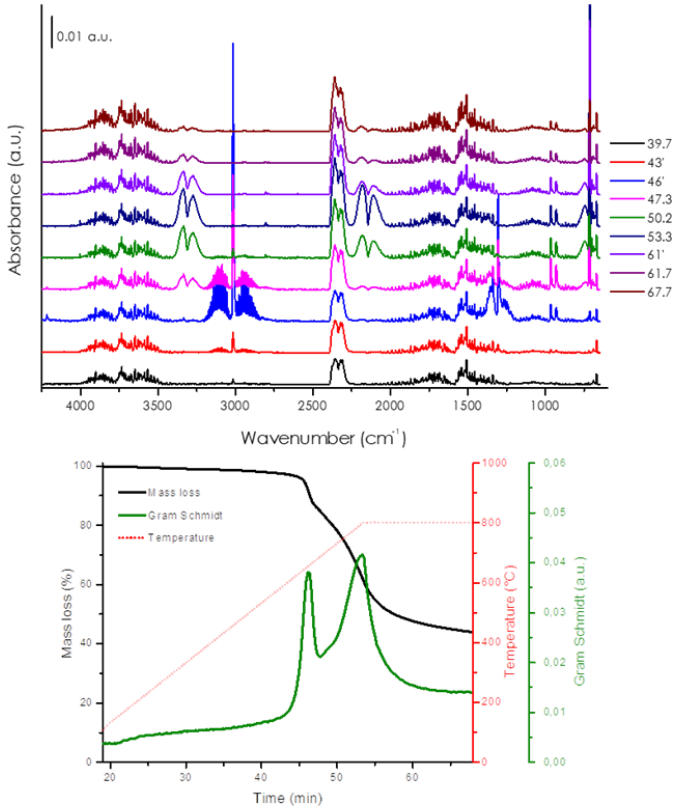

Figure 32: TGA and EGA for sZIF-8. Reproduced with permission from ref. 125. Copyright © 2022, Elsevier Ltd.

The degradation of sZIF-8 occurs in two main steps (Figure 32) which correspond to the two peaks of Gram-Schmidt curve, after 600°C. During the first

degradation step, main degradation products are methane (peak at 3014 cm^{-1}), CO_2 (band at 2340 cm^{-1}), ammonia (peaks at 965 cm^{-1} and 930 cm^{-1}) and water (bands centered at 3780 cm^{-1} and 1595 cm^{-1}). After 680°C, two signals at 3336 cm^{-1} and 3274 cm^{-1} increase in the intensity, indicating increasing amount of HCN vapor, while the signals related to methane become less intense. During the second degradation step at 800°C, degradation products are HCN, CO_2, water, ammonia and CO (bands centered at 2142 cm^{-1}). During the isothermal steps at 800°C, the products degradation composition remains unchanged but the overall spectra intensity decreases. Residual weight of sZIF-8 at 800°C is 44%.

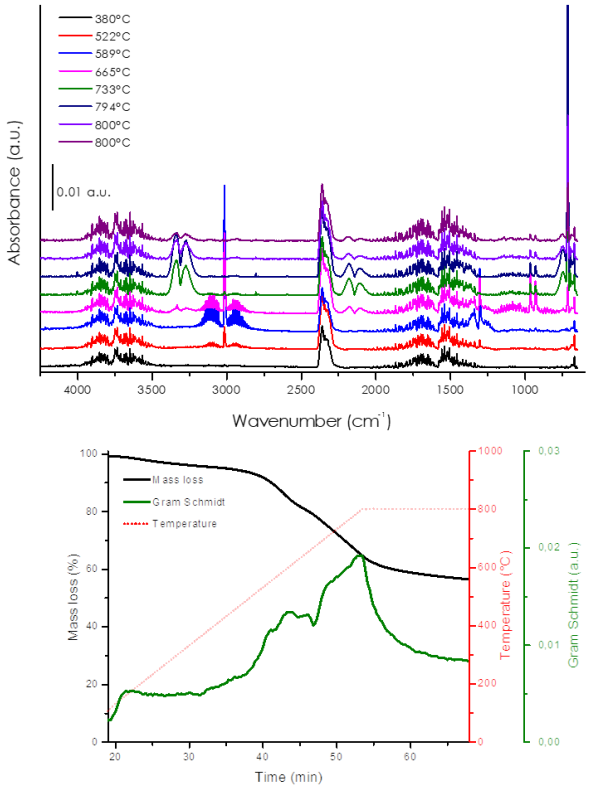

Figure 33: TGA and EGA of sZIF-8-MWCNT. Reproduced with permission from ref. 125. Copyright © 2022, Elsevier Ltd.

The degradation of sZIF-8-MWCNT is less defined but still two main steps can be identified at 600°C and 800°C. The degradation products and their evolution appear to be the same as those of sZIF-8 and the residual weight at 800°C is 57%. The MWCNT presence seems to have no relevant effect on the thermal degradation of sZIF-8. The coherence in the thermal degradation of the samples confirm the presence of a ZIF species also in the composite material.

5.2.4 FE-SEM

A morphological investigation was performed on both materials with the electron microscopy revealing large differences between sZIF-8 and sZIF-8-MWCNT samples. Indeed, sZIF-8 shows the typical rhombic dodecahedron morphology of micrometrical particles[135,136,137,138] (Figure 34a). The incorporation of MWCNTs leads to drastic changes in both the size and morphology of the particles (Figure 34b). During the precipitation and agglomeration of ZIF-8, the MWCNTs were incorporated in the matrix. The dimension of the particles gets lower reaching the nanoscale dimension and the typical rhombic dodecahedron shape is totally lost eventually causing the material amorphization. Such information perfectly matched with the less defined TGA degradation step and with the loss of crystallinity on XRD pattern.

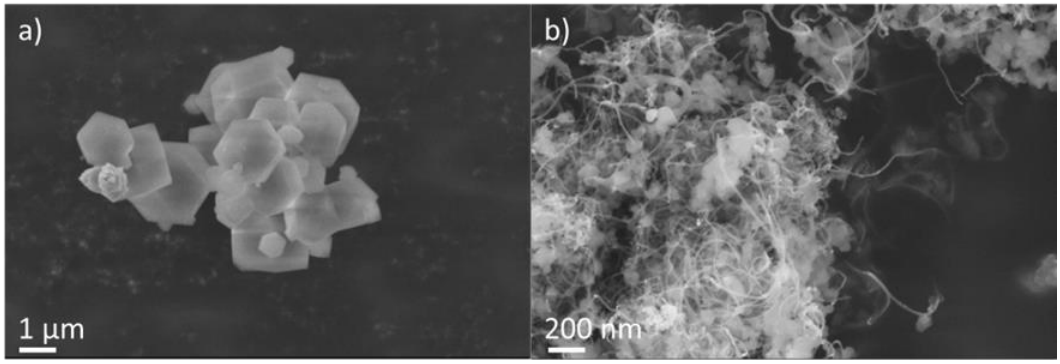

Figure 34: Electron microscopic images. a) FE-SEM images of sZIF-8 and b) sZIF-8-MWCNT. Reproduced with permission from ref. 125. Copyright © 2022, Elsevier Ltd.

5.2.5 BET analysis

Because of the amorphization, the materials also differ for their porosity (Figure 35a and b). sZIF-8 shows a high BET surface area and a large pore volume mainly attributed to micropores, which is typical of well-structured ZIF-8[139]. sZIF-8-MWCNT displays a relatively lower BET surface area and pore volume, to which meso- and macropores are the major contributors, confirming the significant influence of MWCNTs incorporation on the ZIF growth. The detailed obtained values are reported in the comparative Table 4 in which the two samples are summarized.

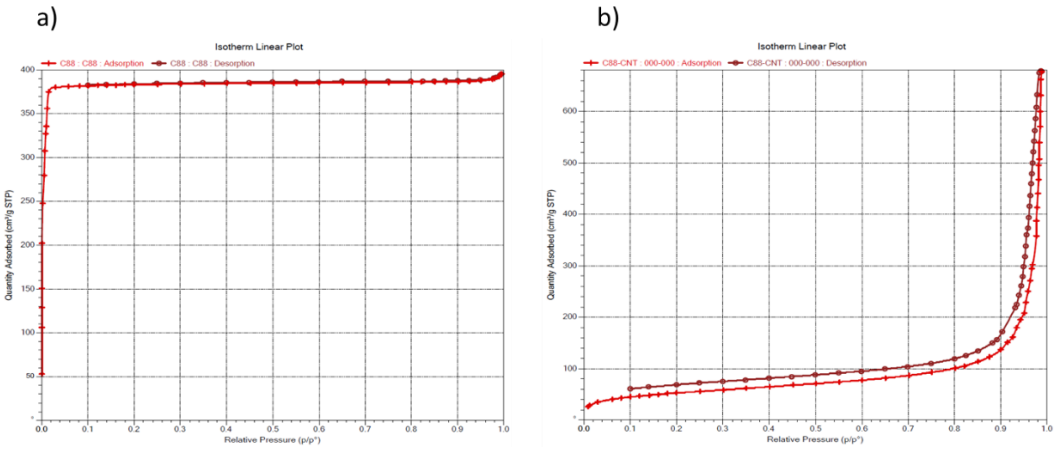

Figure 35: Isothermal linear plot of a) sZIF-8 and b) sZIF-8-MWCNT. Reproduced with permission from ref. 125. Copyright © 2022, Elsevier Ltd.

Table 4: BET surface area and pore volumes of sZIF-8 and sZIF-8-MWCNT. Reproduced with permission from ref. 125. Copyright © 2022, Elsevier Ltd.

Sample	S_{BET}	S_{MICRO}	V_{MICRO}	$S_{(1.7\text{-}300)}$	$V_{(1.7\text{-}300)}$
	($m^2\ g^{-1}$)	($m^2\ g^{-1}$)	($cm^3\ g^{-1}$)	($m^2\ g^{-1}$)	($cm^3\ g^{-1}$)
sZIF-8	1215	1189	0.58	17	0.02
sZIF-8-MWCNT	187	17	0.007	142	1.0

5.2.6 XPS

A detailed X-ray Photoelectron Spectroscopy (XPS) investigation provides several information about the chemical composition of the ligand and of the zinc center for both the sZIF-8 (Figure 36) and sZIF-8-MWCNT catalysts (Figure 37). All the values reported were calibrated with the C1s adventitious carbon placing it at 284.8 eV binding energy. The first parameter to consider is the N1s signals coming from the imidazolate ligand. As we can see from the N 1s plot of sZIF-8 sample (Figure 36 top-left) the nitrogen signal is deconvoluted in two main contributions: the C=N-C (399.1 eV) coming from the degenerate N^- of the

imidazolate ligand Im^- and the C-NH-C (400.2 eV) of undercoordinated imidazole Im which restores the amino group[121]. It is important to underline that, both for the Im^- and Im molecules, the aromatic resonance present on the ring makes the nitrogens equivalent between them; thus the only difference present would be between the nitrogens sharing the negative charge in the ring (Im^-) and the one completely uncharged (Im). The presence of both the nitrogen coming from the Im^- and Im, suggests that there are undercoordinated imidazoles defects on the crystals surface, coherent with their known thermodynamical stability by theoretical investigation[140]. In the C 1s spectrum of sZIF-8 (Figure 36 top-right) several contributions are necessary to fit the imidazole ligand. In details, the C-C (285.6 eV), C-N (286.4 eV) and π-π* (292.2 eV), additionally there is the adventitious carbon, C adv. (284.8 eV), and its oxidized form, C-O-C (287.9 eV). In the region of Zn 2p of sZIF-8 (Figure 36 bottom-left) the typical doublet of Zn is recorded. The $2p_{3/2}$ signal requires two functions to be deconvoluted, the main Zn-N (1022.5 eV)[141] from the Zn coordinating the imidazolate ligand and a generic Zn-OH (1021.6 eV) coming from undercoordinated Zn^{2+} sites which reacts to water in order to balance the charge[126,142]. The water is actually coordinated as H_2O molecule and OH^- ligands in order to balance the stoichiometry charge between the Zn^{2+} and the Im^-. The presence of these minority defects are important, indeed they define the presence of a inorganic active species which can interact both with the CO_2 and H^+ in order to promote an electrochemical reaction. The binding energy of the Zn-OH species is difficult to interpret, indeed the discrimination between the bonds between Zn-O from ZnO and the Zn-OH from $Zn(OH)_2$ it cannot be interpreted by mere Zn investigation[143]. Moreover, in this scenario our supposition is to have only zinc center coordinating on hydroxyl/water ligand together with three imidazolate, not properly an inorganic form of $ZnO/Zn(OH)_2$, since from TGA, ATR there are no evidence of such species. In order to better clarify this aspect, it became fundamental the O 1s spectra analysis. Indeed, if the Zn signals does not discriminate the $ZnO/Zn(OH)_2$, the O 1s such energy gap became important. As we can see from Figure 36 bottom-right, the oxygen signal can be convoluted with two function, one coming from the adventitious carbon oxidized (532.8 eV) already identified by the C1s spectra and an additional OH-Zn peak at (531.5 eV)[143].

Same investigation is performed for the sZIF-8-MWCNT in Figure 37. Looking to each regions, the differences are quite small between the two samples. In the N 1s spectra of the sZIF-8-MWCNT, the ratio between the N-C and N-H is indeed is lower compared to the sZIF-8. This evidences how the former is a more defected material exposing more undercoordinated imidazolate, as confirmed also by the FE-SEM images Figure 34. Analyzing the C 1s region, the presence of a minor amount of adventitious carbon evidence the presence of a minor porous volume of the material which reflects its minor capacity to adsorb molecules inside it pores. Also the C-C signal is of higher intensity, due by the presence of MWCNT inside the material.

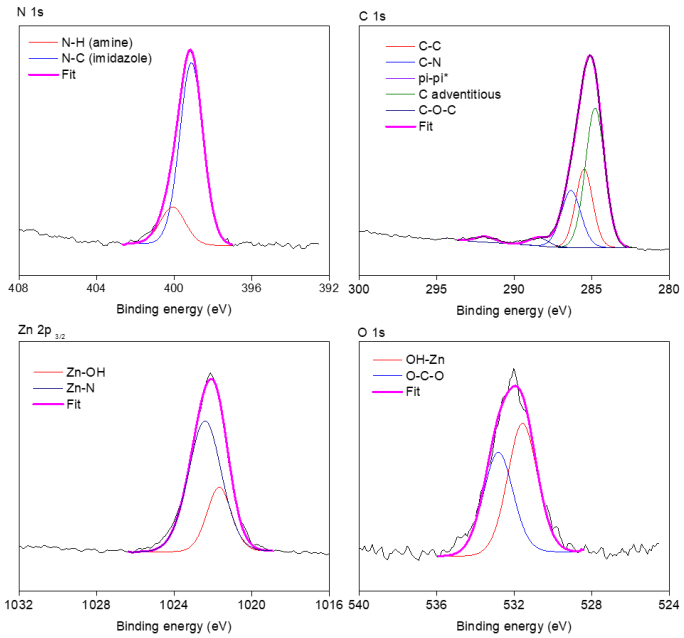

Figure 36: N1s, C 1s, Zn $2p_{3/2}$, O 1s region of XPS spectra of sZIF-8. Reproduced with permission from ref. 125. Copyright © 2022, Elsevier Ltd.

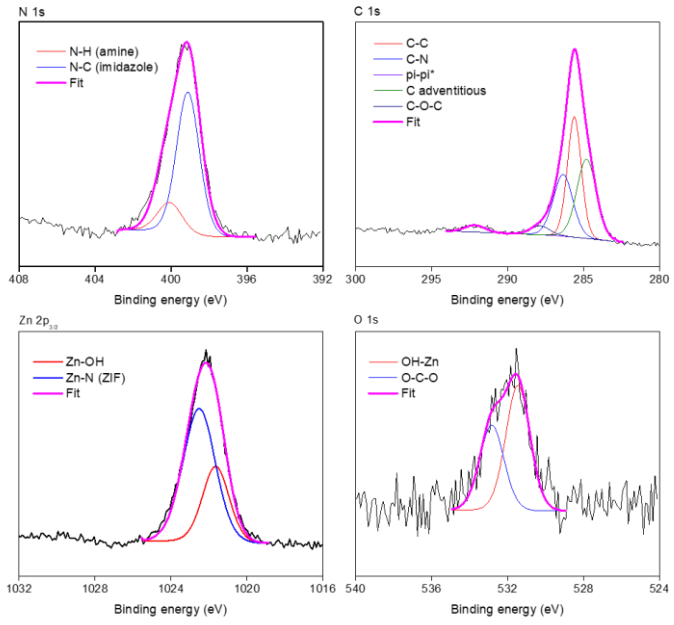

Figure 37: N1s, C 1s, Zn $2p_{3/2}$, O 1s region of XPS spectra of sZIF-8-MWCNT. Reproduced with permission from ref. 125. Copyright © 2022, Elsevier Ltd.

5.3 Ab initio Density Functional Theory

The modelling of the possible catalytic active sites on the ZIF-8 material, detailed highlights the possible reaction pathways and the energies activation for each products of each site. From the surface characterization techniques, we are to identify two possible defects on the periodic structure, which possibly work as active sites. The most abundant undercoordinated imidazole sites, partially protonated in order to achieve the neutral surface, and secondary Zn sites in which the fourth imidazoles is substituted by water. Under this perspective, both the active site were modelled by DFT.

5.3.1 Imidazole-imidazolate pair free surface

Starting with the imidazolate sites, recent studies have proven that CO_2 can form a covalent bond to them by forming a Lewis acid-base adduct in which the CO_2 molecule is bent[144,145]. Here we exploit such finding and prove that the activated CO_2 molecules can be further reduced by subsequent electrocatalytic steps. The ZIF-8 material acts as an ordered and robust imidazole-based structure in which Zn^{2+} cations have the role of anchoring the imidazolate anions[146] in an ordered crystalline arrangement. In order to model and study the catalytic site, a proper facet of the ZIF-8 material must be chosen. The low-index ZIF-8 (110) facets resulted to be the most stable among all the possible facets[147,148] and their prevalence in rhombic dodecahedron crystals, like the one experimentally observed[136,137,135,138]. The CO_2RR electrochemical tests are performed always in a buffer pH solution having different concentration of $KHCO_3$. Once saturated with the CO_2, even the more concentrated 2M $KHCO_3$ shows almost neutral pH or at least slightly acid condition, so it is plausible to investigate imidazole/imidazolate-terminated ZIF-8 (110) surfaces, which recent computational investigations proved the thermodynamical stability of this surface termination in such pH range[140]. In this configuration the ZIF-8 (110) surfaces expose imidazole (*L-H) - imidazolate (*L) pairs (in which the * indicates the underlying ZIF-8 structure) as represented in Figure 38a. The *L-H and *L species coordinate Zn^{2+} species which are 6.02 Å apart. This configuration is stabilized by a hydrogen bond (HB) established between the hydrogen atom of the *L-H and a nitrogen atom of the nearby *L.

Due to the nature of the sZIF-8-MWCNT to integrate inside the material MWCNT, their presence on the material was also modelled. The effect of the carbon nanotubes was modelled by interfacing two ZIF-8 clusters of different sizes (ZC1@CNT and ZC2@CNT) with a metallic (8x8) carbon nanotube (Figure 38b

and c). Smaller ZIF-8 clusters (ZC2@CNT) appear to be relevant to investigate size effects on the electrocatalytic performances.

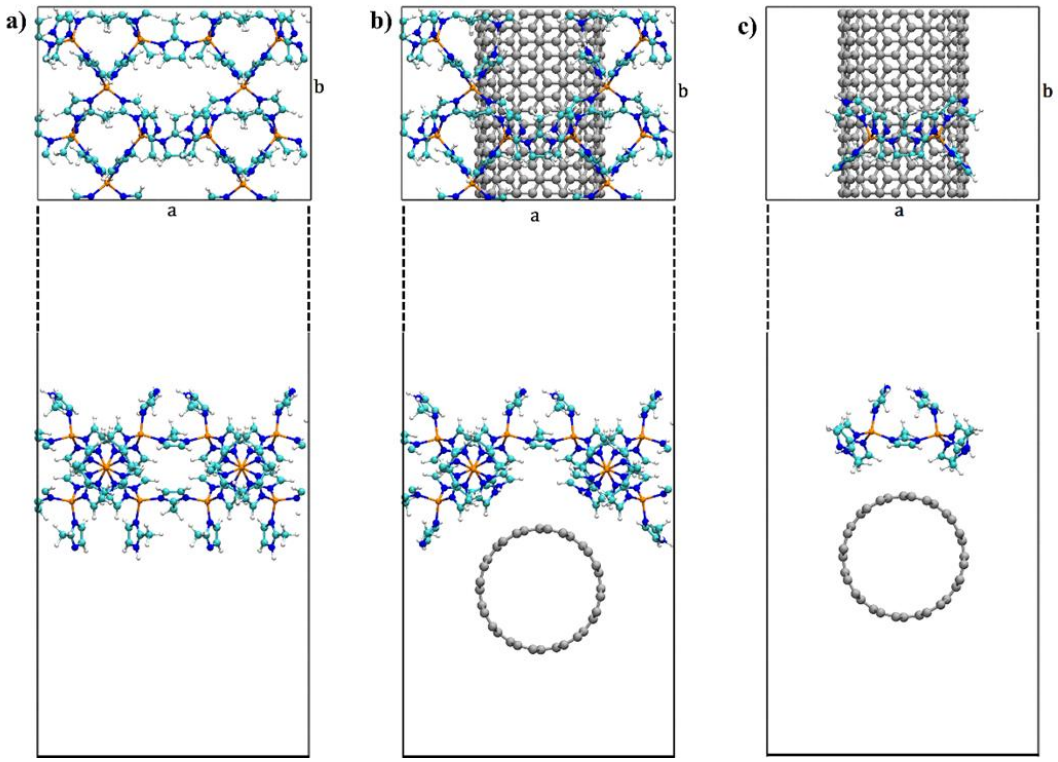

Figure 38: Simulated ZIF-8 structures: a) ZIF-8 (110) surface, b) ZC1@CNT and, c) ZC2@CNT. Color code representation: orange for zinc atoms, cyan for carbon atoms, blue for nitrogen, dark grey for CNT carbons. Reproduced with permission from ref. 125. Copyright © 2022, Elsevier Ltd.

Since the stable ZIF-8 surface at operative reduction conditions exposes the *L-H/*L termination and knowing that CO_2 can covalently bind to imidazolate species, we suggest and study the following CO_2RR mechanism:

$$CO_2 + 2H+ + 2e- \rightarrow CO + H_2O$$

Which unfolds into three steps,

$$*L\cdots H\text{-}L^* + CO_2 \rightarrow *L\text{-}COO\cdots H\text{-}L^* \qquad \text{Equation 18}$$

$$*L\text{-}COO\cdots H\text{-}L^* + (H+ + e^-) \rightarrow *L\text{-}COOH\cdots H\text{-}L^* \qquad \text{Equation 19}$$

$$*L\text{-}COOH\cdots H\text{-}L^* + (H+ + e^-) \rightarrow *L\cdots H\text{-}L^* + CO + H_2O \qquad \text{Equation 20}$$

yielding CO and H_2O. In the first step (Eq.8) a Lewis adduct *L-COO is formed in which the imidazolate nitrogen atom acts as Lewis base while the CO_2 as Lewis acid. Then two electrochemical reduction proton-electron coupled steps (Eq. 9 and 10) occur, which lead to the release of the final products (CO and H_2O) and consequent regeneration of the active surface. Such pathway presents an analogous mechanism of a previous study, in which the CO_2RR reduction is completely performed without using the CO_2 dissolved in the electrolyte, or directly in the gas phase, rather in the form of carbamate bonded to the monoethanolamine[149].

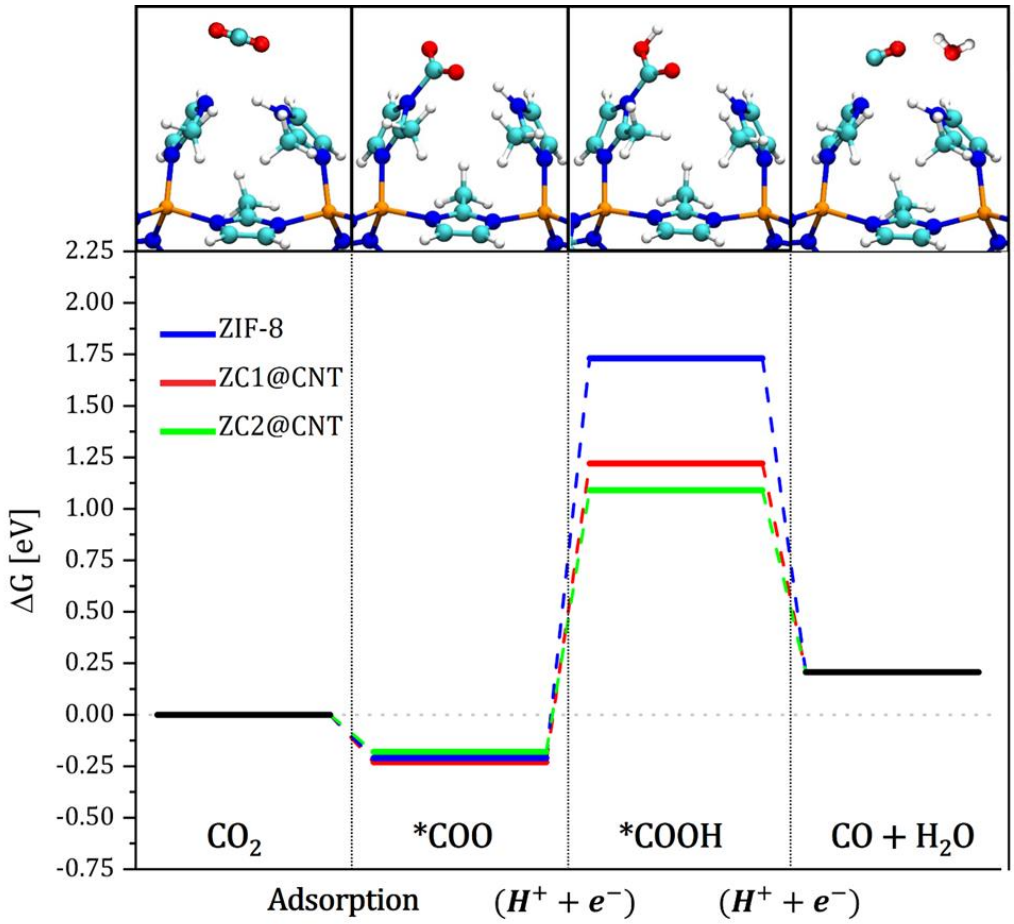

Figure 39: CO_2RR pathway forming CO and H_2O on ZIF-8 (blue line), ZC1@CNT (red line) and ZC2@CNT (green line) at U = 0 V vs RHE. Reproduced with permission from ref. 125. Copyright © 2022, Elsevier Ltd.

Figure 39 shows the calculated free energy profile of the CO_2 electrochemical reduction reaction to CO and H_2O at U = 0 V vs RHE considering the imidazole/imidazolate sites. The blue path corresponds to CO_2RR on ZIF-8 (110) surface (named ZIF-8), while the red and green lines represent the reduction steps

on ZC1@CNT and ZC2@CNT, respectively. In all pathways, the first reaction step, i.e. the nucleophilic addition of N^- moiety to CO_2 is spontaneous ($\Delta G_{*CO2\rightarrow *COO} < 0$). Upon the formation of *L-COO adduct, a C-N bond 1.569 Å long is formed. Consequently, the CO_2 molecule is bent (OCO angle of 134.39° degrees) and activated for subsequent reduction. This configuration is further stabilized by an HB between the *L-COO group and the nearby H-L* ligand. Such results evidence the great advantage of the CO_2 chemical activation compared to the high-energy electrochemical step. For all three pathways, we found a similar energy trend which highlights that the overall reaction is not spontaneous at U = 0 V and a negative onset potential (U^r_{onset}) must be applied. The first electrochemical reduction step ($\Delta G_{*COO\rightarrow *COOH}$) is uphill and it determines the U^r_{onset} of the reaction for all considered model structures. The energy needed to convert *COO to *COOH is markedly higher on the ZIF-8 surface ($\Delta G_{*COO\rightarrow *COOH}$ = 1.95 eV) compared to that on the CNT supported ZIF-8 system ($\Delta G_{*COO\rightarrow *COOH}$ = 1.45 eV for ZC1@CNT). The presence of a metallic CNT support appears to facilitate the first proton-electron transfer to the *COO intermediate and decreases the $|U^r_{onset}|$ of about 0.5 eV. A further $|U^r_{onset}|$ decrease is observed by reducing the ZIF-8 cluster size in contact with the CNT (ZC2@CNT). Indeed, in the reaction path of the latter system U^r_{onset} is decreased to 1.27 eV, suggesting that a smaller ZIF-8 structure, and thus a closer proximity of the active site to the CNT surface, further improves the efficiency of the overall catalytic performances of the ZIF-8/CNT system.

5.3.2 Water coordination by Zn^{2+} sites

Despite the more stable surface exposing undercoordinated imidazole ligands, it is possible that in aqueous environment and at experimental conditions the ZIF-8 surfaces present defective Zn sites, not fully coordinating terminal Im^-/Im ligands, which react with water bonding to OH^-/H_2O species, as suggested by XPS spectra (Figure 37). For this reason the reactivity of a ZIF-8 facet exposing zinc centers saturated with OH^-/H_2O was studied. The Zn-OH species experimentally observed have been studied by DFT simulations to investigate their activity towards CO_2RR and the competitive HER. In this perspective, we considered the charge-neutral surface ZIF-8 (110) terminated by hydroxyls (*OH) and water (*H_2O) species coordinated to Zn atoms (Figure 40). The ambivalence of OH^-/ H_2O ligand comes from the charge compensation required to compensate the Zn cations which are present together with the imidazolate ligands with a stoichiometry of Zn^{2+}: Im^- → 1 : 2.

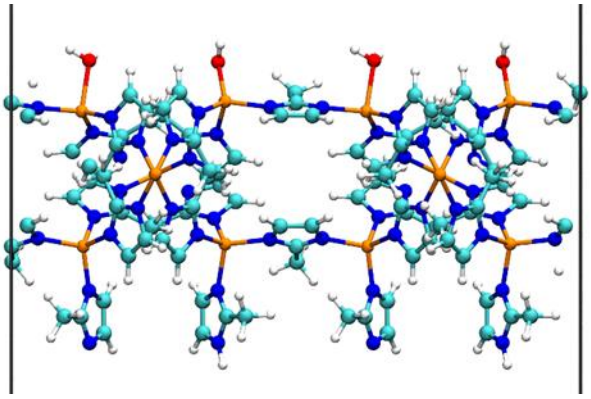

Figure 40: Simulated ZIF-8 (110) surface terminated by hydroxyl anions and water molecules. Color code representation: orange for zinc atoms, cyan for carbon atoms, blue for nitrogen, red for oxygens atoms. Reproduced with permission from ref. 125. Copyright © 2022, Elsevier Ltd.

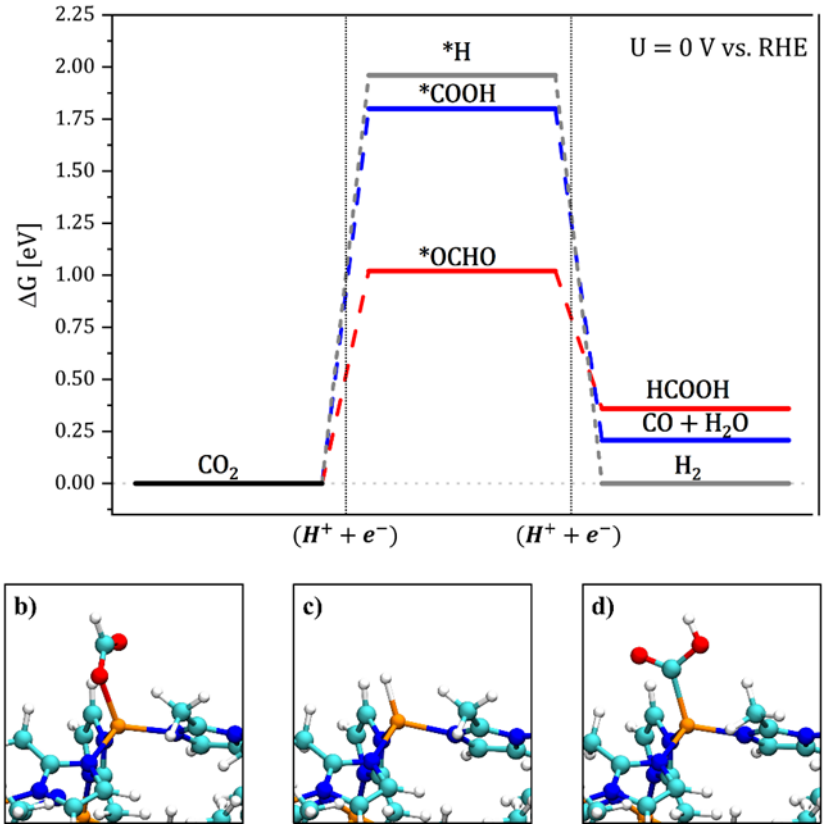

Figure 41: CO_2RR and HER on ZIF-8 (110) surface terminated by hydroxyls and water species: panel a) displays the free-energy profiles for HCOOH (red line), H_2 (grey line) and CO (blue line) at U = 0 V vs RHE; panel b), c) and d) represent *OCHO, *H and *COOH intermediates, respectively. Color code representation: orange for zinc atoms, cyan for carbon atoms, blue for nitrogen, red for oxygens atoms. Reproduced with permission from ref. 125. Copyright © 2022, Elsevier Ltd.

At the surface, Zn atoms must expose an undercoordinated site to be directly involved in reduction process and the coordinative vacancies can be formed through the exit of one ligand. Water molecules are known weak ligands, easily replaceable by incoming species, on the other hand, hydroxyl anions are species strongly bonded to the metal and must protonated to $*H_2O$ in order to unlock the active site. The calculated energy $U_{onset}^{*OH \rightarrow *H_2O}$ corresponding to the protonation step of hydroxyl anion is of -1.50 V, a higher value compared to the operational condition (-1.2 V). For this reason, the catalytic pathway involving water de-coordination will be considered.

We considered the CO_2 conversion to C_1-products, i.e. formate (HCOOH) and carbon monoxide (CO), as well as the molecular hydrogen (H_2) production on Zn atom coordinating a water molecule. Figure 41 shows the free energy profiles of the three above-mentioned reactions at U = 0 V vs RHE employing solvation energy corrections[89,150]. For all the three pathways, the first electrochemical reduction step, which leads to the adsorbed intermediate, is uphill and it determines the $U_{onset}^{r}$of the reaction, highlighting that ZIF-8 (110) surface terminated by water molecules is selective towards formic acid. Such results is experimentally coherent with the small value of formate detected during the electrolysis and to the restricted amount of Zn-OH sites registered.

In summary, from a theoretical point of view, it is anticipated that ZIF-8 based electrocatalysts would present two possible kinds of active sites, the main molecular, one originating from the Im and Im^- pair selective for CO production, and a secondary one, in which Im and Im^- have been substituted by OH^-/H_2O ligand, selective for $HCOO^-$.

5.4 Electrochemical performances

All the electrochemical tests were performed on a micro flow cell reactor bearing a Nafion PEM. The reported potentials are always referred to the RHE.

Preliminary tests investigation were performed on a batch cell reactor having a Nafion PEM as separator between the two chambers. The sZIF-8 and sZIF-8-MWCNT electrodes were tested in a 0.1 M $KHCO_3$ solution, showing the best selectivity of 48.7% and 65.7%, respectively for the CO_2RR (FE_{CO2RR}) at -1.2 V for both the samples. For the former, parallel to a lower FE also a lower current density

of 5.7 mA cm^{-2} is reached, moreover characterized by poor stability of the electrolysis. Such low current density is due to the intrinsic low electrical conductivity of ZIF-8[151] and the stability is correlated to its strong interaction with the polar electrolyte. sZIF-8 catalyst detaches from the gas diffusion layer (GDL) substrate during the electrolysis leading to the support exposure to the electrolyte, which inevitably favors the hydrogen production[152]. Such problem does not occur with the sZIF-8-MWCNT catalyst, which results firmly attached to the electrode and shows a higher current density of 7.0 mA cm^{-2} in the same batch cell setup. MWCNT introduces hydrophobicity to the material, which prevent its detachment from the electrode all along the electrolysis.

Once the better experimental performances of the sZIF-8-MWCNT had been established, the catalyst was further tested in a flow cell configuration having the electrolyte recirculation. Several concentrations of $KHCO_3$ water solution (0.1, 0.5, 1.0 and 2.0 M) and at different potentials (-1.2, -1.0 and -0.8 V) were combined in order to establish the best operational condition. The complete information about relative selectivity and current densities is plotted in Figure 42. A more compact plot which reports only the FE_{CO2RR} of different electrolyte at -1.2 V vs RHE is plotted in Figure 43a. Such plot evidences the current density increases parallel to $KHCO_3$ concentration at each potential, the same for the FE_{H2} and FE_{HCOO-} with the exception of the 0.5 M value, where lower hydrogen evolution was registered. Indeed, the highest selectivity is reached in 0.5 M $KHCO_3$, with FE_{CO} of 65.8% and total FE_{CO2RR} of 70.4% at -1.2 V (Figure 43a). However, despite the great selectivity, this electrolyte leads to a lower current density (Figure 43a, red line) compared to the more concentrated ones (1.0 and 2.0 M). Taking into account the overall electrode activity at the same potential (Figure 43b), the 1.0 M $KHCO_3$ results in the highest turnover frequency number (TOF_{CO2RR}) value of 230.4 h^{-1} (Figure 43b) considering the number of N atoms forming the active site. Another observation can be extrapolated from Figure 43a about the secondary product $HCOO^-$. It is indeed visible that FE_{HCOO-} grows parallel to the $KHCO_3$ concentration in the electrolyte. Since the DFT modelling predict the formate production in presence of surface Zn sites coordinating the OH^-/H_2O ligands, it is plausible that in an electrolyte having a higher dielectric constant, i.e. more salt dissolved, the dissociation of the coordinated water molecules can be easier with a better shielding of zinc charge.

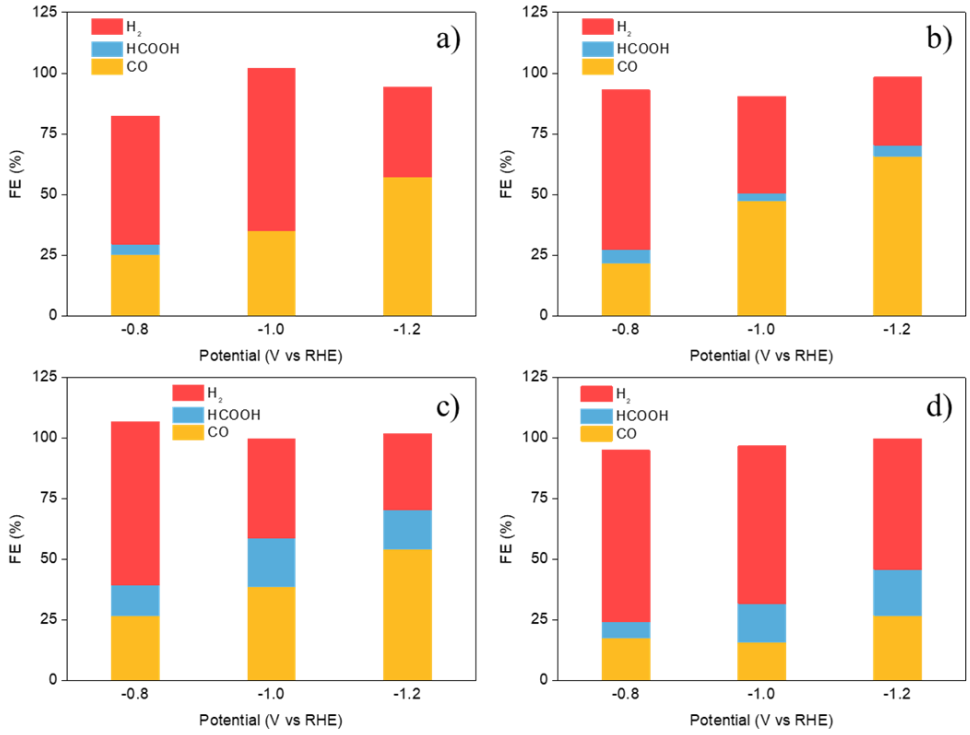

Figure 42: Chronoamperometric tests in different electrolytes and potentials. a) 0. a) 0.1 M $KHCO_3$, b) 0.5 M $KHCO_3$, c) 1.0 M $KHCO_3$, d) 2.0 M $KHCO_3$. Reproduced with permission from ref. 125. Copyright © 2022, Elsevier Ltd.

To evaluate the best conditions of stability and operability of the investigated catalyst, several prolonged electrolysis tests were performed on the sZIF-8-MWCNT catalyst. A 20-hour test at -1.2 V vs RHE in 0.1 M $KHCO_3$ shows a good retention of selectivity along all the hours, in terms of both selectivity, current density (Figure 43c) and CO production rate (Figure 43d) with a value over the 0.05 mmol h^{-1} cm^{-2} at -1.2 V in 0.1 M $KHCO_3$. A different stability test of more than 40 hours was instead tested in 1.0 M $KHCO_3$ electrolyte (Figure 43e and f). After the highest value of 0.13 mmol h^{-1} cm^{-2} registered in the first few hours, a quite stable value of 0.8 mmol h^{-1} cm^{-2} was obtained in the remaining time, showing only a minor rise with time due to the accumulation of formate in recirculating electrolyte. Considering instead the current density, a significant and constant increase occurs all along the measurement. Such effect it was a constant attitude registered all along several tests in such electrolyte. The reason of this phenomena is still of active debate. We encountered this trend only on non-conductive materials, e.g. no metallic species. This can involve that, all along the measurement, the material change its characteristic becoming more conductive, e.g. catalyst

deactivation and metallic particles formation. Anyway, such behavior must be clarified throughout in situ characterization under bias.

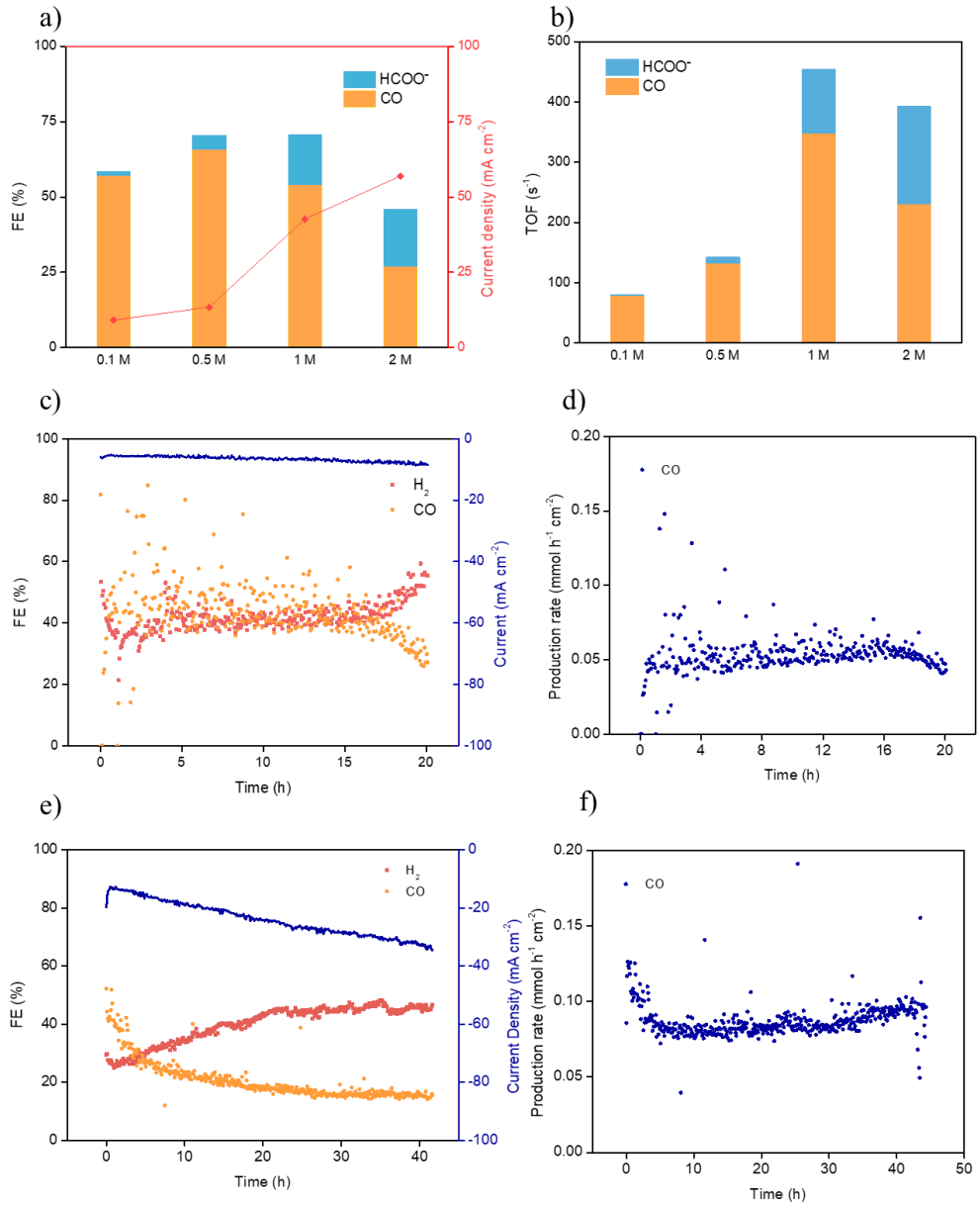

Figure 43: Semi-flow cell CO_2RR investigation on sZIF-8-MWCNT electrodes. a) FEs and current densities at -1.2 V in different electrolyte compositions and b) the relative TOFs. Stability test in 0.1 M $KHCO_3$ at -1.2 V vs RHE c) FE and current density as a function of time and d) CO production rate during a 20-hour stability test. Stability test in 1.0 M $KHCO_3$ at -1.2 V vs RHE e) FE and current density as a function of time and f) CO production rate during a 40-hour stability test. Reproduced with permission from ref. 125. Copyright © 2022, Elsevier Ltd.

As a counterproof of the role of the imidazole supported on ZIF-8 catalyst, an electrode composed only by treated MWCNTs was tested at the same conditions and showed no selectivity for the CO_2RR, producing only H_2. Hence, it is possible to state that ZIF-8 and MWCNTs play synergic roles in the CO_2RR, in which the former provides selective and active imidazole-imidazolate sites able to perform the catalytic and electrocatalytic reduction of CO_2, while the MWCNT favors the electrical conductivity of the catalyst increasing also the overall stability.

Chapter 6

Electrografted Cu-porphyrin

In all the previous chapters, several different approaches were investigated in order to prepare single metal active site catalysts for the CO_2RR. The doped polyanilines are the materials most resembling this strategy, unfortunately they resulted characterized by a low activity. The doping approach mimed the chemical nature of the metal organic complexes, in which a cation coordinates the organic ligands being stabilized and electronically enriched. In the doped polyaniline, a lot of effort was pushed to produce a similar structure. The organic ligands are substituted by the entire polymer, in which the organic functionality is being coordinated by the cations. In order to study a more solid and functional approach, the concept of single metal active site was reconsidered coming back to the canonical approach of metal organic complex as single metal active site.

As mentioned in the introduction, the metalloporphyrins reside a special place among the possible metal organic complexes known for the electrochemical conversion of CO_2, due to their stability and activity. For this reason, a 5,10,15,20-Tetrakis-(4-aminophenyl)-porphyrin (TAPP) complexed by Cu^{2+} cation was investigated as model catalyst. The typical application of metalloporphyrins for CO_2RR is in homogeneous conditions, i.e. with the catalyst dissolved in the electrolyte. Due to the chemical nature of these molecules, water is not a possible solvent to dissolve the major part of these catalysts, as a consequence the employment of organic solvents is the most known approach. The organic electrolytes show significant limitation, reason to drive all the investigation to some new approaches in order to avoid the catalyst dissolution and consequently work with water-based electrolyte.

In the simplest approach, the catalyst was deposited on a GDL, by drop casting, after being dispersed in an iPrOH solution forming a slurry. Due to the highly hydrophobic nature of the porphyrin, the catalyst remains perfectly attached on the GDL support once facing the water electrolyte, even during the electrolysis and consequent gas evolution. A more elaborate strategy was then investigated involving not a deposition of catalyst powder on the substrate, but rather than an

actual covalent bond between catalyst and carbon support through the electrografting. This method would lead to reach only a molecular layer of catalyst and thus avoiding its stratification. The electrografting was performed by the oxidation of the aniline substituent which eventually led to the formation of a C-N covalent bond[153]. The reaction mechanism reported in Figure 44 from the work of Buriez et. al[153] shows how under a positive bias, the electrochemical oxidation of the aromatic amino group produces the relative radical cation. Being the electrochemical process evolved in a base solution, the radical cation rapidly reacts with the organic base generating a neutral radical on the amino group. Such species is extremely reactive and concentrated in the first layer of the electrode where the oxidation occurs, thus will mainly react with its surface. In the cited work, a functionalized ferrocene complex bearing the before mentioned aniline substituent, was able to be electro grafted on several surfaces of carbon, platinum and gold.

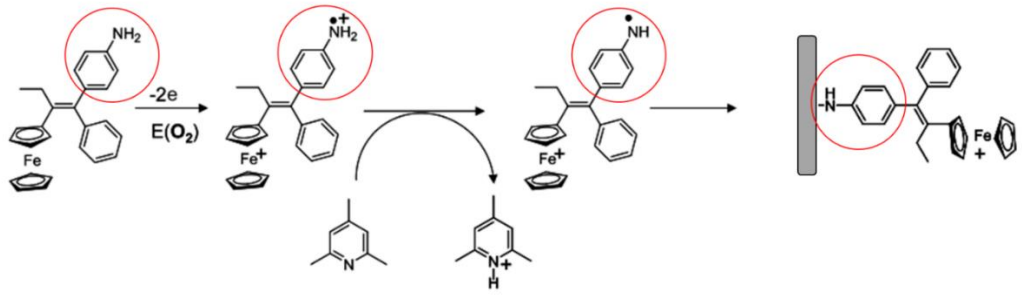

Figure 44: Electrografting mechanism of amino group oxidation. Reproduced with permission from ref. 153, Copyright © 2008 Elsevier B.V.

The choice of the TAPP as model porphyrin of the investigation comes from the necessity to have a catalyst bearing the aniline functionality. Such molecule is commercial and its complexation with copper cations was performed before to proceed with the electrografting. The electrografting was firstly performed by cyclic voltammetry technique on two different forms of carbon supports: the carbon paper (CP) and the GDL. The former is a mixture of carbon nanofiber filled with carbon nanoparticles which makes the substrate gas-permeable; once an additional hydrophobic layer (PTFE dispersion) is added to the CP, the resulting hydrophobic electrode becomes a full GDL. Only once the catalyst layer is deposited to the latter, the full Gas Diffusion Electrode is completed.

The cyclic voltammetry resulted a slow method to reach a homogeneous coverage of the CP electrodes. Instead, on GDL substrate this technique failed, not

showing any trace of catalyst bonded. The grafting procedure by cyclic voltammetry was thus substituted with the chronoamperometry technique, in which a fixed oxidative potential led to a homogeneous functionalization of both substrates (CP and GDL), adjusting the operative time in the range tens of seconds in accordance to the nature of the substrate and its dimension (details reported in the next sessions). In order to evaluate the stability of the catalyst and to proceed with an ex-situ characterization of the active sites, several other substrates were evaluated. In details, the glassy carbon (GC) and highly ordered pyrolytic graphite (HOPG) supports were electrografted, tested and re-analyzed in order to better understand the chemical nature of the active sites. The choice of these supports comes from their highly ordered morphology which makes clearer the ex-situ investigation.

6.1 Physical chemical characterization

6.1.1 UV-Vis spectroscopy

The 4-aminophenyl porphyrin, TAPP, was purchased from Merck and utilized without further purification. In order to complex the molecule with copper cations, 200 mg of TAPP were dissolved in MeOH inside a reaction flask, then an excess of 1.5 mol of $Cu(NO_3)_2$ was added into the solution, Figure 45. The reaction happens instantaneously at room temperature once the copper salt is added to the TAPP. The violet colour of the solution rapidly turns into an intense red. The glassware was then connected to a refrigerator and the solvent placed at reflux temperature for 2 h. The solvent was evaporated using a rotovapor and the excess of copper salt was removed with several washing with deionized water. The purple powder was dried in the oven until constant weight.

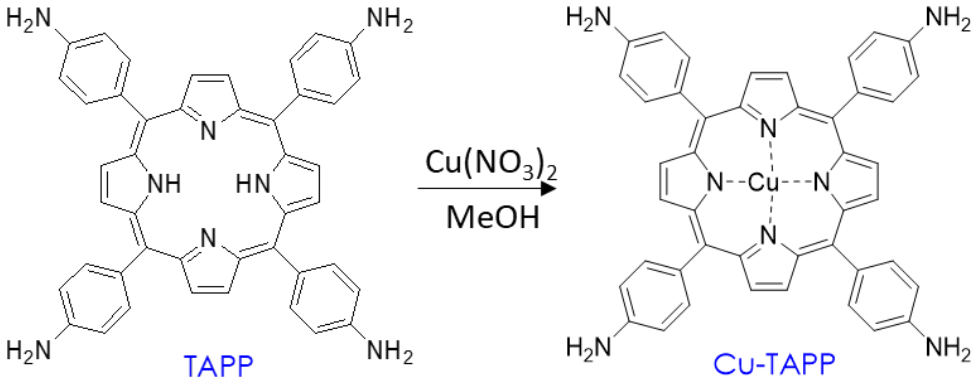

Figure 45: TAPP chemical reaction with copper salt.

In order to characterize the complete reaction with the copper center, the UV-Vis spectroscopy was performed on solutions. The TAPP and CuTAPP powders were dissolved in NMP solvent and analyzed in the range of 300 – 1000 nm. The TAPP presents a C_2 symmetry in which the four nitrogen atoms at the center of the molecules are not degenerate. Once the coordination occurs, the two pyrollic hydrogen atoms are dissociated forming a $TAPP^{2-}$ specie, consequently, the four nitrogen atoms become degenerate, thus increasing the symmetry of the molecules to a C_4. The increased symmetry influences the orbital levels of the molecule and the consequent electronic transitions. In Figure 46a, the UV-Vis spectra of NMP dissolved TAPP and CUTAPP compounds are reported. The main transition around the 400 nm is named Soret band, and it is the most intense transition for all the porphyrin. Between TAPP and CuTAPP, the Soret band shows a slight wavelength shift due to copper coordination. For the TAPP, four additional transitions are present (magnified in the inset) and schematized in Figure 46b. They are named Q bands and B bands and come from the transitions among the HOMO, HOMO-1, LUMO and LUMO-1 orbital levels. Once the molecule is complexed, CuTAPP, the C_4 symmetry makes those orbitals pair degenerate, generating only two possible transitions and consequently bands, as reported in the inset of Figure 46b for CuTAPP[154]. The UV-Vis spectroscopy indeed evidences the correct total coordination of the porphyrin by the copper cation since the loss of the four Q and B bands is substituted to two new bands.

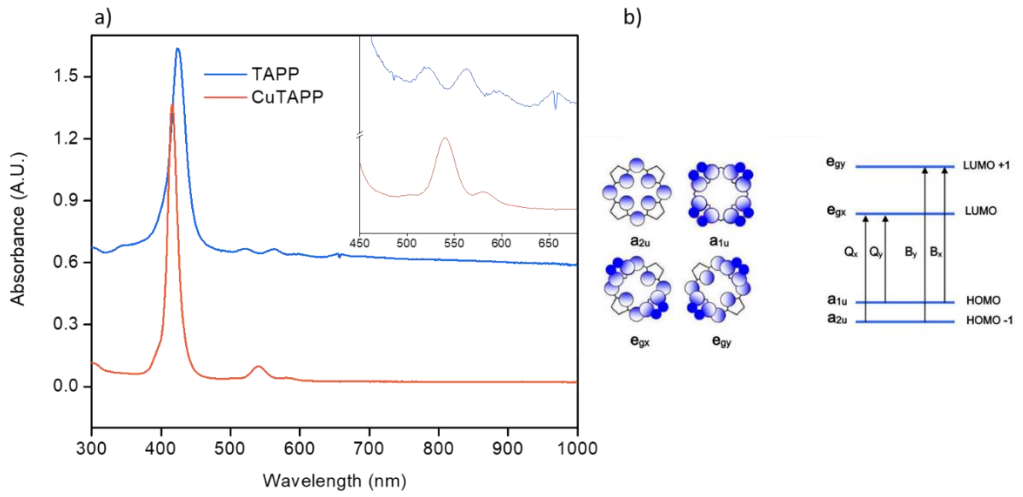

Figure 46: a) UV-Vis spectra of TAPP and CUTAPP in NMP solution. b) schematic representation of the four possible Q and B transitions on TAPP molecules.

The UV-Vis absorption spectroscopy clarified the chemical nature of the porphyrin priory to its electrografting; once covalently bonded to the surface by electrografting, there is no further knowledge of its chemical state. For this purpose, the UV-Vis spectroscopy in reflectance mode bearing the integration sphere helps to investigate the UV-Vis absorption on the molecules electrografted on the support.

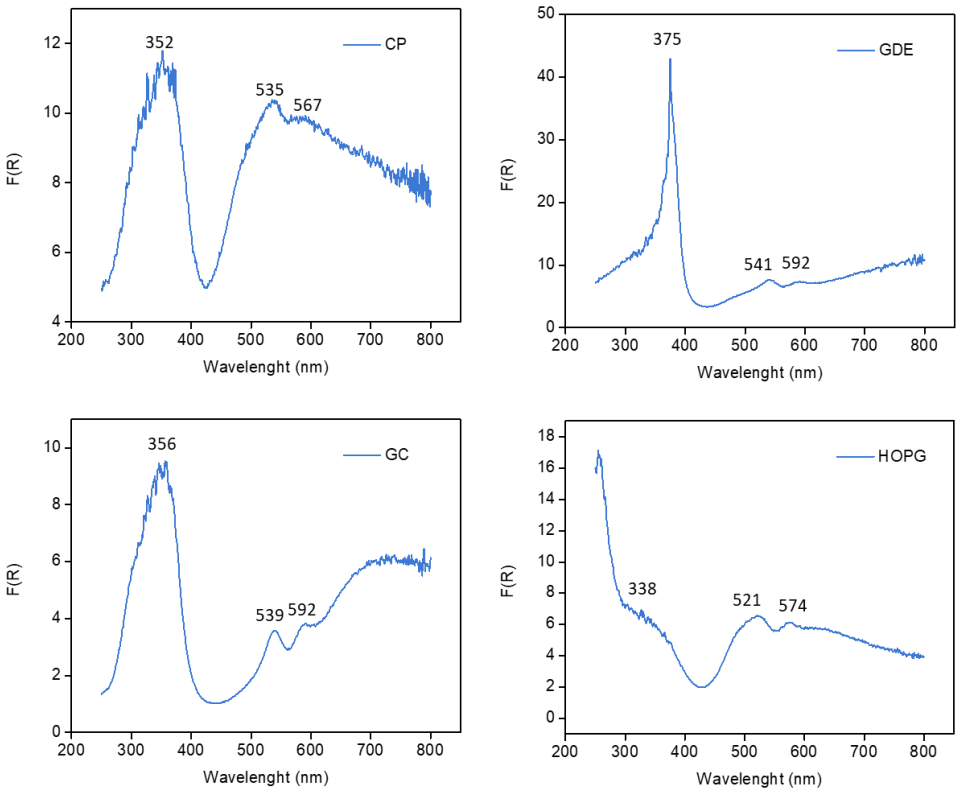

Figure 47: UV-Vis spectra in reflectance mode of electrografted supports: GC, HOPG, CP and GDL.

The same investigation was performed on all the electrografted supports: CP, GDL, GC and HOPG. If the UV-Vis spectroscopy in absorption mode furnishes detailed and clear spectra, in case of reflectance mode the information is noisier and more difficult to interpret. This occurs also considering the morphology of the samples, which are not flat, but rather rough and three-dimensional according to the specific carbon support. In Figure 47, all the four spectra of GC, HOPG, CP and GDL electrodes, after being electrografted, are reported after being processed with the Kubelka Munk function. The spectra show several differences due to the nature of the support, nevertheless is possible to identify one main Soret band and the two minor Q bands in any support, analogously to the absorption mode obtained spectra. The case of GC and GDL are the one more resembling the spectra obtained in the solution. In general, for all the four spectra, variations on the maximums wavelength are reported. This is also caused by the low resolution of those peaks. Nevertheless, in all the samples it was possible to identify the correct grafting of the porphyrin and its chemical state bearing the copper cation.

6.1.2 XPS

XPS analysis resulted to be a fundamental technique in order to distinguish the copper present as metallorganic complex and as the possible different inorganic form, i.e. metal/metal oxide, on the grafted electrodes. Moreover, XPS analysis further provides stability information about the active site once the analysis is repeated after the electrolysis, i.e. ex situ.

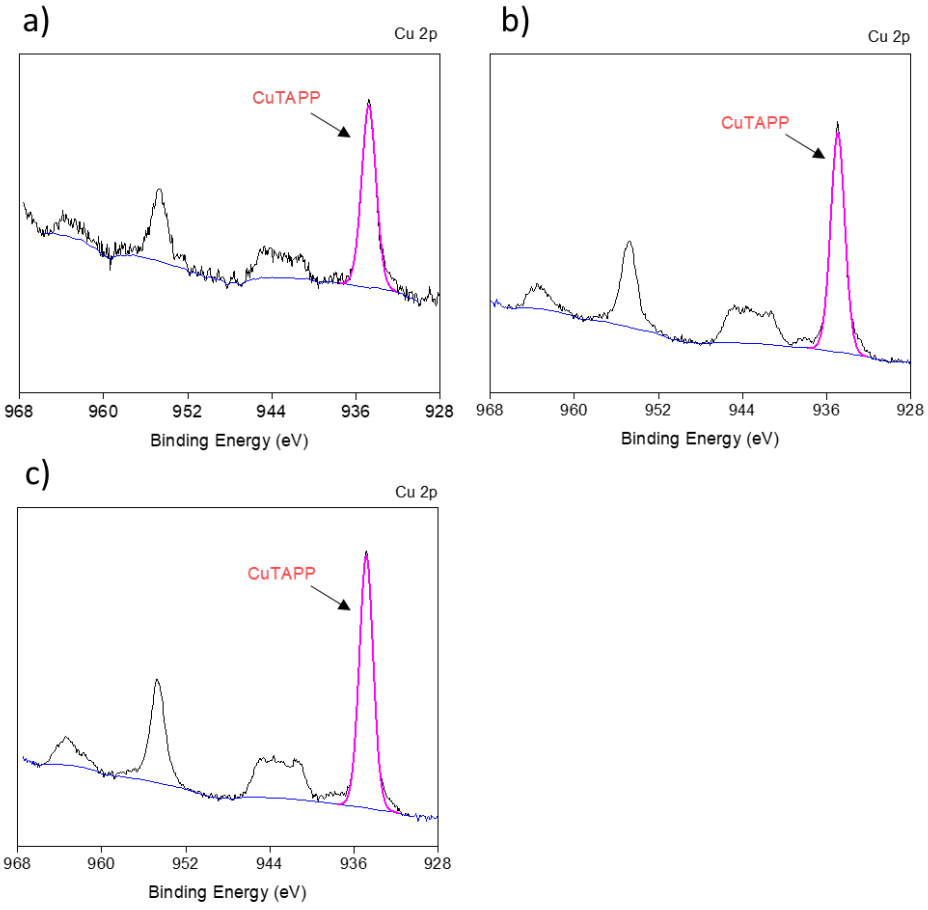

Figure 48: XPS spectra Cu 2p region of a) CuTAPP-CP, b) CuTAPP-GC and c) CuTAPP-HOPG.

The XPS analysis was performed directly pointing the X-Ray source on the surface of the electrografted electrodes, actually analysing the porphyrin being grafted on the support in its real condition rather than as mere powder.

From XPS analysis it is possible to collect the information of C 1s, N 1s, O 1s and Cu 2p. Due to the complexity of the molecule, the main source of information

comes from the nitrogen and copper signals. In Figure 48, the plot of the Cu 2p spectra for all the three electrodes CuTAPP-CP, CuTAPP-GC and CuTAPP-HOPG are reported. These spectra are the ones of the virgin samples, being electro-grafted and not yet been tested for the electrolysis.

The reported Cu 2p regions of the virgin electrodes show a similar pattern for each grafted support. As evidenced in Figure 48, in each spectra are present the typical pair of peaks of Cu around 955 and 935 eV (coming from the $2p_{1/2}$ and $2p_{3/2}$ orbital) together with their satellite signals. The detailed values of the main peaks of each support are reported in the Table 5 together with the reference values of the inorganic Cu, Cu_2O, CuO and $Cu(OH)_2$[101]. Qualitatively, the presence of the satellite peaks suggests a Cu^{2+} specie. Moreover, the intensity of the satellite signals is lower compared to the main peaks of almost a third. In CuO and $Cu(OH)_2$ species, the intensity of the satellite signals is instead comparable to the main peaks, suggesting that for the electrografted electrodes a different Cu^{2+} compound is involved. This information is also confirmed by the Cu2p and Cu LMM values reported in the Table 5. The registered Cu 2p peaks for the grafted samples defer from the Cu, CuO and Cu_2O reference values, while there is a good match instead with the Cu 2p data of the copper hydroxide. Although, a great mismatch is present for the Cu LMM peak signal of the latter, confirming the presence of a not inorganic Cu^{2+} compound.

The experimental values are indeed similar to the reported literature of Cu^{2+}-tetrakisphenyl porphyrin (TPP) and Cu-tetrakis(pentafluorophenyl)porphyrin (CuTPP(F)), which bears indeed Cu^{2+} species and thus justifying the presence of copper as metal organic complex[155].

The N 1s spectra of the grafted electrodes is also highly informative and confirms the presence of the electrografted porphyrin, Figure 49. Indeed, in all the different grafted substrates, the main contributions of the four degenerate pyrollic nitrogen complexing the Cu^{2+} cations (namely N_4^{2-}), the four aromatic amine substituents (N-H (aniline)) and the N* satellite typical of the porphyrin samples are recorded. Such information gives us knowledge of the correct grafting of the organic compound and moreover its complexation as metallorganic CuTAPP[155,156]. Indeed, the absence of the contributions at 397.8 and 399.4 eV coming from the two pairs of protonated and un-protonated pyrroles, confirm that the Cu^{2+} cations completely coordinate the porphyrin[157], Table 6.

Table 5: Cu $2p_{3/2}$ binding energy, Cu $L_3M_{4,5}M_{4,5}$ kinetic energy, Auger Parameter (α') of reference materials (a)[101], of the electrografted samples CuTAPP-CP, CuTAPP-GC, CuTAPP-HOPG, and the reference[155] CuTPP and CuTPP(F) samples (b).

Compound	Cu $2p_{3/2}$ peak maximum E_b (eV)	Cu LMM Auger peak maximum E_k (eV)	Auger Parameter (eV)
[a] Cu	932.6	918.6	1851.2
[a] Cu_2O	932.2	917.0	1849.2
[a] CuO	933.8	917.6	1851.3
[a] $Cu(OH)_2$	934.7	916.3	1850.9
CuTAPP-CP	934.8	914.3	1849.1
CuTAPP-GC	935.0	914.9	1849.9
CuTAPP-HOPG	934.8	914.5	1849.3
[b] CuTPP	935.2		
[b] CuTPP(F)	935.7		

Further contribution is the NO_2 group at high binding energy, partially present in all the samples, with the exception of grafted CP. Such chemical group could be induced by the partial oxidation of the amino aniline group during the electrografting at positive potential. Finally, a further signal of interest, completely missing from the comparing literature, is the one registered at 402 eV. Such value is expected to be the one coming from the bond form from the nitrogen radical to the conductive carbon support (namely N (cond. C)). The high conductivity of the support indeed rises the binding energy of this peak, which partially shifts due to the different nature of the carbon support. This information further elucidates the covalent bond between the catalyst and the carbon support.

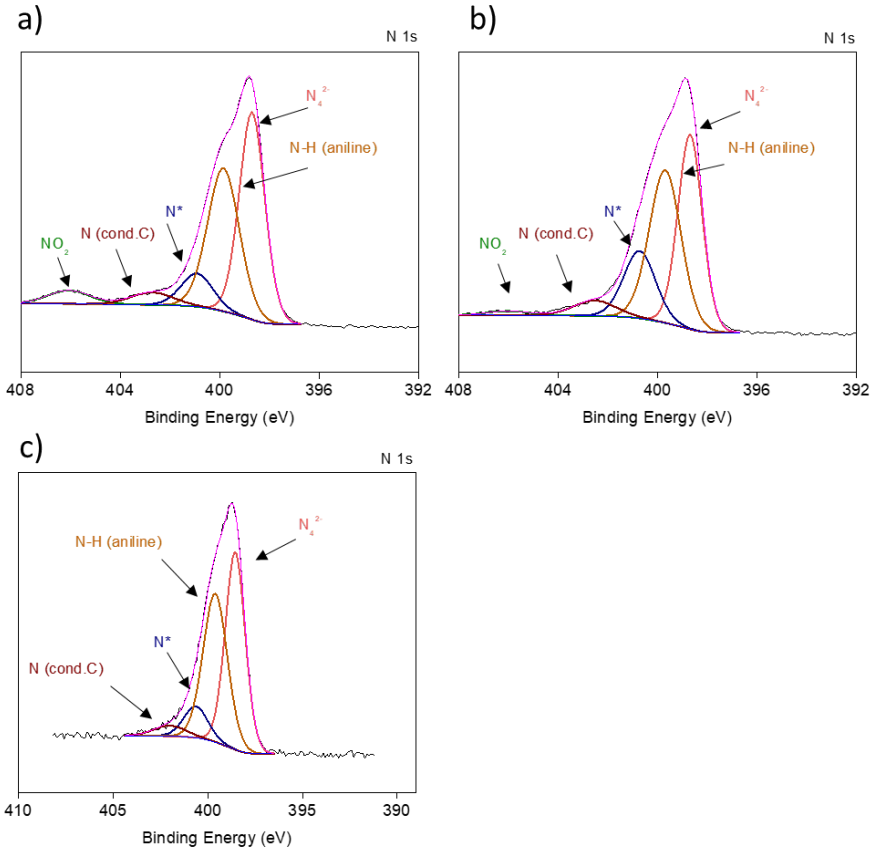

Figure 49: XPS spectra N 1s region of a) CuTAPP-CP, b) CuTAPP-GC and c) CuTAPP-HOPG.

Table 6: N 1s binding energy of reference materials (a), TAPP, Zn-TAPP[157] and of the electrografted samples CuTAPP-CP, CuTAPP-GC, CuTAPP-HOPG.

	[a] TAPP	[a] Zn-TAPP	CuTAPP-CP	CuTAPP-GC	CuTAPP-HOPG
-N= (TAPP)	397.8	-	-	-	-
N_4^{2-}	-	398.4	398.6	398.7	398.7
N-H (aniline)	399.4	399.8	399.6	399.7	399.9
N-H (TAPP)	400.0	-	-	-	-
N*	401.6	401.5	400.6	400.7	400.9
N (cond. C)	-	-	402.0	402.5	402.7
NO_2	-	-	-	406.0	406.1

6.1.3 FE-SEM

Through the electron-microscopy, the surface of the grafted electrodes was investigated both previously and after the electrochemical test as ex-situ characterization. In Figure 50 are reported three different magnifications of three different CP electrodes after being electrografted. In the first column are reported three different regions of a virgin CP, i.e. without electrografting. Respectively in the second and third columns are reported two grafted CPs respectively at +0.5 V and +0.8 V vs Ag/AgCl.

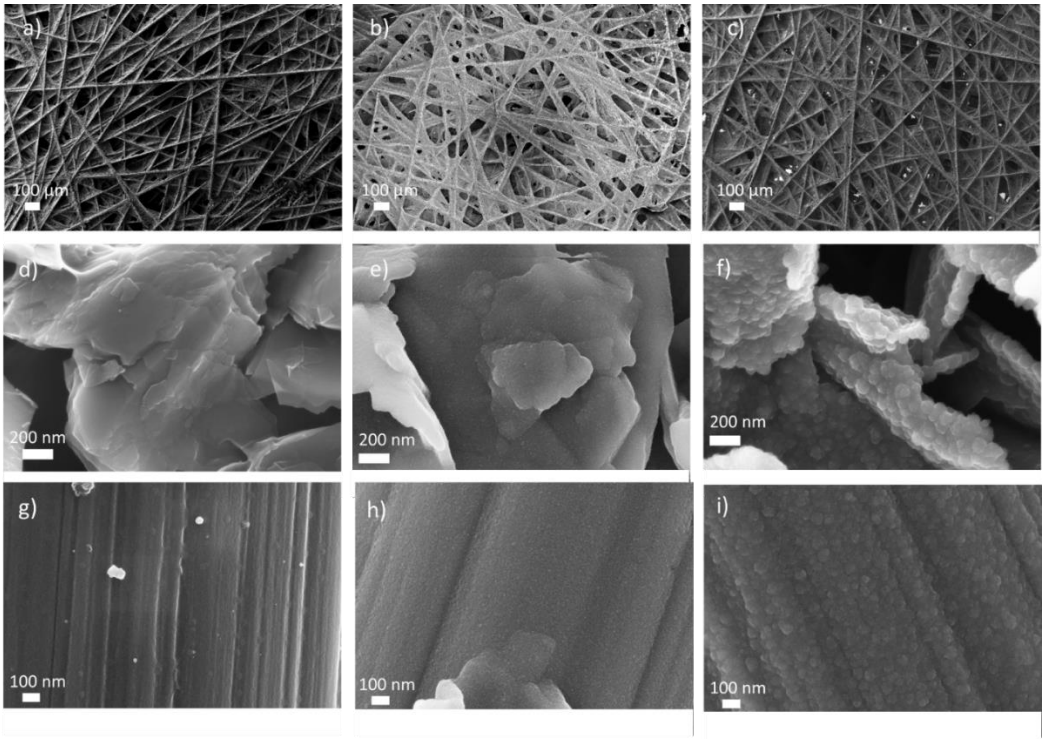

Figure 50: FE-SEM images of three different electrodes at three different magnifications. a,d,g) virgin carbon paper electrode, b,e,h) carbon paper electrode grafted at +0.5 V vs Ag/AgCl by CA and c,f,i) carbon paper electrode grafted at +0,8 V vs Ag/AgCl by CA. All the potential are reported vs Ag/AgCl reference electrode.

As it will be discussed in the next session, at +0.5 V vs Ag/AgCl starts the oxidation of the amino group, which causes the electrografting. If by chronoamperometry technique a homogeneous coverage of the electrode was already reached at +0.5 V, in the case of cyclic voltammetry electrografting, such coverage was reachable only pushing the bias to +0.8 V. In Figure 50 both the electrodes prepared by chronoamperometry at +0.5 V and +0.8 V are reported. First line is a magnification of different electrodes at a micro scale, second and third lines

show a specific regions having carbon nanofibers and carbon nanoparticles respectively.

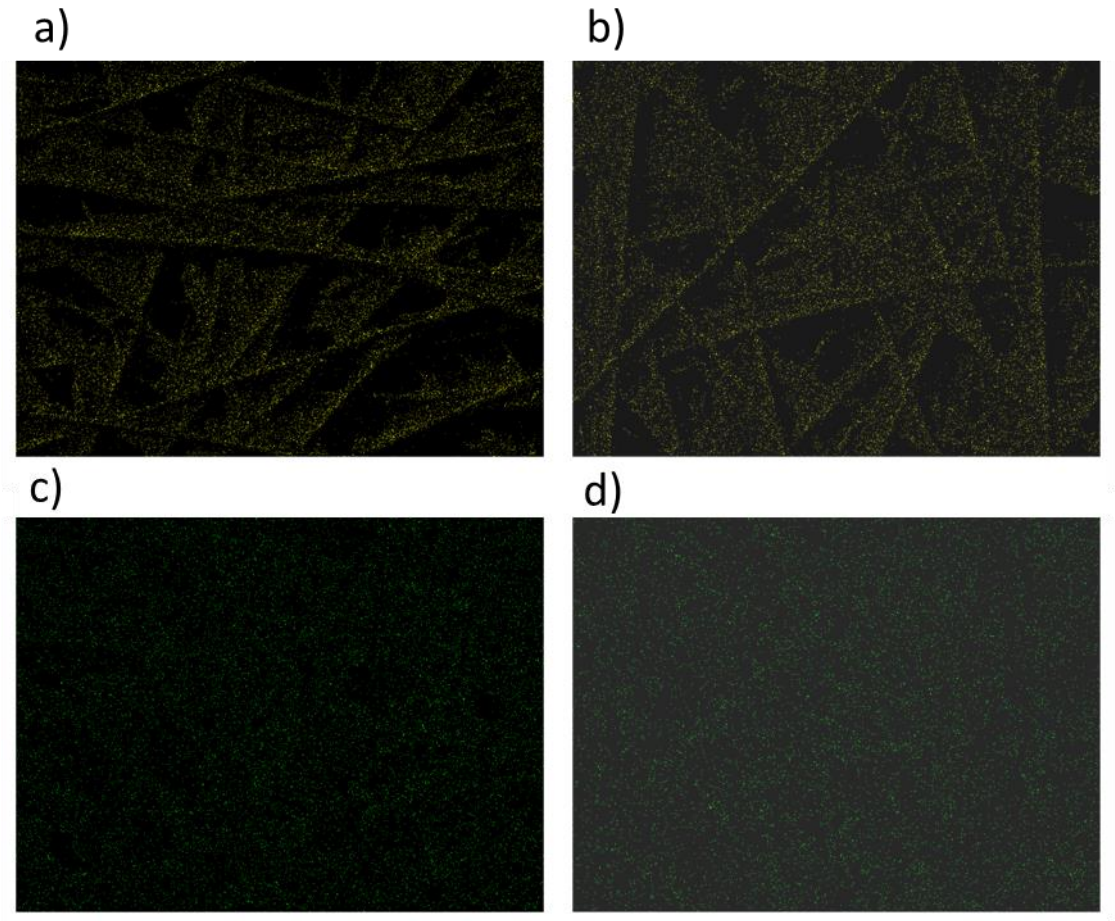

Figure 51: EDX mapping of copper and nitrogen atoms. a) and c) N atoms from electrodes +0.5 V and +0.8 V, b) and d) Cu atoms from electrodes at +0.5 V and +0.8 V vs Ag/AgCl.

As we can see, there is no actual covering of the original surfaces of the grafted electrode, which expose the same morphologies, with the exception of the new obtained roughness of the electrode, which clearly expose both the carbon nanofiber and carbon nanoparticles of the original electrode. Only increasing the magnification at a high value, it is possible to distinguish a homogeneous roughness all over the carbon nanoparticles which do not modify their size, rather change the actual surface. Shifting the grafting potential from +0.5 V to +0.8 V, causes a more evident roughness on the electrode, showing asperities of higher dimensions. FE-SEM characterization evidences how the electrografting approach does not cover

the carbon support like any other deposition technique, precisely because only the minimal amount of molecule can be bonded on the surface of the electrode, do not allowing any other progression in its grafting.

In order to evaluate the actual presence of the metal organic complex, also the Energy-Dispersive X-ray spectroscopy (EDX) was performed on both the electrodes. In Figure 51, the nitrogen atoms (Figure 51a and c) and copper atoms (Figure 51b and d) mapping are reported. The left column images are the ones obtained from CuTAPP-CP prepared at +0.5 V, the right column instead at +0.8 V. As we can clearly see, the metal complex is homogeneously spread all over the electrode without forming significant agglomerates, suggesting the presence of a perfectly homogeneous distribution of grafted complexes. Switching the potential from +0.5 V to more positive bias like the +0.8 V does not present any significant variation in the atom distribution from EDX images.

6.2 Electrochemical characterization

The electro-grafting methodology was firstly studied by cyclic voltammetry investigation as reported in the previous publication of Buriez et. al[153]. The experiment was performed on a mono chamber cell in which, a carbon paper foil was place as working electrode, a Pt foil as counter electrode and finally an Ag/AgCl electrode as reference. The cell was filled with a 0.1 M $LiClO_4$ anhydrous methanol solution.

A preliminary voltage scan was performed in the range of -0.2 V to +0.8 V with 100 mV s^{-1} of scan rate in order to evaluate the blank capacitive current of the electrode, Figure 52 black line. Successively the triethylamine (TEA) was added inside the electrolyte, reaching a title of 25 mM (red line) and also CuTAPP, reaching a 0.5 mM title (blue line). As we can see in Figure 52a, the oxidation of the TEA starts around the +0.6 V vs Ag/AgCl (magnification reported in Figure 52b) and does not reach a plateau. The CV in presence of the porphyrin shows an oxidative peak previously to +0.5 V and a negative one close to zero V. Interestingly, both the peaks are irreversible and they completely disappear on their second cycle. Pushing the scan rate at high value of 1 V s^{-1} it is possible to maintain these peaks for an interval of 2/3 cycles, suggesting the occurring reaction is exhausted already in the lifetime of the first cycle. The formation of the radical occurs therefore around +0.5 V, the minimal potential required in order to achieve

the grafting. The first CP electrodes were prepared by CV technique repeating several cycles in the range of +0.5 V to -0.2 V vs Ag/AgCl. The correct electro-grafting of the CuTAPP complex was firstly monitored simply looking to the electrode (Figure 53), since a strong blue color appears on the surface, and then verified by UV-Vis reflectance spectroscopy. Since the strong color of the porphyrin, once the black electrode is perfectly grafted, a homogeneous blue deposition appears on the electrode, which results indissoluble to organic solvents like methanol, acetone, acetonitrile. Generally, the correct grafting process on CP electrode with voltammetry scan reaching the +0.5 V vs Ag/AgCl resulted to be quite struggling, requiring excessive amount of cycles (around 200) in order to reach an homogeneous deposition. Pushing instead the potential to higher bias like +0.8 V, resulted to be more performant and faster, requiring a smaller amount of cycles and a better coverage. The electrografting process through cyclic voltammetry completely failed once the support was changed from CP to GDL.

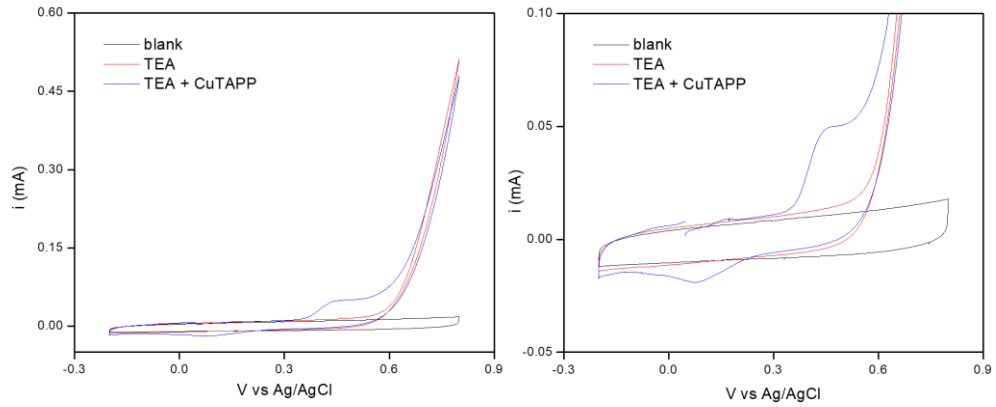

Figure 52: Cyclic Voltammetry of CuTAPP solution (0.5 mM) inside a 0.1 M $LiClO_4$ methanol solution with 25mM TEA base. a) complete cyclic voltammetry, b) magnification.

Further experiments were than performed switching from cyclic voltammetry to chronoamperometry as grafting technique. Indeed, once the chronoamperometry was placed at the correct bias of +0.5 V vs Ag/AgCl inside the same type of solution and setup, a more homogeneous preparation occurs actually reducing the preparation time to few seconds or almost a minute in case of larger electrodes. Chronoamperometry grafting resulted to be more efficient also regarding the substrates, making it possible to actually graft the GDL. The same operational procedure was performed on different substrates as reported in Figure 53, in which

in order a CP, a GDL, a GC and a HOPG electrode were electrochemically grafted by the CuTAPP.

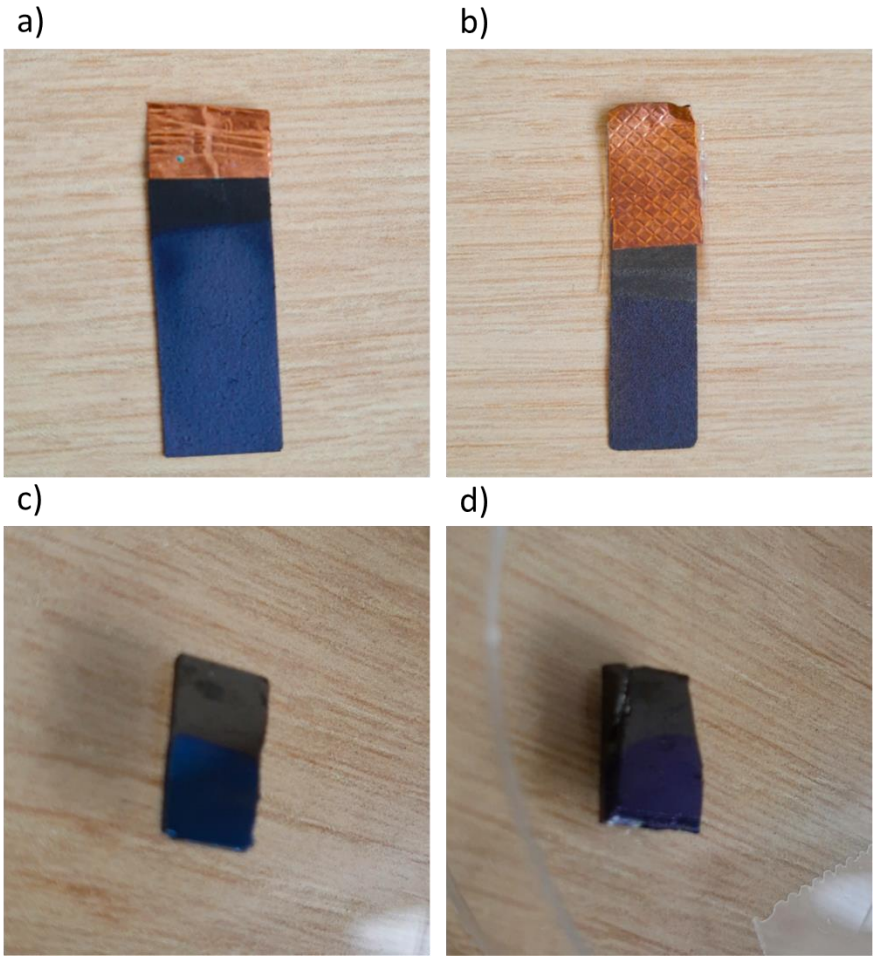

Figure 53: CuTAPP electrografted electrodes. In order, a) CP support, b) GDE support, c) GC support and d) HOPG support.

6.3 Electrochemical performances

The electrochemical performances of the grafted electrodes were deeply investigated with several approaches. Among all the employed supports, only CP and GDL were investigated in the electrolysis setup. In details, the CP was employed in a batch cell configuration, in which the electrode was immersed inside the electrolyte and the CO_2 was also bubbled inside it, while the GDL was tested in

a flow cell reactor in which the CO_2 flow passes backbone the electrode. The first electrochemical investigation of the CuTAPP was in a batch cell configuration in which the catalyst was drop-casted on a GDL electrode.

In Figure 54, the drop casted CuTAPP was tested at different potentials in a 0.1 M $KHCO_3$ electrolyte solution. The reported plot highlights the selectivity towards CO_2RR increases once the bias is pushed to more negative potentials. The highest selectivity is reached at the value of -1.2 V vs RHE, showing a modest overall selectivity around the 50% for CO and $HCOO^-$ products together. This investigation clarifies the optimal potential required for the CO_2RR for the catalyst and furnishes details regarding the possible reachable products spectrum.

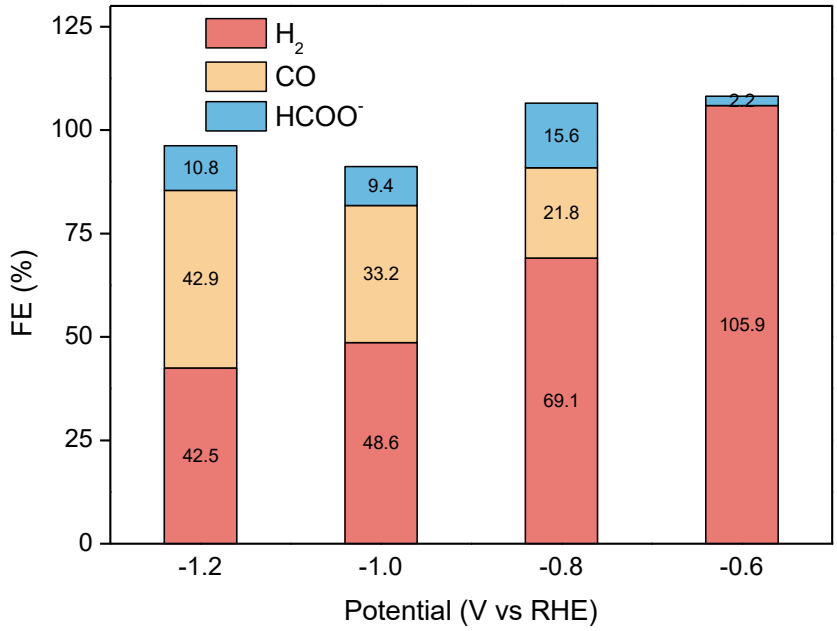

Figure 54: CuTAPP drop casted on a GDL support tested in a flow cell configuration. Chronoamperometry test performed in 0.1 M $KHCO_3$ solution at different potentials.

Once moving from the drop casted electrode to the electrografted one, the electrochemical behavior drastically changes. Three different types of electrode were analyzed: the CuTAPP-CP prepared by cyclic voltammetry, the CuTAPP-CP prepared by chronoamperometry and the CuTAPP-GDL by chronoamperometry. Both the grafted CP types, due to the absence of a hydrophobic layer, were tested in a batch cell configuration immersing the catalyst in the electrolyte. In Figure 55 are reported the FEs and the current densities of the CuTAPP-CP electrodes

prepared by CV tested at -1.2 V vs RHE in different electrolytes. The spectrum of products is wider compared to the one obtained with the drop casted CuTAPP. Indeed, in this case more valuable products like CH_4 and C_2H_4 are obtained and with an interesting concentration.

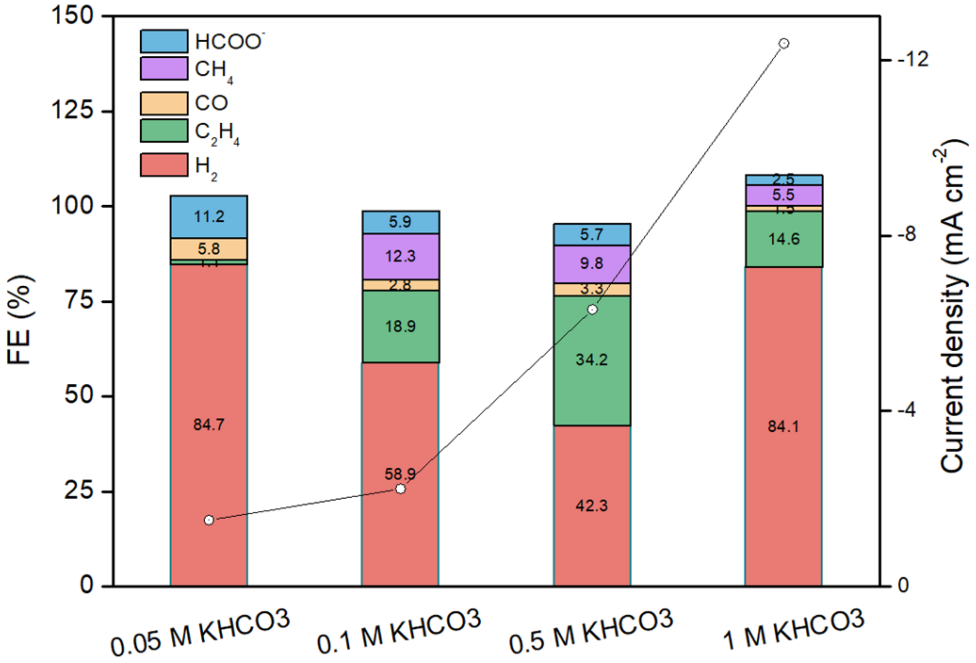

Figure 55: CuTAPP-CP prepared by cyclic voltammetry electrochemical test. Chronoamperometry performed at -1.2 V vs RHE in different electrolyte composition.

The tests reported in Figure 55 are at the same potential, -1.2 V vs RHE, but at different concentrations of $KHCO_3$. The lowest FE for the HER is reached in the 0.5 M electrolyte, interestingly, such value also coincides with the highest amount of hydrogenated products, CH_4 + C_2H_4. Common characteristic of the electrodes prepared by cyclic voltammetry, is their weak stability. Indeed, the ethylene and methane production shows their maximum accumulation in the first 20 minutes of chronoamperometry, then a fast decrease occurs until no more traces of such products were able to be detected. Such test evidences the possible production of interesting products, hydrogenated one, and their electrolyte tuning in order to reach the highest possible FE. Nevertheless it shows a fragile system that could barely work.

In order to improve their stability and performances, the chronoamperometry grafting was then optimized and the same electrochemical

investigation was performed on carbon paper supports. As evidenced in Figure 56**Error! Reference source not found.**, the CP electrodes prepared by chronoamperometry resulted to be again able to produce CH_4 and C_2H_4 products and at the same time be able to continuously produce them all over an hour of experiment without any sort of interruption. Another difference is also the lower rate regarding the CO_2RR at expanse of the HER which inevitably increases. If with the CuTAPP-CP electrodes prepared by cyclic voltammetry, in the first minutes of electrolysis the FE for the HER was of 42.3%, Figure 55, such low amount was not detected at the same condition with the electrodes prepared by chronoamperometry. Indeed, a value around 65% was obtained all over the experiments. Such results make the CuTAPP-CP prepared by chronoamperometry a weaker approach in terms of selectivity, nevertheless a more solid procedure in order to prepare stable catalysts.

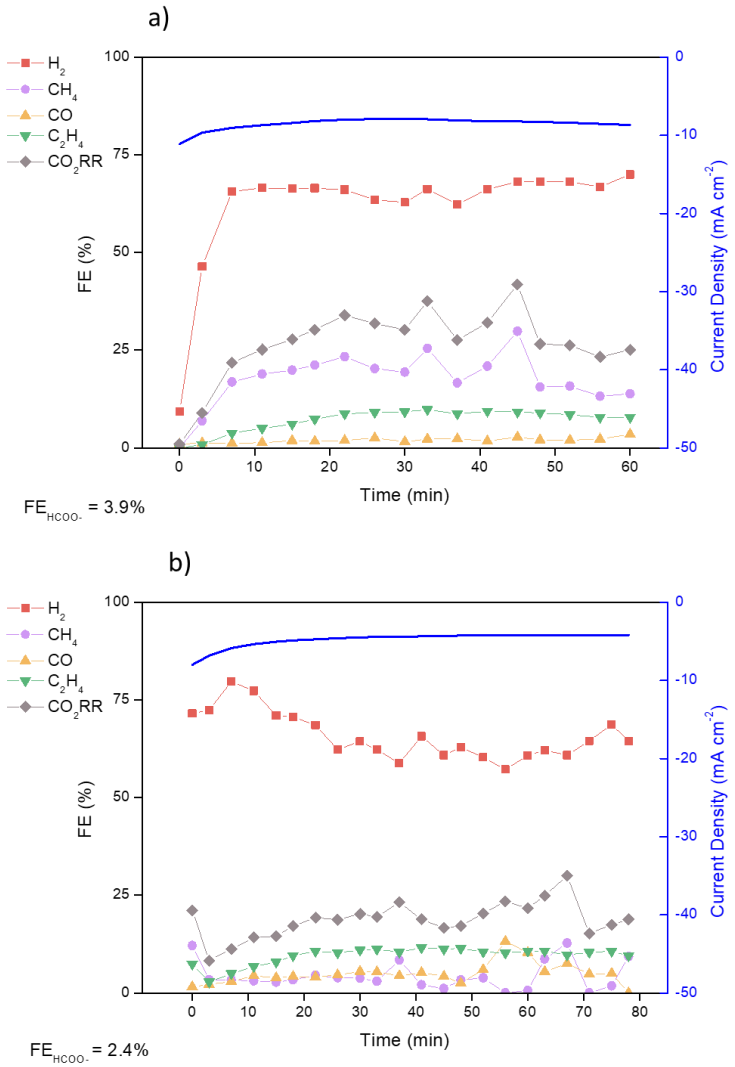

Figure 56: Electrochemical performances of CuTAPP-CP grafted electrodes by chronoamperometry. Electrolysis performed in a batch cell configuration with a 0.5 M $KHCO_3$ electrolyte at a) -1.2 V vs RHE and b) -1.1 V vs RHE.

In order to prepare stable electrodes by chronoamperometry but at the same time to reach higher FE towards the CO_2RR and higher current densities, the electrografting by chronoamperometry on GDL was performed and tested in a flow cell. The setup utilized was a flow cell bearing an anionic exchange membrane, AEM, as working electrode a CuTAPP-GDL and counter a Pt foil. Such experiment, even if conducted in the same cell of the previous chapter, was

performed in a different laboratory during an Erasmus Traineeship in the Université de Paris.

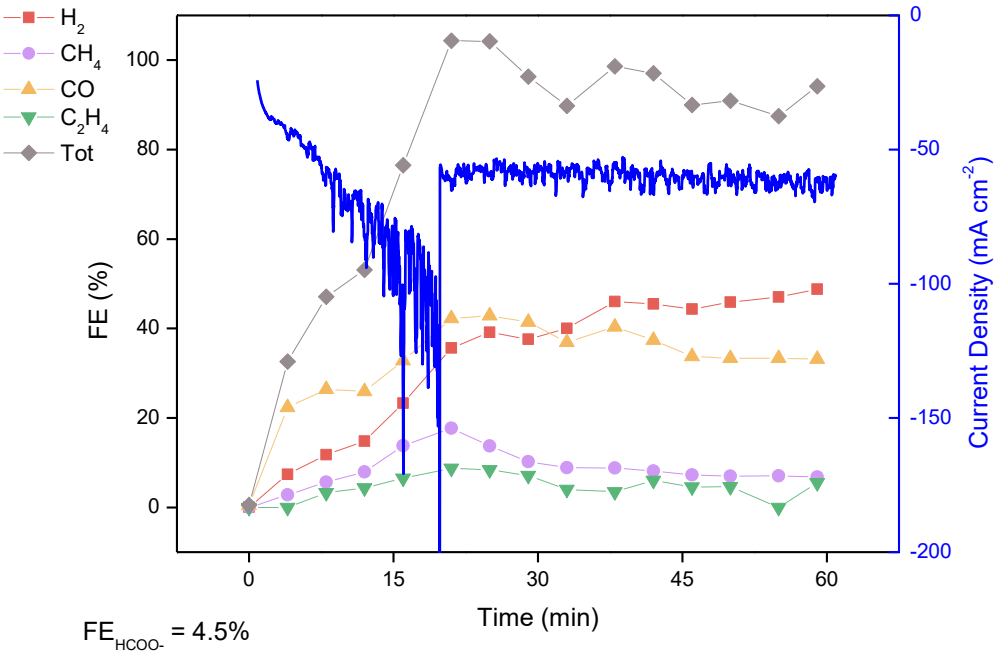

Figure 57: Electrochemical tests in a flow cell configuration of CuTAPP-GDL, 0.5 M $KHCO_3$ at -1.2 V vs RHE, bearing a Sustanion AEM.

In such facility, the ethylene detection was not possible, reason of the missing registration value for such product, even if qualitatively identified. In Figure 57 are reported the electrochemical tests performed in a flow cell setup configuration, both in the optimized potential-electrolyte -1.2 V vs RHE and 0.5 M $KHCO_3$ from previous analysis. In Figure 57a, the electrochemical test bearing a Fumasep AEM is reported. The main variation switching from a batch cell having a PEM to a flow cell bearing an AEM is in a higher current density and an unfortunately lower selectivity towards CH_4 and C_2H_4 products. Indeed, the obtained selectivity toward such products was not able to surpass the low value of 5%.

Such a change in the selectivity of difficult interpretation. The presence of a hydrophobic layer modifies the interaction with the water electrolyte, the interaction instead with the metal complex under potential is a completely different matter. Anyway we can anticipate that the selectivity towards CH_4 and C_2H_4

products comes from the copper clusters formation, thus a minor selectivity of those products it is translated to a minor metal copper formation.

6.4 Ex-situ characterization

The extremely high interest for the hydrogenated products like ethylene and methane pushes the investigation on the catalyst in order to elucidate its actual active site. Indeed, as mentioned in the first chapter, the only species actually known to be able to produce such hydrocarbons by electrochemistry is the metal copper. Since the nature of the metal cation involved in the porphyrin, is possible a de-complexation reaction, promoted by the negative bias, in which the Cu^{2+} ions are actually unbounded to the molecule and can easily be reduced to metal clusters. Once the cyclic voltammetry investigation of the CuTAPP-CP was performed in water solution, no evidence of possible degradation was evidenced. Trying to investigate the catalyst in homogeneous condition, there was no evidence of catalyst de-complexation reaction. In order to evaluate a possible change in the nature of the catalyst, several ex-situ characterizations were repeated on the grafted electrodes once they have performed exhaustive electrolysis under negative bias. Among all the possible characterization techniques, only the FE-SEM and the XPS were able to furnish further information about the possible change in the catalysts.

The first analysis was with the FE-SEM technique on CuTAPP-CP electrodes prepared by cyclic voltammetry, Figure 58. The electrodes of the investigation were tested at -1.2 V vs RHE in a 0.5 M $KHCO_3$, accumulating one hour of electrolysis. Such electrodes prepared by cyclic voltammetry, showed a peculiar behavior. They result highly selective for hydrogenated products like CH_4 and C_2H_4 in the first minutes of electrolysis, nevertheless they eventually stop the hydrocarbons production after this preliminary phase, Figure 54. From FE-SEM images of a tested electrode, it was possible to detect small particles spread all over the catalyst having an extremely small dimension that were not present on the virgin grafted electrode. Such clusters were investigated through the SE2 detector in order to detect copper clusters due to the high Z number of Cu, nevertheless a more intense brightness was not detected. From EDX mapping, there is no evidence of metal clusters since the Cu signal is perfectly distributed all over the electrode, together with the N signal correlated to the porphyrin grafting. Despite a difficult determination, a clear change in the surface morphology occurred.

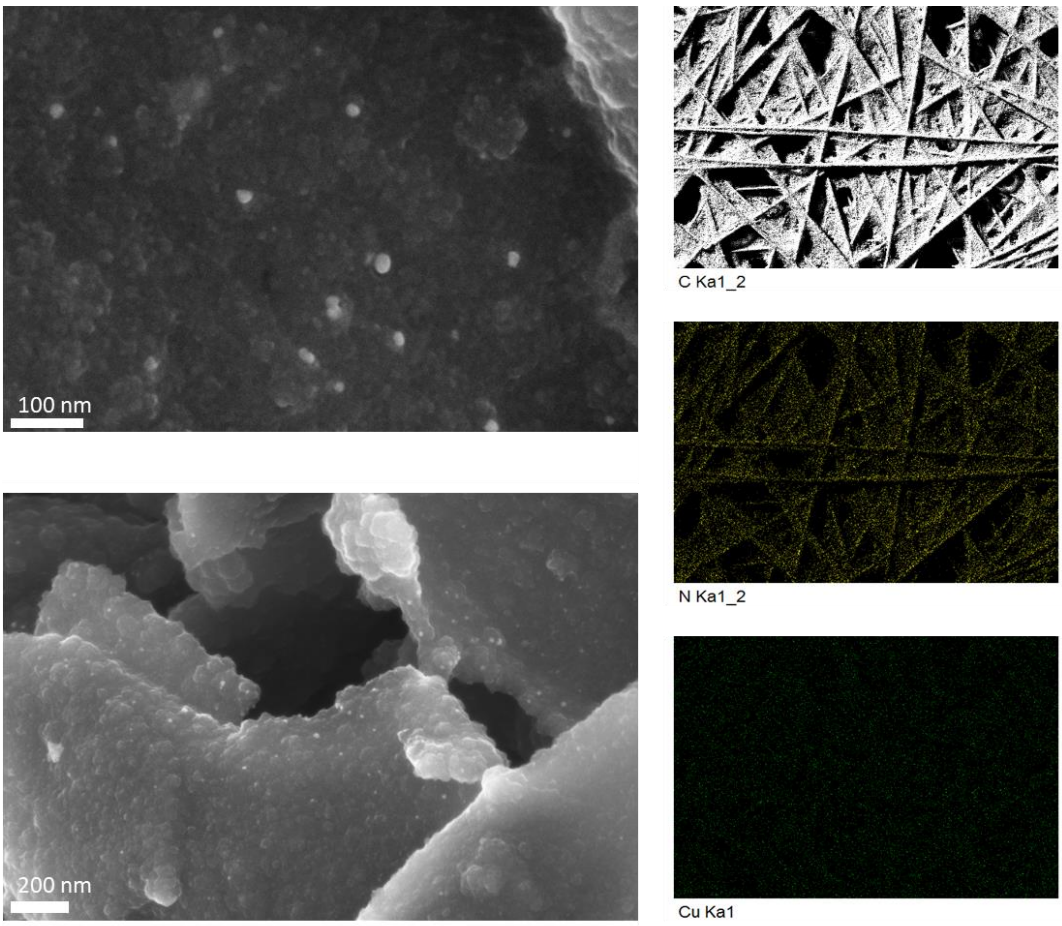

Figure 58: FE-SEM images of the grafted CuTAPP-CP prepared by cyclic voltammetry, tested at -1.2 V vs RHE in 0.5 M$KHCO_3$ for 1 hour.

In Figure 59 are reported a detailed FE-SEM investigation on a CuTAPP-CP electrodes prepared by chronoamperometry. In the left column, Figure 59a,c,e, are reported three different magnifications of the virgin CuTAPP-CP grafted electrode. Instead, in the right column, Figure 59b,d,f, the same magnification of the same electrode after 30 hours of electrolysis at -1.2 V vs RHE in a 0.5M $KHCO_3$ solution are reported. In this case of the grafted CuTAPP-CP by chronoamperometry, a completely different scenario appears. Indeed, once the electrolysis is performed for 30 h, there are no evidence of any morphological changes in electrode. This unpredicted information is someway parallel to the electrochemical behavior, in which the CuTAPP-CP prepared by chronoamperometry does not show any trace of CH_4 and C_2H_4 selectivity loss, thus differing from the one prepared by CV. Such investigations do not clarify what is

the active site of the catalysis, it furnishes only evidence that the two procedures for the electrografting are different on the same substrate, and highlights the benefits of the latter.

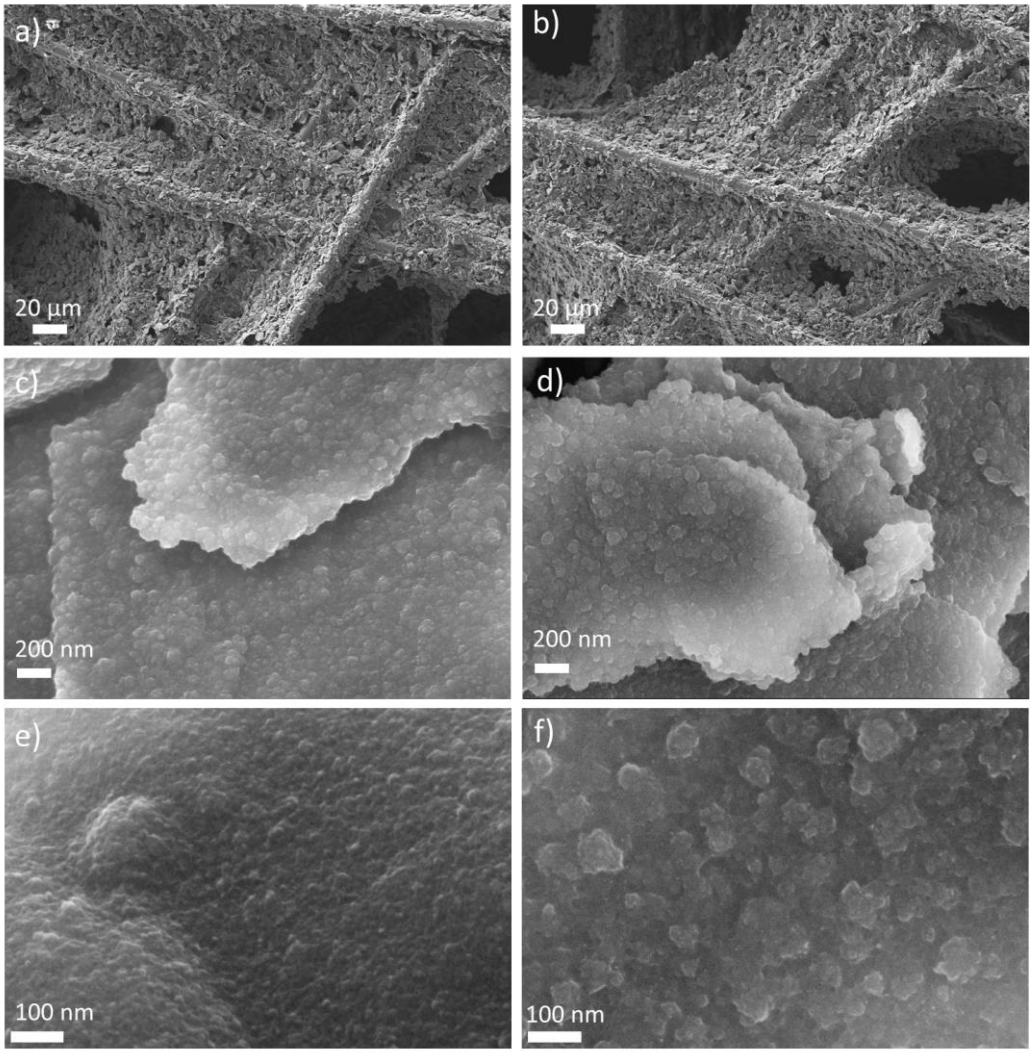

Figure 59: FE-SEM images of a CuTAPP-CP grafted electrode. Three different magnifications a-b, c-d and e-f, with virgin electrode on the left column and tested electrode after 30 h of electrolysis on the right column.

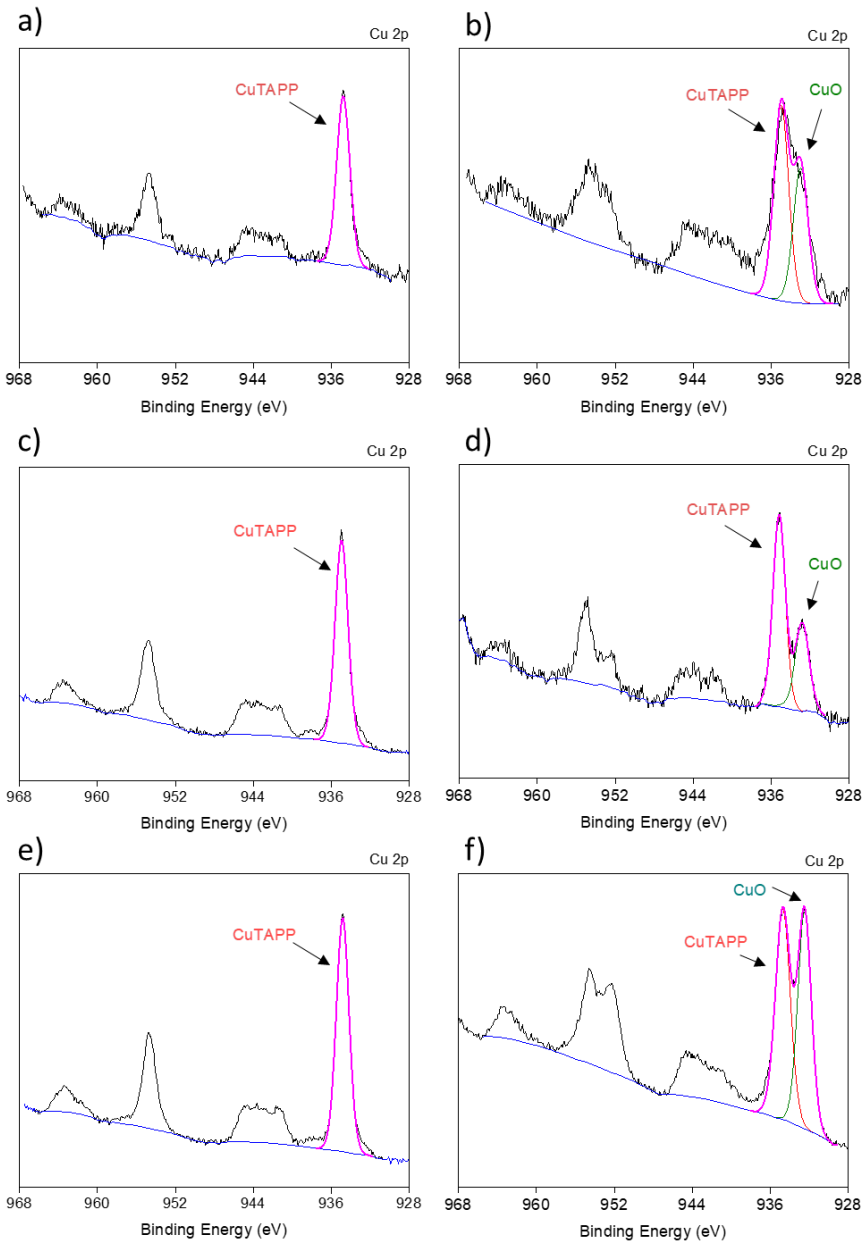

Figure 60: XPS measurements on a) and b) CuTAPP-CP, c) and d) CuTAPP-GC, e) and f) CuTAPP-HOPG. Left column, virgin electrodes priory chronoamperometry, right column tested electrodes after 30h of test.

The technique able to furnish the main ex-situ information is the XPS. Indeed, by analyzing the copper signals of the virgin electrodes, it is possible to identify the absorption pattern of the molecular copper complex and distinguish it from the ones obtained for Cu, CuO, Cu_2O and $Cu(OH)_2$. In Figure 60 are reported the Cu 2p

signals of the grafted electrodes. The left column shows the virgin samples, in the right column are the tested electrodes, i.e. re-analyzed after the electrolysis.

In Figure 60a and b, the spectra of the CuTAPP-CP prepared by chronoamperometry and the same sample re-analyzed after 30h of electrolysis are reported. From this comparison, a minor modification of the Cu $2p_{3/2}$ contribution is detachable. Since the three-dimensional nature of the CP support, composed of multilayer carbon species, its analysis can be difficult and a clear information is difficult to extrapolate since the low resolution of the Cu 2p peak.

Table 7: Cu 2p3/2 binding energy, Cu L3M4,5M4,5 kinetic energy, Auger Parameter (α') of reference materials (a)[101] and of the electrografted samples CuTAPP-CP, CuTAPP-GC, CuTAPP-HOPG after test.

Compound	Cu $2p_{3/2}$ peak maximum E_b (eV)	Cu LMM Auger peak maximum E_k (eV)	Auger Parameter (eV)
[a]Cu	932.6	918.6	1851.2
[a]Cu_2O	932.2	917.0	1849.2
[a]CuO	933.8	917.6	1851.3
[a]$Cu(OH)_2$	934.7	916.3	1850.9
CuTAPP-CP	933.0	915.0	1847.95
CuTAPP-GC	932.8	914.7	1847.52
CuTAPP-HOPG	932.5	916.3	1848.76

In order to clarify the stability of the catalyst, more ordered and flat surfaces like the GC and the HOPG were electrografted, tested and analyzed. A definitely more clear spectra is indeed obtained for GC (Figure 60c,d) and even more for HOPG (Figure 60e,f) supports. In both these electrodes, once the electrolysis is performed, there is an important splitting of the copper pattern; an information present also for the CP even if less clear. On this supports, the copper signal is clearly associable with the presence of both the Cu-porphyrin and a secondary inorganic form of copper. Analyzing the values of Cu 2p listed in the Table 7, a possible match is present with the metallic copper and its Cu^{2+} oxide. In order to discriminate between these two contributes, the Cu LMM signal must be taken in consideration. Nevertheless, being the Auger transition the superimposition of both the CuTAPP species and of the Cu/CuO compounds, the Cu LMM signals is of

difficult estimation, not allowing further clarification. It can be hypothesized anyway that metal clusters agglomeration occurs under negative potential and, due to the extremely low size of the particles, their oxidation occurs once the bias is stopped and the sample is exposed to the air. Such hypothesis is of very recent discussion, as reported in recent publications of well-known journals[158,159].

Putting aside the discrimination between the Cu/CuO formation, the ex situ analysis furnishes a more important information on the stability of the CuTAPP under potential. The main hypothesis is that the Cu^{2+}-porphyrin is not stable under such reducing bias, thus partially freeing the Cu^{2+} cations which are reduced to form metal clusters. The metal copper is the main active species for the hydrocarbons formation recorded during the electrolysis, perfectly matching the previously literacture[55,63,160,161]. A proper investigation should be performed through in-situ technique, thus actually analyzing the copper signal meanwhile the bias is imposed.

Such investigation highlights of course a drawback regarding the molecular complex, actually defining as unstable and not being the active species of the products of more interest. Nevertheless, shows also how an electrografting approach is a possible strategy to actually introduce an extremely low amount of metal resources on the electrode and still reach a great selectivity. Taking in consideration this aspect, several more stable porphyrins are known and even unstable complexes could be of interest in order to actually produce metal clusters of extremely low size.

Chapter 7

Conclusions

In all the previous chapters, several approaches in order to obtain stable single metal centers were investigated. The proposed catalysts, deeply varying in their chemical composition, have as the only common aspect the idea to introduce metal atoms in form of cations in the structure of the material. The chosen strategies were variegated, as dopants in the case of doped polyaniline, as metal oxide in the case of binary SnO_2/PANI material, as direct building block in the case of MOF, in which the metal center specifically builds the entire material coordinating organic ligands, and finally as metallorganic complex once the metal porphyrin was studied and functionalized on carbon supports.

Together with the physical and chemical investigations around these catalysts, the electrochemical characterization was also optimized. Indeed, in the former parts of work, a batch cell setup was employed, resulting in low performances and reachable FEs. Subsequently, the introduction of flow cell completely improved the investigation. The catalysts were able to produce a higher rate of CO_2RR overwhelming the requirement of the dissolved CO_2 and working instead directly with its gas phase. This is translated in better FEs and higher geometric current densities. The introduction of flow cell makes it possible also the study of different concentrations of electrolytes, permitting stability tests of several hours until the longest investigated time of few days.

Considering the typology of required process and the nature of the experiment, the strategy to investigate catalysts based on organic species resulted a limited approach. Inevitably, the requirement of a highly conductive material makes the competition between the more canonical benchmark metallic species and the organic ones unbalanced. Even if underlying the interest of a more strategic employment of metallic resources, the nonconductive nature of the organic species is often an obstacle for the overall performance. Nevertheless, this does not discourage that type of research, rather than more solid and advanced strategies must be applied in order to reach performances of interest. The case of the electrografted porphyrin is a good example. A nonconductive drop-casted catalyst

limits the great conductivity of the carbon-based support above, although, once the strategy of mere deposition switches to the more advanced electrografting, an extremely thin film is present on the support, almost nonvisible by SEM. Such layer does not induce a lower conductivity due to the extremely low deposition, as a consequence the material showed great performances of current density once a bias was applied.

Analyzing the CO_2RR theme in general instead, the progresses in this field are encouraging and at the same time not excelling. The knowledge and the performances are rapidly growing, thus making obsolete the research papers in short time. Nevertheless, the combination of the costs, the performances, the lifetime and the problems regarding the scale up still makes the technology deeply limited. A lot of knowledge is still missing and being in study, actually limiting the possible curve of progress for the technology. In situ characterizations are becoming more popular, actually clarifying all the transformation inside the materials once under bias and during the catalysis, thus helping the possible optimization and modelling steps for future works.

Further efforts will be focused both on the setup employed and the materials, maintaining the idea of single metal active site solution. More ambitious studies will be also followed trying to investigate molecular compounds, metal free, able to perform the CO_2RR without the presence of an actual metal center.

Bibliography

(1) Todorova, T. K.; Schreiber, M. W.; Fontecave, M. Mechanistic Understanding of CO2 Reduction Reaction (CO2RR) Toward Multicarbon Products by Heterogeneous Copper-Based Catalysts. *ACS Catal.* **2020**, *10* (3), 1754–1768. https://doi.org/10.1021/acscatal.9b04746.

(2) Ghosh, D.; Kumar, G. R.; Subramanian, S.; Tanaka, K. More Than Just a Reagent: The Rise of Renewable Organohydrides for Catalytic Reduction of Carbon Dioxide. *ChemSusChem* **2020**, 824–841. https://doi.org/10.1002/cssc.202002660.

(3) Cheng, Y.; Yang, S.; Jiang, S. P.; Wang, S. Supported Single Atoms as New Class of Catalysts for Electrochemical Reduction of Carbon Dioxide. *Small Methods* **2019**, *3* (9), 1–16. https://doi.org/10.1002/smtd.201800440.

(4) Siemenski, A. Technology Readiness and Costs of CCS The Circular Carbon Economy. *J. Combust. Soc. Japan* **2021**, No. March.

(5) Murdoch, K.; Smith, F.; Perry, J.; Green, S. Assessment of Technology Readiness Level of a Carbon Dioxide Reduction Assembly (CRA) for Use on International Space Station. *SAE Tech. Pap.* **2004**, No. 724. https://doi.org/10.4271/2004-01-2446.

(6) Zhang, G.; Wang, Z.; Wu, J. Construction of a Z-Scheme Heterojunction for High-Efficiency Visible-Light-Driven Photocatalytic CO2reduction. *Nanoscale* **2021**, *13* (8), 4359–4389. https://doi.org/10.1039/d0nr08442e.

(7) Li, X.; Wen, J.; Low, J.; Fang, Y.; Yu, J. *Design and Fabrication of Semiconductor Photocatalyst for Photocatalytic Reduction of CO2 to Solar Fuel*; 2014; Vol. 57. https://doi.org/10.1007/s40843-014-0003-1.

(8) Zhang, W.; Hu, Y.; Ma, L.; Zhu, G.; Wang, Y.; Xue, X.; Chen, R.; Yang, S.; Jin, Z. Progress and Perspective of Electrocatalytic CO2 Reduction for Renewable Carbonaceous Fuels and Chemicals. *Adv. Sci.* **2018**, *5* (1). https://doi.org/10.1002/advs.201700275.

(9) Benson, E. E.; Kubiak, C. P.; Sathrum, A. J.; Smieja, J. M. Electrocatalytic and Homogeneous Approaches to Conversion of CO2 to Liquid Fuels. *Chem. Soc. Rev.* **2009**, *38* (1), 89–99. https://doi.org/10.1039/b804323j.

(10) Bard, A. J.; Parsons, R.; Jordan, J. *Standard Potentials in Aqueous Solution*; Routledge, 2017; Vol. 7. https://doi.org/10.1201/9780203738764.

(11) Lukoyanov, D.; Barney, B. M.; Dean, D. R.; Seefeldt, L. C.; Hoffman, B. M. Connecting Nitrogenase Intermediates with the Kinetic Scheme for N 2 Reduction by a Relaxation Protocol and Identification of the N 2 Binding State. *Proc. Natl. Acad. Sci. U. S. A.* **2007**, *104* (5), 1451–1455. https://doi.org/10.1073/pnas.0610975104.

(12) Yoo, S. J.; Angove, H. C.; Papaefthymiou, V.; Burgess, B. K.; Münck, E. Mossbauer Study of the MoFe Protein of Nitrogenase from Azotobacter Vinelandii Using Selective 57Fe Enrichment of the M-Centers. *J. Am. Chem. Soc.* **2000**, *122* (20), 4926–4936. https://doi.org/10.1021/ja000254k.

(13) Barney, B. M.; Lee, H. I.; Dos Santos, P. C.; Hoffman, B. M.; Dean, D. R.; Seefeldt, L. C. Breaking the N 2 Triple Bond: Insights into the Nitrogenase Mechanism. *Dalt. Trans.* **2006**, No. 19, 2277–2284. https://doi.org/10.1039/b517633f.

(14) Hoffman, B. M.; Lukoyanov, D.; Yang, Z. Y.; Dean, D. R.; Seefeldt, L. C. Mechanism of Nitrogen Fixation by Nitrogenase: The next Stage. *Chem. Rev.* **2014**, *114* (8), 4041–4062. https://doi.org/10.1021/cr400641x.

(15) Garza, A. J.; Bell, A. T.; Head-Gordon, M. Mechanism of CO2 Reduction at Copper Surfaces: Pathways to C2 Products. *ACS Catal.* **2018**, *8* (2), 1490–1499. https://doi.org/10.1021/acscatal.7b03477.

(16) Singh, M. R.; Clark, E. L.; Bell, A. T. Effects of Electrolyte, Catalyst, and Membrane Composition and Operating Conditions on the Performance of Solar-Driven Electrochemical Reduction of Carbon Dioxide. *Phys. Chem. Chem. Phys.* **2015**, *17* (29), 18924–18936. https://doi.org/10.1039/c5cp03283k.

(17) De Jesus Gálvez-Vázquez, M.; Moreno-García, P.; Xu, H.; Hou, Y.; Hu, H.; Montiel, I. Z.; Rudnev, A. V.; Alinejad, S.; Grozovski, V.; Wiley, B. J.; Arenz, M.; Broekmann, P.; Moreno-García, P. Environment Matters: CO2RR Electrocatalyst Performance Testing in a Gas-Fed Zero-Gap Electrolyzer. *ACS Catal.* **2020**, *10* (21), 13096–13108. https://doi.org/10.1021/acscatal.0c03609.

(18) Lees, E. W.; Mowbray, B. A. W.; Parlane, F. G. L.; Berlinguette, C. P. Gas Diffusion Electrodes and Membranes for CO2 Reduction Electrolysers. *Nature Reviews Materials*. Nature Publishing Group September 17, 2021, pp 1–10. https://doi.org/10.1038/s41578-021-00356-2.

(19) Saeki, T.; Hashimoto, K.; Kimura, N.; Omata, K.; Fujishima, A. Electrochemical Reduction of CO2 with High Current Density in a CO2 + Methanol Medium II. CO Formation Promoted by Tetrabutylammonium Cation. *J. Electroanal. Chem.* **1995**, *390* (1–2), 77–82. https://doi.org/10.1016/0022-0728(95)03897-P.

(20) Saeki, T.; Hashimoto, K.; Fujishima, A.; Kimura, N.; Omata, K. Electrochemical Reduction of CO2 with High Current Density in a CO2-Methanol Medium. *J. Phys. Chem.* **1995**, *99* (20), 8440–8446. https://doi.org/10.1021/j100020a083.

(21) Li, J.; Prentice, G. Electrochemical Synthesis of Methanol from CO 2 in High-Pressure Electrolyte. *J. Electrochem. Soc.* **1997**, *144* (12), 4284–4288. https://doi.org/10.1149/1.1838179.

(22) Bartlett, P. N.; Cook, D. C.; George, M. W.; Ke, J.; Levason, W.; Reid, G.; Su, W.; Zhang, W. Phase Behaviour and Conductivity Study on Multi-Component Mixtures for Electrodeposition in Supercritical Fluids. *Phys. Chem. Chem. Phys.* **2010**, *12* (2), 492–501. https://doi.org/10.1039/b918981e.

(23) Melchaeva, O.; Voyame, P.; Bassetto, V. C.; Prokein, M.; Renner, M.; Weidner, E.; Petermann, M.; Battistel, A. Electrochemical Reduction of Protic Supercritical CO2 on Copper Electrodes. *ChemSusChem* **2017**, *10* (18), 3660–3670. https://doi.org/10.1002/cssc.201701205.

(24) König, M.; Vaes, J.; Klemm, E.; Pant, D. Solvents and Supporting Electrolytes in the Electrocatalytic Reduction of CO2. *iScience* **2019**, *19*, 135–160. https://doi.org/10.1016/j.isci.2019.07.014.

(25) Oh, Y.; Vrubel, H.; Guidoux, S.; Hu, X. Electrochemical Reduction of CO2 in Organic Solvents Catalyzed by MoO2. *Chem. Commun.* **2014**, *50* (29), 3878–3881. https://doi.org/10.1039/c3cc49262a.

(26) Tomita, Y.; Teruya, S.; Koga, O.; Hori, Y. Electrochemical Reduction of Carbon Dioxide at a Platinum Electrode in Acetonitrile-Water Mixtures. *J. Electrochem. Soc.* **2000**, *147* (11), 4164. https://doi.org/10.1149/1.1394035.

(27) Rosen, B. A.; Salehi-Khojin, A.; Thorson, M. R.; Zhu, W.; Whipple, D. T.; Kenis, P. J. A.; Masel, R. I. Ionic Liquid-Mediated Selective Conversion of CO2 to CO at Low Overpotentials. *Science (80-.).* **2011**, *334* (6056), 643–644. https://doi.org/10.1126/science.1209786.

(28) Atifi, A.; Boyce, D. W.; Dimeglio, J. L.; Rosenthal, J. Directing the Outcome

of CO2 Reduction at Bismuth Cathodes Using Varied Ionic Liquid Promoters. *ACS Catal.* **2018**, *8* (4), 2857–2863. https://doi.org/10.1021/acscatal.7b03433.

(29) Sun, L.; Ramesha, G. K.; Kamat, P. V.; Brennecke, J. F. Switching the Reaction Course of Electrochemical CO2 Reduction with Ionic Liquids. *Langmuir* **2014**, *30* (21), 6302–6308. https://doi.org/10.1021/la5009076.

(30) Rudnev, A. V.; Zhumaev, U. E.; Kuzume, A.; Vesztergom, S.; Furrer, J.; Broekmann, P.; Wandlowski, T. The Promoting Effect of Water on the Electroreduction of CO2 in Acetonitrile. *Electrochim. Acta* **2016**, *189*, 38–44. https://doi.org/10.1016/j.electacta.2015.12.088.

(31) Gonella, G.; Backus, E. H. G.; Nagata, Y.; Bonthuis, D. J.; Loche, P.; Schlaich, A.; Netz, R. R.; Kühnle, A.; McCrum, I. T.; Koper, M. T. M.; Wolf, M.; Winter, B.; Meijer, G.; Campen, R. K.; Bonn, M. Water at Charged Interfaces. *Nat. Rev. Chem.* **2021**, *0123456789*. https://doi.org/10.1038/s41570-021-00293-2.

(32) Huang, J. E.; Li, F.; Ozden, A.; Rasouli, A. S.; de Arquer, F. P. G.; Liu, S.; Zhang, S.; Luo, M.; Wang, X.; Lum, Y.; Xu, Y.; Bertens, K.; Miao, R. K.; Dinh, C. T.; Sinton, D.; Sargent, E. H. CO2 Electrolysis to Multicarbon Products in Strong Acid. *Science (80-.).* **2021**, *372* (6546), 1074–1078. https://doi.org/10.1126/science.abg6582.

(33) Hernandez-Aldave, S.; Andreoli, E. Fundamentals of Gas Diffusion Electrodes and Electrolysers for Carbon Dioxide Utilisation: Challenges and Opportunities. *Catalysts* **2020**, *10* (6), 1–34. https://doi.org/10.3390/CATAL10060713.

(34) Tung, S. P.; Hwang, B. J. Synthesis and Characterization of Hydrated Phosphor-Silicate Glass Membrane Prepared by an Accelerated Sol-Gel Process with Water/Rapor Management. *J. Mater. Chem.* **2005**, *15* (34), 3532–3538. https://doi.org/10.1039/b505918f.

(35) Ma, D.; Jin, T.; Xie, K.; Huang, H. An Overview of Flow Cell Architecture Design and Optimization for Electrochemical CO2reduction. *J. Mater. Chem. A* **2021**, *9* (37), 20897–20918. https://doi.org/10.1039/d1ta06101a.

(36) Pärnamäe, R.; Mareev, S.; Nikonenko, V.; Melnikov, S.; Sheldeshov, N.; Zabolotskii, V.; Hamelers, H. V. M.; Tedesco, M. Bipolar Membranes: A Review on Principles, Latest Developments, and Applications. *J. Memb. Sci.* **2021**, *617*. https://doi.org/10.1016/j.memsci.2020.118538.

(37) Shi, S.; Pan, Y.; Lu, B.; Shen, C.; Zheng, G.; Liu, C. Preparation and

Characterization of a Bipolar Membrane Modified by Copper Phthalocyanine 16-Carboxylic Acid and Acetyl Ferrocene. *J. Macromol. Sci. Part B Phys.* **2014**, *53* (8), 1431–1441. https://doi.org/10.1080/00222348.2014.910047.

(38) Wang, A.; Peng, S.; Wu, Y.; Huang, C.; Xu, T. A Hybrid Bipolar Membrane. *J. Memb. Sci.* **2010**, *365* (1–2), 269–275. https://doi.org/10.1016/j.memsci.2010.09.016.

(39) Chen, R. Y.; Chen, Z.; Zheng, X.; Chen, X.; Wu, S. Y. Preparation and Characterization of MSA/MCS Bipolar Membranes Modified by CuTsPc and CuTAPc. *J. Memb. Sci.* **2010**, *355* (1–2), 1–6. https://doi.org/10.1016/j.memsci.2010.01.013.

(40) Rajesh, A. M.; Kumar, M.; Shahi, V. K. Functionalized Biopolymer Based Bipolar Membrane with Poly Ethylene Glycol Interfacial Layer for Improved Water Splitting. *J. Memb. Sci.* **2011**, *372* (1–2), 249–257. https://doi.org/10.1016/j.memsci.2011.02.009.

(41) Tepzz, T. Cationic-Anionic Ion-Exchange Membrane, 2019.

(42) Kumar, M.; Shahi, V. K. Heterogeneous-Homogeneous Composite Bipolar Membrane for the Conversion of Salt of Homologous Carboxylates into Their Corresponding Acids and Bases. *J. Memb. Sci.* **2010**, *349* (1–2), 130–137. https://doi.org/10.1016/j.memsci.2009.11.041.

(43) Vogel, C.; Meier-Haack, J. Preparation of Ion-Exchange Materials and Membranes. *Desalination* **2014**, *342*, 156–174. https://doi.org/10.1016/j.desal.2013.12.039.

(44) Lees, E. W.; Mowbray, B. A. W.; Parlane, F. G. L.; Berlinguette, C. P. Gas Diffusion Electrodes and Membranes for CO2 Reduction Electrolysers. *Nat. Rev. Mater.* **2021**, *0123456789*. https://doi.org/10.1038/s41578-021-00356-2.

(45) Tan, X.; Yu, C.; Ren, Y.; Cui, S.; Li, W.; Qiu, J. Recent Advances in Innovative Strategies for the CO2electroreduction Reaction. *Energy Environ. Sci.* **2021**, *14* (2), 765–780. https://doi.org/10.1039/d0ee02981e.

(46) Ripatti, D. S.; Veltman, T. R.; Kanan, M. W. Carbon Monoxide Gas Diffusion Electrolysis That Produces Concentrated C2 Products with High Single-Pass Conversion. *Joule* **2019**, *3* (1), 240–256. https://doi.org/10.1016/j.joule.2018.10.007.

(47) Rabinowitz, J. A.; Kanan, M. W. The Future of Low-Temperature Carbon Dioxide Electrolysis Depends on Solving One Basic Problem. *Nat. Commun.* **2020**, *11* (1), 10–12. https://doi.org/10.1038/s41467-020-19135-8.

(48) Jeng, E.; Jiao, F. Investigation of CO2single-Pass Conversion in a Flow Electrolyzer. *React. Chem. Eng.* **2020**, *5* (9), 1768–1775. https://doi.org/10.1039/d0re00261e.

(49) Bhargava, S. S.; Proietto, F.; Azmoodeh, D.; Cofell, E. R.; Henckel, D. A.; Verma, S.; Brooks, C. J.; Gewirth, A. A.; Kenis, P. J. A. Cover Feature: System Design Rules for Intensifying the Electrochemical Reduction of CO 2 to CO on Ag Nanoparticles (ChemElectroChem 9/2020) . *ChemElectroChem* **2020**, *7* (9), 1953–1953. https://doi.org/10.1002/celc.202000448.

(50) Jeanty, P.; Scherer, C.; Magori, E.; Wiesner-Fleischer, K.; Hinrichsen, O.; Fleischer, M. Upscaling and Continuous Operation of Electrochemical CO2 to CO Conversion in Aqueous Solutions on Silver Gas Diffusion Electrodes. *J. CO2 Util.* **2018**, *24* (November 2017), 454–462. https://doi.org/10.1016/j.jcou.2018.01.011.

(51) García de Arquer, F. P.; Dinh, C. T.; Ozden, A.; Wicks, J.; McCallum, C.; Kirmani, A. R.; Nam, D. H.; Gabardo, C.; Seifitokaldani, A.; Wang, X.; Li, Y. C.; Li, F.; Edwards, J.; Richter, L. J.; Thorpe, S. J.; Sinton, D.; Sargent, E. H. CO2 Electrolysis to Multicarbon Products at Activities Greater than 1 A Cm−2. *Science (80-.).* **2020**, *367* (6478), 661–666. https://doi.org/10.1126/science.aay4217.

(52) Dinh, C. T.; Burdyny, T.; Kibria, G.; Seifitokaldani, A.; Gabardo, C. M.; Pelayo García De Arquer, F.; Kiani, A.; Edwards, J. P.; De Luna, P.; Bushuyev, O. S.; Zou, C.; Quintero-Bermudez, R.; Pang, Y.; Sinton, D.; Sargent, E. H. CO2 Electroreduction to Ethylene via Hydroxide-Mediated Copper Catalysis at an Abrupt Interface. *Science (80-.).* **2018**, *360* (6390), 783–787. https://doi.org/10.1126/science.aas9100.

(53) Wang, X.; de Araújo, J. F.; Ju, W.; Bagger, A.; Schmies, H.; Kühl, S.; Rossmeisl, J.; Strasser, P. Mechanistic Reaction Pathways of Enhanced Ethylene Yields during Electroreduction of CO2–CO Co-Feeds on Cu and Cu-Tandem Electrocatalysts. *Nat. Nanotechnol.* **2019**, *14* (11), 1063–1070. https://doi.org/10.1038/s41565-019-0551-6.

(54) Li, J.; Chen, G.; Zhu, Y.; Liang, Z.; Pei, A.; Wu, C. L.; Wang, H.; Lee, H. R.; Liu, K.; Chu, S.; Cui, Y. Efficient Electrocatalytic CO2 Reduction on a Three-Phase Interface. *Nat. Catal.* **2018**, *1* (8), 592–600. https://doi.org/10.1038/s41929-018-0108-3.

(55) Nitopi, S.; Bertheussen, E.; Scott, S. B.; Liu, X.; Engstfeld, A. K.; Horch, S.; Seger, B.; Stephens, I. E. L.; Chan, K.; Hahn, C.; Nørskov, J. K.; Jaramillo, T. F.; Chorkendorff, I. Progress and Perspectives of Electrochemical CO2 Reduction on Copper in Aqueous Electrolyte. *Chem. Rev.* **2019**, *119* (12), 7610–7672. https://doi.org/10.1021/acs.chemrev.8b00705.

(56) Kutana, A.; Giapis, K. P. Atomistic Simulations of Electrowetting in Carbon Nanotubes. *Nano Lett.* **2006**, *6* (4), 656–661. https://doi.org/10.1021/nl052393b.

(57) Lomax, D. J.; Kant, P.; Williams, A. T.; Patten, H. V.; Zou, Y.; Juel, A.; Dryfe, R. A. W. Ultra-Low Voltage Electrowetting Using Graphite Surfaces. *Soft Matter* **2016**, *12* (42), 8798–8804. https://doi.org/10.1039/c6sm01565d.

(58) Weng, L. C.; Bell, A. T.; Weber, A. Z. Modeling Gas-Diffusion Electrodes for CO2 Reduction. *Phys. Chem. Chem. Phys.* **2018**, *20* (25), 16973–16984. https://doi.org/10.1039/c8cp01319e.

(59) Santamaria, A. D.; Das, P. K.; MacDonald, J. C.; Weber, A. Z. Liquid-Water Interactions with Gas-Diffusion-Layer Surfaces. *J. Electrochem. Soc.* **2014**, *161* (12), F1184–F1193. https://doi.org/10.1149/2.0321412jes.

(60) Wang, Q.; Dong, H.; Yu, H.; Yu, H. Enhanced Performance of Gas Diffusion Electrode for Electrochemical Reduction of Carbon Dioxide to Formate by Adding Polytetrafluoroethylene into Catalyst Layer. *J. Power Sources* **2015**, *279*, 1–5. https://doi.org/10.1016/j.jpowsour.2014.12.118.

(61) Sassone, D.; Zeng, J.; Fontana, M.; Sacco, A.; Farkhondehfal, M. A.; Periolatto, M.; Pirri, C. F.; Bocchini, S. Polymer-Metal Complexes as Emerging Catalysts for Electrochemical Reduction of Carbon Dioxide. *J. Appl. Electrochem.* **2021**, *51* (9), 1301–1311. https://doi.org/10.1007/s10800-021-01585-7.

(62) Haas, T.; Krause, R.; Weber, R.; Demler, M.; Schmid, G. Technical Photosynthesis Involving CO2 Electrolysis and Fermentation. *Nat. Catal.* **2018**, *1* (1), 32–39. https://doi.org/10.1038/s41929-017-0005-1.

(63) Ma, W.; Xie, S.; Liu, T.; Fan, Q.; Ye, J.; Sun, F.; Jiang, Z.; Zhang, Q.; Cheng, J.; Wang, Y. Electrocatalytic Reduction of CO2 to Ethylene and Ethanol through Hydrogen-Assisted C–C Coupling over Fluorine-Modified Copper. *Nat. Catal.* **2020**, *3* (6), 478–487. https://doi.org/10.1038/s41929-020-0450-0.

(64) Verma, S.; Hamasaki, Y.; Kim, C.; Huang, W.; Lu, S.; Jhong, H. R. M.;

Gewirth, A. A.; Fujigaya, T.; Nakashima, N.; Kenis, P. J. A. Insights into the Low Overpotential Electroreduction of CO2 to CO on a Supported Gold Catalyst in an Alkaline Flow Electrolyzer. *ACS Energy Lett.* **2018**, *3* (1), 193–198. https://doi.org/10.1021/acsenergylett.7b01096.

(65) Endrődi, B.; Samu, A.; Kecsenovity, E.; Halmágyi, T.; Sebők, D.; Janáky, C. Operando Cathode Activation with Alkali Metal Cations for High Current Density Operation of Water-Fed Zero-Gap Carbon Dioxide Electrolysers. *Nat. Energy* **2021**, *6* (4), 439–448. https://doi.org/10.1038/s41560-021-00813-w.

(66) Gao, D.; Wei, P.; Li, H.; Lin, L.; Wang, G.; Bao, X. Designing Electrolyzers for Electrocatalytic Co2 Reduction. *Wuli Huaxue Xuebao/ Acta Phys. -Chim. Sin.* **2021**, *37* (5). https://doi.org/10.3866/PKU.WHXB202009021.

(67) Therdthianwong, A.; Manomayidthikarn, P.; Therdthianwong, S. Investigation of Membrane Electrode Assembly (MEA) Hot-Pressing Parameters for Proton Exchange Membrane Fuel Cell. *Energy* **2007**, *32* (12), 2401–2411. https://doi.org/10.1016/j.energy.2007.07.005.

(68) Fujinuma, N.; Ikoma, A.; Lofland, S. E. Highly Efficient Electrochemical CO2 Reduction Reaction to CO with One-Pot Synthesized Co-Pyridine-Derived Catalyst Incorporated in a Nafion-Based Membrane Electrode Assembly. *Adv. Energy Mater.* **2020**, *10* (39), 2–7. https://doi.org/10.1002/aenm.202001645.

(69) Genovese, C.; Ampelli, C.; Perathoner, S.; Centi, G. Electrocatalytic Conversion of CO2 to Liquid Fuels Using Nanocarbon-Based Electrodes. *J. Energy Chem.* **2013**, *22* (2), 202–213. https://doi.org/10.1016/S2095-4956(13)60026-1.

(70) Gutiérrez-Guerra, N.; Valverde, J. L.; Romero, A.; Serrano-Ruiz, J. C.; de Lucas-Consuegra, A. Electrocatalytic Conversion of CO2 to Added-Value Chemicals in a High-Temperature Proton-Exchange Membrane Reactor. *Electrochem. commun.* **2017**, *81*, 128–131. https://doi.org/10.1016/j.elecom.2017.06.018.

(71) Xia, C.; Zhu, P.; Jiang, Q.; Pan, Y.; Liang, W.; Stavitsk, E.; Alshareef, H. N.; Wang, H. Continuous Production of Pure Liquid Fuel Solutions via Electrocatalytic CO2 Reduction Using Solid-Electrolyte Devices. *Nat. Energy* **2019**, *4* (9), 776–785. https://doi.org/10.1038/s41560-019-0451-x.

(72) Fan, L.; Xia, C.; Zhu, P.; Lu, Y.; Wang, H. Electrochemical CO2 Reduction to High-Concentration Pure Formic Acid Solutions in an All-Solid-State Reactor. *Nat. Commun.* **2020**, *11* (1), 1–9. https://doi.org/10.1038/s41467-

020-17403-1.

(73) Yin, Z.; Peng, H.; Wei, X.; Zhou, H.; Gong, J.; Huai, M.; Xiao, L.; Wang, G.; Lu, J.; Zhuang, L. An Alkaline Polymer Electrolyte CO2 Electrolyzer Operated with Pure Water. *Energy Environ. Sci.* **2019**, *12* (8), 2455–2462. https://doi.org/10.1039/c9ee01204d.

(74) Thorson, M. R.; Siil, K. I.; Kenis, P. J. A. Effect of Cations on the Electrochemical Conversion of CO 2 to CO . *J. Electrochem. Soc.* **2013**, *160* (1), F69–F74. https://doi.org/10.1149/2.052301jes.

(75) Larrazábal, G. O.; Martín, A. J.; Krumeich, F.; Hauert, R.; Pérez-Ramírez, J. Solvothermally-Prepared Cu2O Electrocatalysts for CO2 Reduction with Tunable Selectivity by the Introduction of p-Block Elements. *ChemSusChem* **2017**, *10* (6), 1255–1265. https://doi.org/10.1002/cssc.201601578.

(76) Monteiro, M. C. O.; Philips, M. F.; Schouten, K. J. P.; Koper, M. T. M. Efficiency and Selectivity of CO2 Reduction to CO on Gold Gas Diffusion Electrodes in Acidic Media. *Nat. Commun.* **2021**, *12* (1), 1–7. https://doi.org/10.1038/s41467-021-24936-6.

(77) Lu, Q.; Rosen, J.; Zhou, Y.; Hutchings, G. S.; Kimmel, Y. C.; Chen, J. G.; Jiao, F. A Selective and Efficient Electrocatalyst for Carbon Dioxide Reduction. *Nat. Commun.* **2014**, *5*, 1–6. https://doi.org/10.1038/ncomms4242.

(78) Qian, C.; Sun, W.; Hung, D. L. H.; Qiu, C.; Makaremi, M.; Hari Kumar, S. G.; Wan, L.; Ghoussoub, M.; Wood, T. E.; Xia, M.; Tountas, A. A.; Li, Y. F.; Wang, L.; Dong, Y.; Gourevich, I.; Singh, C. V.; Ozin, G. A. Catalytic CO2 Reduction by Palladium-Decorated Silicon–Hydride Nanosheets. *Nat. Catal.* **2019**, *2* (1), 46–54. https://doi.org/10.1038/s41929-018-0199-x.

(79) Luo, W.; Zhang, Q.; Zhang, J.; Moioli, E.; Zhao, K.; Züttel, A. Electrochemical Reconstruction of ZnO for Selective Reduction of CO2 to CO. *Appl. Catal. B Environ.* **2020**, *273* (April), 119060. https://doi.org/10.1016/j.apcatb.2020.119060.

(80) Yu, J.; Wang, J.; Ma, Y.; Zhou, J.; Wang, Y.; Lu, P.; Yin, J.; Ye, R.; Zhu, Z.; Fan, Z. Recent Progresses in Electrochemical Carbon Dioxide Reduction on Copper-Based Catalysts toward Multicarbon Products. *Adv. Funct. Mater.* **2021**, 2102151. https://doi.org/10.1002/adfm.202102151.

(81) Esmaeilirad, M.; Baskin, A.; Kondori, A.; Sanz-Matias, A.; Qian, J.; Song, B.; Tamadoni Saray, M.; Kucuk, K.; Belmonte, A. R.; Delgado, P. N. M.;

Park, J.; Azari, R.; Segre, C. U.; Shahbazian-Yassar, R.; Prendergast, D.; Asadi, M. Gold-like Activity Copper-like Selectivity of Heteroatomic Transition Metal Carbides for Electrocatalytic Carbon Dioxide Reduction Reaction. *Nat. Commun.* **2021**, *12* (1), 1–10. https://doi.org/10.1038/s41467-021-25295-y.

(82) Liang, S.; Huang, L.; Gao, Y.; Wang, Q.; Liu, B. Electrochemical Reduction of CO2 to CO over Transition Metal/N-Doped Carbon Catalysts: The Active Sites and Reaction Mechanism. *Adv. Sci.* **2021**, *8* (24), 1–23. https://doi.org/10.1002/advs.202102886.

(83) Lin, S.; Diercks, C. S.; Zhang, Y. B.; Kornienko, N.; Nichols, E. M.; Zhao, Y.; Paris, A. R.; Kim, D.; Yang, P.; Yaghi, O. M.; Chang, C. J. Covalent Organic Frameworks Comprising Cobalt Porphyrins for Catalytic CO2 Reduction in Water. *Science (80-.).* **2015**, *349* (6253), 1208–1213. https://doi.org/10.1126/science.aac8343.

(84) Kornienko, N.; Zhao, Y.; Kley, C. S.; Zhu, C.; Kim, D.; Lin, S.; Chang, C. J.; Yaghi, O. M.; Yang, P. Metal-Organic Frameworks for Electrocatalytic Reduction of Carbon Dioxide. *J. Am. Chem. Soc.* **2015**, *137* (44), 14129–14135. https://doi.org/10.1021/jacs.5b08212.

(85) He, T.; Chen, S.; Ni, B.; Gong, Y.; Wu, Z.; Song, L.; Gu, L.; Hu, W.; Wang, X. Zirconium–Porphyrin-Based Metal–Organic Framework Hollow Nanotubes for Immobilization of Noble-Metal Single Atoms. *Angew. Chemie - Int. Ed.* **2018**, *57* (13), 3493–3498. https://doi.org/10.1002/anie.201800817.

(86) Chen, Z.; Wang, J.; Zhang, S.; Zhang, Y.; Zhang, J.; Li, R.; Peng, T. Porphyrin-Based Conjugated Polymers as Intrinsic Semiconducting Photocatalysts for Robust H 2 Generation under Visible Light . *ACS Appl. Energy Mater.* **2019**, *2* (8), 5665–5676. https://doi.org/10.1021/acsaem.9b00811.

(87) Zhang, Y.; Dong, L.-Z.; Li, S.; Huang, X.; Chang, J.-N.; Wang, J.-H.; Zhou, J.; Li, S.-L.; Lan, Y.-Q. Coordination Environment Dependent Selectivity of Single-Site-Cu Enriched Crystalline Porous Catalysts in CO2 Reduction to CH4. *Nat. Commun.* **2021**, *12* (1), 1–9. https://doi.org/10.1038/s41467-021-26724-8.

(88) Chase, M. W. NIST-JANAF Thermochemical Tables, 4th Ed. J. Phys. Chem. Ref. Data. 1998, Monograph 9(Part I and Part II). *Journal of Physical and Chemical Reference Data*. 1998, p Part I&II.

(89) Risplendi, F.; Re Fiorentin, M.; Cicero, G. Unravelling Electrocatalytic

Properties of Metal Porphyrin-like Complexes Hosted in Graphene Matrices. *2D Mater.* **2020**, *7* (2). https://doi.org/10.1088/2053-1583/ab6a5f.

(90) Nørskov, J. K.; Rossmeisl, J.; Logadottir, A.; Lindqvist, L.; Kitchin, J. R.; Bligaard, T.; Jónsson, H. Origin of the Overpotential for Oxygen Reduction at a Fuel-Cell Cathode. *J. Phys. Chem. B* **2004**, *108* (46), 17886–17892. https://doi.org/10.1021/jp047349j.

(91) Rossmeisl, J.; Qu, Z. W.; Zhu, H.; Kroes, G. J.; Nørskov, J. K. Electrolysis of Water on Oxide Surfaces. *J. Electroanal. Chem.* **2007**, *607* (1–2), 83–89. https://doi.org/10.1016/j.jelechem.2006.11.008.

(92) Rossmeisl, J.; Logadottir, A.; Nørskov, J. K. Electrolysis of Water on (Oxidized) Metal Surfaces. *Chem. Phys.* **2005**, *319* (1–3), 178–184. https://doi.org/10.1016/j.chemphys.2005.05.038.

(93) Chiolerio, A.; Bocchini, S.; Porro, S. Inkjet Printed Negative Supercapacitors: Synthesis of Polyaniline-Based Inks, Doping Agent Effect, and Advanced Electronic Devices Applications. *Adv. Funct. Mater.* **2014**, *24* (22), 3375–3383. https://doi.org/10.1002/adfm.201303371.

(94) Xu, H.; Zhang, J.; Chen, Y.; Lu, H.; Zhuang, J. Electrochemical Polymerization of Polyaniline Doped with Zn2+ as the Electrode Material for Electrochemical Supercapacitors. *J. Solid State Electrochem.* **2014**, *18* (3), 813–819. https://doi.org/10.1007/s10008-013-2327-5.

(95) Xu, H.; Zhang, J.; Chen, Y.; Zhuang, J.; Lu, H. Electrochemical Polymerization of Polyaniline Doped with Mn2+ as Electrode Material for Electrochemical Supercapacitors. *Gaofenzi Cailiao Kexue Yu Gongcheng/Polymeric Mater. Sci. Eng.* **2014**, *30* (10), 23–27. https://doi.org/10.1039/c3ra45794j.

(96) Chiolerio, A.; Bocchini, S.; Scaravaggi, F.; Porro, S.; Perrone, D.; Beretta, D.; Caironi, M.; Fabrizio Pirri, C. Synthesis of Polyaniline-Based Inks for Inkjet Printed Devices: Electrical Characterization Highlighting the Effect of Primary and Secondary Doping. *Semicond. Sci. Technol.* **2015**, *30* (10). https://doi.org/10.1088/0268-1242/30/10/104001.

(97) Izumi, C. M. S.; Rodrigues, D. C.; Pelaes, L. A. G.; Da Costa Ferreira, A. M.; Temperini, M. L. A. Influence of Different Copper(II) Salts on the Oxidation and Doping Reactions of Emeraldine Base Polyaniline. *Vib. Spectrosc.* **2016**, *87*, 129–136. https://doi.org/10.1016/j.vibspec.2016.09.019.

(98) Bocchini, S.; Chiolerio, A.; Porro, S.; Accardo, D.; Garino, N.; Bejtka, K.; Perrone, D.; Pirri, C. F. Synthesis of Polyaniline-Based Inks, Doping Thereof and Test Device Printing towards Electronic Applications. *J. Mater. Chem. C* **2013**, *1* (33), 5101–5109. https://doi.org/10.1039/c3tc30764f.

(99) Gul, S.; Shah, A. U. H. A.; Bilal, S. Synthesis and Characterization of Processable Polyaniline Salts. *J. Phys. Conf. Ser.* **2013**, *439* (1). https://doi.org/10.1088/1742-6596/439/1/012002.

(100) Vasquez, R. P. CuCl by XPS. *Surf. Sci. Spectra* **1993**, *2* (2), 138–143. https://doi.org/10.1116/1.1247732.

(101) Biesinger, M. C. Advanced Analysis of Copper X-Ray Photoelectron Spectra. *Surf. Interface Anal.* **2017**, *49* (13), 1325–1334. https://doi.org/10.1002/sia.6239.

(102) Xu, H.; Zhang, J.; Chen, Y.; Lu, H.; Zhuang, J. Electrochemical Polymerization of Polyaniline Doped with Cu2+ as the Electrode Material for Electrochemical Supercapacitors. *RSC Adv.* **2014**, *4* (11), 5547–5552. https://doi.org/10.1039/c3ra45794j.

(103) Bejtka, K.; Zeng, J.; Sacco, A.; Castellino, M.; Hernández, S.; Farkhondehfal, M. A.; Savino, U.; Ansaloni, S.; Pirri, C. F.; Chiodoni, A. Chainlike Mesoporous SnO2 as a Well-Performing Catalyst for Electrochemical CO2 Reduction. *ACS Appl. Energy Mater.* **2019**, *2* (5), 3081–3091. https://doi.org/10.1021/acsaem.8b02048.

(104) Kwoka, M.; Ottaviano, L.; Passacantando, M.; Santucci, S.; Czempik, G.; Szuber, J. XPS Study of the Surface Chemistry of L-CVD SnO2 Thin Films after Oxidation. *Thin Solid Films* **2005**, *490* (1), 36–42. https://doi.org/10.1016/j.tsf.2005.04.014.

(105) Stranick, M. A.; Moskwa, A. SnO2 by XPS. *Surf. Sci. Spectra* **1993**, *2* (1), 50–54. https://doi.org/10.1116/1.1247724.

(106) Nesbitt, H. W.; Banerjee, D. Interpretation of XPS Mn(2p) Spectra of Mn Oxyhydroxides and Constraints on the Mechanism of MnO2 Precipitation. *Am. Mineral.* **1998**, *83* (3–4), 305–315. https://doi.org/10.2138/am-1998-3-414.

(107) Biesinger, M. C.; Payne, B. P.; Grosvenor, A. P.; Lau, L. W. M.; Gerson, A. R.; Smart, R. S. C. Resolving Surface Chemical States in XPS Analysis of First Row Transition Metals, Oxides and Hydroxides: Cr, Mn, Fe, Co and Ni. *Appl. Surf. Sci.* **2011**, *257* (7), 2717–2730. https://doi.org/10.1016/j.apsusc.2010.10.051.

(108) Grosvenor, A. P.; Kobe, B. A.; Biesinger, M. C.; McIntyre, N. S. Investigation of Multiplet Splitting of Fe 2p XPS Spectra and Bonding in Iron Compounds. *Surf. Interface Anal.* **2004**, *36* (12), 1564–1574. https://doi.org/10.1002/sia.1984.

(109) Xu, H.; Wu, J.; Li, C.; Zhang, J.; Liu, J. Investigation of Polyaniline Films Doped with Fe3+ as the Electrode Material for Electrochemical Supercapacitors. *Electrochim. Acta* **2015**, *165*, 14–21. https://doi.org/10.1016/j.electacta.2015.01.224.

(110) Kumar, S. N.; Gaillard, F.; Bouyssoux, G.; Sartre, A. High-Resolution XPS Studies of Electrochemically Synthesized Conducting Polyaniline Films. *Synth. Met.* **1990**, *36* (1), 111–127. https://doi.org/10.1016/0379-6779(90)90240-L.

(111) Bocchini, S.; Castellino, M.; Della Pina, C.; Rajan, K.; Falletta, E.; Chiolerio, A. Inkjet Printed Doped Polyaniline: Navigating through Physics and Chemistry for the next Generation Devices. *Appl. Surf. Sci.* **2018**, *456*, 246–258. https://doi.org/10.1016/j.apsusc.2018.06.003.

(112) Sacco, A. Electrochemical Impedance Spectroscopy as a Tool to Investigate the Electroreduction of Carbon Dioxide: A Short Review. *J. CO2 Util.* **2018**, *27* (January), 22–31. https://doi.org/10.1016/j.jcou.2018.06.020.

(113) Jhong, H. R. Q.; Brushett, F. R.; Kenis, P. J. A. The Effects of Catalyst Layer Deposition Methodology on Electrode Performance. *Adv. Energy Mater.* **2013**, *3* (5), 589–599. https://doi.org/10.1002/aenm.201200759.

(114) Ott, S.; Orfanidi, A.; Schmies, H.; Anke, B.; Nong, H. N.; Hübner, J.; Gernert, U.; Gliech, M.; Lerch, M.; Strasser, P. Ionomer Distribution Control in Porous Carbon-Supported Catalyst Layers for High-Power and Low Pt-Loaded Proton Exchange Membrane Fuel Cells. *Nat. Mater.* **2020**, *19* (1), 77–85. https://doi.org/10.1038/s41563-019-0487-0.

(115) Ju, W.; Bagger, A.; Hao, G. P.; Varela, A. S.; Sinev, I.; Bon, V.; Roldan Cuenya, B.; Kaskel, S.; Rossmeisl, J.; Strasser, P. Understanding Activity and Selectivity of Metal-Nitrogen-Doped Carbon Catalysts for Electrochemical Reduction of CO2. *Nat. Commun.* **2017**, *8* (1), 1–9. https://doi.org/10.1038/s41467-017-01035-z.

(116) Zhao, S.; Li, S.; Guo, T.; Zhang, S.; Wang, J.; Wu, Y.; Chen, Y. Advances in Sn-Based Catalysts for Electrochemical CO2 Reduction. *Nano-Micro Lett.* **2019**, *11* (1). https://doi.org/10.1007/s40820-019-0293-x.

(117) Golczak, S.; Kanciurzewska, A.; Fahlman, M.; Langer, K.; Langer, J. J. Comparative XPS Surface Study of Polyaniline Thin Films. *Solid State Ionics* **2008**, *179* (39), 2234–2239. https://doi.org/10.1016/j.ssi.2008.08.004.

(118) Chiolerio, A.; Bocchini, S.; Crepaldi, M.; Bejtka, K.; Pirri, C. F. Bridging Electrochemical and Electron Devices: Fast Resistive Switching Based on Polyaniline from One Pot Synthesis Using FeCl3 as Oxidant and Co-Doping Agent. *Synth. Met.* **2017**, *229* (April), 72–81. https://doi.org/10.1016/j.synthmet.2017.05.001.

(119) Yoon, S. B.; Yoon, E. H.; Kim, K. B. Electrochemical Properties of Leucoemeraldine, Emeraldine, and Pernigraniline Forms of Polyaniline/Multi-Wall Carbon Nanotube Nanocomposites for Supercapacitor Applications. *J. Power Sources* **2011**, *196* (24), 10791–10797. https://doi.org/10.1016/j.jpowsour.2011.08.107.

(120) Tantawy, H. R.; Kengne, B. A. F.; McIlroy, D. N.; Nguyen, T.; Heo, D.; Qiang, Y.; Aston, D. E. X-Ray Photoelectron Spectroscopy Analysis for the Chemical Impact of Solvent Addition Rate on Electromagnetic Shielding Effectiveness of HCl-Doped Polyaniline Nanopowders. *J. Appl. Phys.* **2015**, *118* (17). https://doi.org/10.1063/1.4934851.

(121) Mohtasebi, A.; Chowdhury, T.; Hsu, L. H. H.; Biesinger, M. C.; Kruse, P. Interfacial Charge Transfer between Phenyl-Capped Aniline Tetramer Films and Iron Oxide Surfaces. *J. Phys. Chem. C* **2016**, *120* (51), 29248–29263. https://doi.org/10.1021/acs.jpcc.6b09950.

(122) Ren, X.; Liu, Y.; Lee, D. G.; Kim, W. Bin; Han, G. S.; Jung, H. S.; Liu, S. (Frank). Chlorine-modified SnO 2 Electron Transport Layer for High-efficiency Perovskite Solar Cells . *InfoMat* **2020**, *2* (2), 401–408. https://doi.org/10.1002/inf2.12059.

(123) Gong, W.; Guo, H.; Zhang, H.; Yang, J.; Chen, H.; Wang, L.; Hao, F.; Niu, X. Chlorine-Doped SnO2hydrophobic Surfaces for Large Grain Perovskite Solar Cells. *J. Mater. Chem. C* **2020**, *8* (33), 11638–11646. https://doi.org/10.1039/d0tc00515k.

(124) Sun, D.; Chen, Y. *Electrode Kinetics of CO2 Electroreduction*; 2016. https://doi.org/10.1201/b20177-4.

(125) Sassone, D.; Bocchini, S.; Fontana, M.; Salvini, C.; Cicero, G.; Re, M.; Risplendi, F.; Latini, G.; Farkhondehfal, M. A.; Pirri, F.; Zeng, J. Imidazole-Imidazolate Pair as Organo-Electrocatalyst for CO 2 Reduction on ZIF-8 Material. *Appl. Energy* **2022**, *324* (June), 119743. https://doi.org/10.1016/j.apenergy.2022.119743.

(126) Winiarski, J.; Tylus, W.; Winiarska, K.; Szczygieł, I.; Szczygieł, B. XPS and FT-IR Characterization of Selected Synthetic Corrosion Products of Zinc Expected in Neutral Environment Containing Chloride Ions. *J. Spectrosc.* **2018**, *2018*. https://doi.org/10.1155/2018/2079278.

(127) Momma, K.; Izumi, F. VESTA 3 for Three-Dimensional Visualization of Crystal, Volumetric and Morphology Data. *J. Appl. Crystallogr.* **2011**, *44* (6), 1272–1276. https://doi.org/10.1107/S0021889811038970.

(128) Geng, W.; Chen, W.; Li, G.; Dong, X.; Song, Y.; Wei, W.; Sun, Y. Induced CO2 Electroreduction to Formic Acid on Metal−Organic Frameworks via Node Doping. *ChemSusChem* **2020**, *201620*, 4035–4040. https://doi.org/10.1002/cssc.202001310.

(129) Liédana, N.; Galve, A.; Rubio, C.; Téllez, C.; Coronas, J. CAF@ZIF-8: One-Step Encapsulation of Caffeine in MOF. *ACS Appl. Mater. Interfaces* **2012**, *4* (9), 5016–5021. https://doi.org/10.1021/am301365h.

(130) Nordin, N. A. H. M.; Ismail, A. F.; Misdan, N.; Nazri, N. A. M. Modified ZIF-8 Mixed Matrix Membrane for CO2/CH4 Separation. *AIP Conf. Proc.* **2017**, *1891* (November). https://doi.org/10.1063/1.5005424.

(131) Cao, S.; Bennett, T. D.; Keen, D. A.; Goodwin, A. L.; Cheetham, A. K. Amorphization of the Prototypical Zeolitic Imidazolate Framework ZIF-8 by Ball-Milling. *Chem. Commun.* **2012**, *48* (63), 7805–7807. https://doi.org/10.1039/c2cc33773h.

(132) Wu, X.; Yue, H.; Zhang, Y.; Gao, X.; Li, X.; Wang, L.; Cao, Y.; Hou, M.; An, H.; Zhang, L.; Li, S.; Ma, J.; Lin, H.; Fu, Y.; Gu, H.; Lou, W.; Wei, W.; Zare, R. N.; Ge, J. Packaging and Delivering Enzymes by Amorphous Metal-Organic Frameworks. *Nat. Commun.* **2019**, *10* (1), 1–8. https://doi.org/10.1038/s41467-019-13153-x.

(133) Bennett, T. D.; Cao, S.; Tan, J. C.; Keen, D. A.; Bithell, E. G.; Beldon, P. J.; Friscic, T.; Cheetham, A. K. Facile Mechanosynthesis of Amorphous Zeolitic Imidazolate Frameworks. *J. Am. Chem. Soc.* **2011**, *133* (37), 14546–14549. https://doi.org/10.1021/ja206082s.

(134) Hameed, N.; Church, J. S.; Salim, N. V.; Hanley, T. L.; Amini, A.; Fox, B. L. Dispersing Single-Walled Carbon Nanotubes in Ionic Liquids: A Quantitative Analysis. *RSC Adv.* **2013**, *3* (43), 20034–20039. https://doi.org/10.1039/c3ra42488j.

(135) Goyal, S.; Shaharun, M. S.; Kait, C. F.; Abdullah, B.; Ameen, M.

Photoreduction of Carbon Dioxide to Methanol over Copper Based Zeolitic Imidazolate Framework-8: A New Generation Photocatalyst. *Catalysts* **2018**, *8* (12). https://doi.org/10.3390/catal8120581.

(136) Schejn, A.; Aboulaich, A.; Balan, L.; Falk, V.; Lalevée, J.; Medjahdi, G.; Aranda, L.; Mozet, K.; Schneider, R. Cu2+-Doped Zeolitic Imidazolate Frameworks (ZIF-8): Efficient and Stable Catalysts for Cycloadditions and Condensation Reactions. *Catal. Sci. Technol.* **2015**, *5* (3), 1829–1839. https://doi.org/10.1039/c4cy01505c.

(137) Pan, Y.; Liu, Y.; Zeng, G.; Zhao, L.; Lai, Z. Rapid Synthesis of Zeolitic Imidazolate Framework-8 (ZIF-8) Nanocrystals in an Aqueous System. *Chem. Commun.* **2011**, *47* (7), 2071–2073. https://doi.org/10.1039/c0cc05002d.

(138) Cravillon, J.; Münzer, S.; Lohmeier, S. J.; Feldhoff, A.; Huber, K.; Wiebcke, M. Rapid Room-Temperature Synthesis and Characterization of Nanocrystals of a Prototypical Zeolitic Imidazolate Framework. *Chem. Mater.* **2009**, *21* (8), 1410–1412. https://doi.org/10.1021/cm900166h.

(139) Mu, L.; Liu, B.; Liu, H.; Yang, Y.; Sun, C.; Chen, G. A Novel Method to Improve the Gas Storage Capacity of ZIF-8. *J. Mater. Chem.* **2012**, *22* (24), 12246–12252. https://doi.org/10.1039/c2jm31541f.

(140) Weng, T.; Schmidt, J. R. Structure and Thermodynamic Stability of Zeolitic Imidazolate Framework Surfaces. *J. Phys. Chem. C* **2020**, *124* (2), 1458–1468. https://doi.org/10.1021/acs.jpcc.9b10124.

(141) Tuncel, D.; Ökte, A. N. Improved Adsorption Capacity and Photoactivity of ZnO-ZIF-8 Nanocomposites. *Catal. Today* **2021**, *361* (April 2020), 191–197. https://doi.org/10.1016/j.cattod.2020.04.014.

(142) Tian, F.; Cerro, A. M.; Mosier, A. M.; Wayment-Steele, H. K.; Shine, R. S.; Park, A.; Webster, E. R.; Johnson, L. E.; Johal, M. S.; Benz, L. Surface and Stability Characterization of a Nanoporous ZIF-8 Thin Film. *J. Phys. Chem. C* **2014**, *118* (26), 14449–14456. https://doi.org/10.1021/jp5041053.

(143) Duchoslav, J.; Steinberger, R.; Arndt, M.; Stifter, D. XPS Study of Zinc Hydroxide as a Potential Corrosion Product of Zinc: Rapid X-Ray Induced Conversion into Zinc Oxide. *Corros. Sci.* **2014**, *82*, 356–361. https://doi.org/10.1016/j.corsci.2014.01.037.

(144) Izadyar, M.; Rezaeian, M.; Victorov, A. Theoretical Study on the Absorption of Carbon Dioxide by DBU-Based Ionic Liquids. *Phys. Chem. Chem. Phys.* **2020**, *22* (35), 20050–20060. https://doi.org/10.1039/d0cp03612a.

(145) Zhu, X.; Song, M.; Xu, Y. DBU-Based Protic Ionic Liquids for CO2 Capture. *ACS Sustain. Chem. Eng.* **2017**, *5* (9), 8192–8198. https://doi.org/10.1021/acssuschemeng.7b01839.

(146) Kaneti, Y. V.; Dutta, S.; Hossain, M. S. A.; Shiddiky, M. J. A.; Tung, K. L.; Shieh, F. K.; Tsung, C. K.; Wu, K. C. W.; Yamauchi, Y. Strategies for Improving the Functionality of Zeolitic Imidazolate Frameworks: Tailoring Nanoarchitectures for Functional Applications. *Adv. Mater.* **2017**, *29* (38), 1–31. https://doi.org/10.1002/adma.201700213.

(147) Pang, S. H.; Han, C.; Sholl, D. S.; Jones, C. W.; Lively, R. P. Facet-Specific Stability of ZIF-8 in the Presence of Acid Gases Dissolved in Aqueous Solutions. *Chem. Mater.* **2016**, *28* (19), 6960–6967. https://doi.org/10.1021/acs.chemmater.6b02643.

(148) Chizallet, C.; Bats, N. External Surface of Zeolite Imidazolate Frameworks Viewed Ab Initio: Multifunctionality at the Organic-Inorganic Interface. *J. Phys. Chem. Lett.* **2010**, *1* (1), 349–353. https://doi.org/10.1021/jz900192x.

(149) Lee, G.; Li, Y. C.; Kim, J. Y.; Peng, T.; Nam, D. H.; Sedighian Rasouli, A.; Li, F.; Luo, M.; Ip, A. H.; Joo, Y. C.; Sargent, E. H. Electrochemical Upgrade of CO2 from Amine Capture Solution. *Nat. Energy* **2021**, *6* (1), 46–53. https://doi.org/10.1038/s41560-020-00735-z.

(150) Rendón-Calle, A.; Builes, S.; Calle-Vallejo, F. Substantial Improvement of Electrocatalytic Predictions by Systematic Assessment of Solvent Effects on Adsorption Energies. *Appl. Catal. B Environ.* **2020**, *276* (February), 119147. https://doi.org/10.1016/j.apcatb.2020.119147.

(151) Kim, D.; Kim, D. W.; Hong, W. G.; Coskun, A. Graphene/ZIF-8 Composites with Tunable Hierarchical Porosity and Electrical Conductivity. *J. Mater. Chem. A* **2016**, *4* (20), 7710–7717. https://doi.org/10.1039/c6ta01899h.

(152) Zeng, J.; Fontana, M.; Sacco, A.; Sassone, D.; Pirri, C. F. A Study of the Effect of Electrode Composition on the Electrochemical Reduction of CO2. *Catal. Today* **2021**, No. July. https://doi.org/10.1016/j.cattod.2021.07.014.

(153) Buriez, O.; Labbé, E.; Pigeon, P.; Jaouen, G.; Amatore, C. Electrochemical Attachment of a Conjugated Amino-Ferrocifen Complex onto Carbon and Metal Surfaces. *J. Electroanal. Chem.* **2008**, *619–620* (1–2), 169–175. https://doi.org/10.1016/j.jelechem.2008.04.012.

(154) Giovanelli, L.; Lee, H. L.; Lacaze-Dufaure, C.; Koudia, M.; Clair, S.; Lin, Y. P.; Ksari, Y.; Themlin, J. M.; Abel, M.; Cafolla, A. A. Electronic Structure

of Tetra(4-Aminophenyl)Porphyrin Studied by Photoemission, UV–Vis Spectroscopy and Density Functional Theory. *J. Electron Spectros. Relat. Phenomena* **2017**, *218*, 40–45. https://doi.org/10.1016/j.elspec.2017.05.005.

(155) Mangione, G.; Carlotto, S.; Sambi, M.; Ligorio, G.; Timpel, M.; Vittadini, A.; Nardi, M. V.; Casarin, M. Electronic Structures of CuTPP and CuTPP(F) Complexes. A Combined Experimental and Theoretical Study I. *Phys. Chem. Chem. Phys.* **2016**, *18* (28), 18727–18738. https://doi.org/10.1039/c6cp01423b.

(156) Xiao, J.; Ditze, S.; Chen, M.; Buchner, F.; Stark, M.; Drost, M.; Steinrück, H. P.; Gottfried, J. M.; Marbach, H. Temperature-Dependent Chemical and Structural Transformations from 2H-Tetraphenylporphyrin to Copper(II)-Tetraphenylporphyrin on Cu(111). *J. Phys. Chem. C* **2012**, *116* (22), 12275–12282. https://doi.org/10.1021/jp301757h.

(157) Hu, Y.; Goodeal, N.; Chen, Y.; Ganose, A. M.; Palgrave, R. G.; Bronstein, H.; Blunt, M. O. Probing the Chemical Structure of Monolayer Covalent-Organic Frameworks Grown: Via Schiff-Base Condensation Reactions. *Chem. Commun.* **2016**, *52* (64), 9941–9944. https://doi.org/10.1039/c6cc03895f.

(158) Robert, M. Confined Molecular Catalysts Provide an Alternative Interpretation to the Electrochemically Reversible Demetallation of Copper Complexes. **2022**, 11–13. https://doi.org/10.1038/s41467-022-31661-1.

(159) Creissen, C. E.; Fontecave, M. Keeping Sight of Copper in Single-Atom Catalysts for Electrochemical Carbon Dioxide Reduction. *Nat. Commun.* **2022**, *13* (1), 1–4. https://doi.org/10.1038/s41467-022-30027-x.

(160) Eilert, A.; Roberts, F. S.; Friebel, D.; Nilsson, A. Formation of Copper Catalysts for CO $_2$ Reduction with High Ethylene/Methane Product Ratio Investigated with In Situ X-Ray Absorption Spectroscopy. *J. Phys. Chem. Lett.* **2016**, *7* (8), 1466–1470. https://doi.org/10.1021/acs.jpclett.6b00367.

(161) Weng, Z.; Jiang, J.; Wu, Y.; Wu, Z.; Guo, X.; Materna, K. L.; Liu, W.; Batista, V. S.; Brudvig, G. W.; Wang, H. Electrochemical CO2Reduction to Hydrocarbons on a Heterogeneous Molecular Cu Catalyst in Aqueous Solution. *J. Am. Chem. Soc.* **2016**, *138* (26), 8076–8079. https://doi.org/10.1021/jacs.6b04746.